On a Cartesian cut-cell methodology for simulating atmospheric ice accretion on aircraft

Lukas Wutschitz
Department of Physics
University of Cambridge

This dissertation is submitted for the degree of:
Doctor of Philosophy

Selwyn College
September 2018

Abstract

Atmospheric in-flight ice accretion has been a significant operational hazard in aviation for decades. Super-cooled water droplets impinge on exposed surfaces such as wings and rotor blades. These droplets may freeze on the surface thereby changing lift characteristics and disturb weight and aerodynamic balances.

The multiple length scales involved prevent designing dynamically similar flows making traditional aeronautical engineering tools such as wind tunnel experiments not suitable. Therefore, computational fluid dynamics (CFD) methods have proved an attractive alternative to study atmospheric icing effects. However, most approaches are based on simple incompressible models and are only suited for small ice heights due to the difficulty of dynamically tracking the ice accretion. This thesis aims to develop novel mathematical models to capture more relevant phenomena and to improve the numerical methods to allow dynamic tracking of the air-ice interface.

The initial chapter presents an augmented air and droplet model which tracks droplet temperatures thereby producing more accurate heat fluxes for the phase transition calculation. Firstly, we validate our novel model for common ice accretion test cases and find excellent agreement with literature. The advantage of the augmented system is demonstrated by applying it to an experimental setup that studies the heat exchange between water droplets and air for various flow conditions. We find excellent agreement between our model and the experiment for all presented cases whereas constant-temperature approaches match only for short interaction times. Finally, we apply the new system to study the droplet temperatures around various aerofoil and find significant temperature differences compared with conventional models.

The following chapter studies the freezing process on the wing geometry. Presently, the most advanced model is based on lubrication theory, however, linear terms are truncated. We extend the series expansion to include first order terms and demonstrate that the additional order is necessary to accurately capture the thin film flow on a cylinder. Furthermore, we extend the lubrication-theory-based approach which was limited to simple geometries. The extended model is valid on arbitrary wing shapes making it more relevant for engineers studying real-world problems.

The penultimate chapter combines the previous two to give a simulation of the full icing process. We integrate it with a Cartesian cut-cell method which can cope dynamically with moving interfaces. The robustness and performance of the cut-cell techniques allow us to simulate ice growth on real-world geometries. We demonstrate this capability by presenting results of the dynamic ice growth on a NACA 0012 aerofoil - making this the first such numerical experiment.

Declaration

This dissertation is the result of my own work and includes nothing which is the outcome of work done in collaboration except as declared in the Preface and specified in the text. It is not substantially the same as any that I have submitted, or, is being concurrently submitted for a degree or diploma or other qualification at the University of Cambridge or any other University or similar institution except as declared in the Preface and specified in the text. I further state that no substantial part of my dissertation has already been submitted, or, is being concurrently submitted for any such degree, diploma or other qualification at the University of Cambridge or any other University or similar institution except as declared in the Preface and specified in the text. It does not exceed the limit of sixty thousand words prescribed by the Degree Committee for Physics and Chemistry.

Lukas Wutschitz,
September 2018

Acknowledgements

This thesis would not have been possible without the support and guidance of my supervisor Dr Nikos Nikiforakis.

I would like to also thank my fellow members of the Laboratory for Scientific Computing who have made the past five years such a great experience. In particular, thanks are due to Nandan Gokhale, Murray Cutforth and Lefteris Ioannou for countless interesting discussions in our office. I would also like to express my gratitude to Dr Philip Blakely as a never ending source of C++ wisdom and Dr Oliver Strickson for many fruitful discussions and invaluable advice. This thesis has benefited greatly from the input of my diligent proofreaders Alo Roosing and William Drazin. Thanks are also due to my fiends Hiroe Yamazaki, Peter Wirnsberger, Raman Ganti and Chongli Qin who made Cambridge feel like home over the past years.

Thanks also go to my family, Birgit, Lukas, and Lorenz, for their unwavering support over the past five years. I would also like to thank my uncle, Pius, who has sparked my interest in physics, maths and programming many years ago.

Finally, I would like to acknowledge the sponsorship by the Engineering and Physical Sciences Research Council for this PhD project.

Contents

1 Introduction 1
   1.1 Terminology and contributing physical phenomena 2
      1.1.1 Ice producing precipitation 2
      1.1.2 Liquid water content (LWC) 3
      1.1.3 Types of ice shape 4
      1.1.4 Outside air temperature 4
      1.1.5 Airspeed 5
      1.1.6 Median volumetric diameter (MVD) 5
      1.1.7 Gravity 6
   1.2 Modules of icing simulations 6
      1.2.1 Air flow 6
      1.2.2 Droplet flow 8
      1.2.3 Ice growth 10
      1.2.4 Time stepping 12
   1.3 Previous work 13
   1.4 Conclusions of literature review 14
   1.5 Thesis outline 14
   1.6 Conventions and notation 16

2 Modelling of water droplet and air flow 17
   2.1 Introduction 17
      2.1.1 Outline of this chapter 18
   2.2 Mathematical models 19
      2.2.1 Governing equations 20
      2.2.2 Coupling terms 21

2.2.3 Homogeneous equations 23
2.3 Numerical methods 24
2.3.1 Non-negativity preservation 24
2.3.2 Boundary conditions 25
2.3.3 Cut-cell method 26
2.3.4 Source terms 30
2.3.5 Adaptive mesh refinement 32
2.4 Validation 32
2.4.1 Validation of air and droplet coupling 32
2.4.2 Validation of collection efficiency boundary condition 35
2.4.3 Validation of heat exchange modelling 39
2.5 Case studies 40
2.5.1 Droplet temperature dependence on free-stream Mach number and angle of attack 40
2.5.2 GA-W-1 aerofoil with Fowler flap system 42
2.5.3 DrivAer model 43
2.6 Conclusion 45

3 Surface models 47
3.1 Extraction of external flow states 47
3.2 Boundary layer model 51
3.2.1 Pohlhausen method 51
3.2.2 Transition to turbulence 52
3.3 Surface roughness 54
3.4 Implementation 57
3.5 Validation 57

4 Modelling thin water film freezing 59
4.1 Introduction 59
4.1.1 Previous approaches 59
4.1.2 Conclusions of literature review 62
4.1.3 Outline of this chapter 62
4.2 The generalisation for arbitrarily parameterised surfaces 63
4.2.1 Surfaces, manifolds and notation 63

4.2.2 Dimensional analysis of the Navier Stokes equations 69
4.2.3 Continuity equation 73
4.2.4 Boundary conditions 74
4.2.5 Integration of the governing equations 78
4.2.6 Summary of the physical processes in the water film 81
4.3 Numerical methods for the water film 81
4.3.1 Explicit portion 82
4.3.2 Implicit portion 83
4.4 Validation tests for the water film 84
4.5 Importance of $\mathcal{O}(\varepsilon)$ terms 87
4.6 Flow on a two-dimensional plate 88
4.7 Generalisation for independent droplet temperatures 91
4.7.1 Heat exchange at the free surface 92
4.7.2 Numerical methods for the ice layer 95
4.7.3 Summary of the physical processes in the ice layer 95
4.8 Icing of a flat plate 96
4.9 Conclusions 97

5 The full in-flight ice accretion simulation with a continuously deforming interface 99
5.1 Introduction 99
5.2 RTO/NATO validation test cases for static meshes 100
5.2.1 Core data case 4 101
5.2.2 Optional data case 5 102
5.3 Extension for continuously deforming bodies 103
5.3.1 Boundary treatment for deforming bodies 104
5.3.2 Summary of modules and algorithms of the full continuous ice accretion software 105
5.3.3 Optimisations 108
5.3.4 Validation of the implementation of the geometry update 108
5.4 Showcase: NACA 0012 111
5.5 Conclusions 117

6 Conclusions 119
6.1 Summary 119

6.2 Further Work 120

A Representation of icing geometries 123
A.1 Extraction of cut-cell parameters 123
A.1.1 Signed distance function 124
A.1.2 The Characteristic Scan Conversion (CSC) algorithm 124
A.2 Example: NACA 0012 125

List of Figures

1.1 Illustration of the different types of accreting ice shape. 4
1.2 Illustration of the modular structure of ice accretion simulations. 7

2.1 Cut-cell geometry 28
2.2 A wave solution for the Riemann problem of the pressureless Euler equations. . . 29
2.3 Saito's test for the full particle and gas model at $t = 30\tau$ 34
2.4 Collection efficiencies for a NACA 0012 aerofoil 36
2.5 Flow of air and droplets around a sphere. 37
2.6 Results of the validation test of the heat exchange terms. 38
2.7 Surface temperatures of air and impinging water droplets at the stagnation point. 41
2.8 Illustration of temperature coupling effects of water droplet flow around a GA-W-1 aerofoil with extended Fowler flap system. 42
2.9 Illustration of streamlines of air and droplet phases around a GA-W-1 aerofoil with extended Fowler flap system. 43
2.10 DrivAer model 44

3.1 Illustration of surface data extraction for boundary following computational meshes 48
3.2 Illustration of a naïve surface data extraction for cut-cell meshes 48
3.3 Illustration of surface data extraction for a Cartesian cut-cell mesh using a constant distance between extraction position and rigid body surface. 49
3.4 Flowchart of boundary layer computation 56
3.5 Validation test for surface extraction routine and boundary layer model 58

4.1 Illustration of the ice and water layer 64
4.2 Illustration of the ice and water layer heights 67
4.3 Illustration of the setup of the flat plate validation case 84

4.4 Water height of a shear stress driven thin film 85
4.5 Film on flat plate under shear stress and gravity 86
4.6 Illustration of the test case for assessing importance of $\mathcal{O}(\varepsilon)$ terms 87
4.7 Results for the test case for assessing the importance of $\mathcal{O}(\varepsilon)$ terms 89
4.8 Two-dimensional thin water film on a flat plate 90
4.9 Results for icing of a flat inclined plate after 60s 96
4.10 Results for icing of a flat inclined plate after 60s for different droplet temperatures 97

5.1 Results for the static interface simulation of the NATO C4 test 102
5.2 Results for the static interface simulation of the NATO C4 test 103
5.3 Flowchart of the full simulation with a continuously deforming interface 106
5.4 (Contd.) Flowchart of the full simulation with a continuously deforming interface 107
5.5 Illustration of the temporal structure of the AMR setup 108
5.6 Illustration of moving film boundary of the icing of a flat inclined plate. 109
5.7 Validation of the interface update for the icing of a flat inclined plate 110
5.8 Ice accretion comparison of moving and static interface simulations of the ice accretion of a NACA 0012 aerofoil 113
5.9 Air streamlines for the ice accretion of a NACA 0012 aerofoil. 114
5.10 Droplet streamlines for the ice accretion of a NACA 0012 aerofoil. 115
5.11 Contours of air temperature for the ice accretion of a NACA 0012 aerofoil. 116

List of Tables

1.1 Overview of the models used by current generation icing codes 14

2.1 Initial conditions for Saito's shock tube experiment for the dusty gas model 33
2.2 Discretisation of droplet diameter distribution 35
2.3 Values for physical constants for the air and water droplet simulations. 39

4.1 Physical constants used for the validation of the thin water film and ice solver. . . . 84

Nomenclature

Acronyms

AMR	Adaptive mesh refinement
CFD	Computational fluid dynamics
CFL	Courant-Friedrichs-Lewy
CPU	Central processing unit
GPGPU	General purpose graphics processing unit
KBN	Klein-Bates-Nikiforakis
LPFS	Localised proportional flux stabilisation
LWC	Liquid water content
MPI	Message passing interface
MUSCL	Monotonic upwind scheme for conservation laws
MVD	Median volumetric diameter
ODE	Ordinary differential equation
PDE	Partial differential equation
RANS	Reynolds-averaged Navier-Stokes
SDF	Signed distance function
SLD	Supercooled large droplet

SLIC	Slope limited centred scheme

Physical constants

χ	Evaporation coefficient
γ	Ratio of specific heats
μ	Dynamic viscosity
ν	Kinematic viscosity
σ	Surface tension
c_p	Specific heat capacity at constant pressure
c_v	Specific heat capacity at constant volume
g	Gravitational acceleration
k	Thermal conductivity
L	Latent heat
r	Local recovery factor

Geometrical quantities

α	Fluid cut-cell volume fraction (Section 2.3)
β	Fluid cut-cell face fraction (Section 2.3)
$\boldsymbol{n}$	Normal vector
$\boldsymbol{x}$	Coordinate map
η	Distance in normal direction to the surface
Γ	Christoffel symbol
$\mathscr{M}$	Manifold
ϕ	Signed distance function (Appendix A)

σ	Surface distance (Chapter 3)
ε	Ratio of the characteristic height over the characteristic extent of the water film
a	First fundamental form (Chapter 4)
b	Second fundamental form (Chapter 4)
c	Aerofoil chord length
c	Third fundamental form (Chapter 4)
g	Metric tensor (Chapter 4)
H	Mean curvature (Chapter 4)
s	Surface coordinate

Labels

$\bar{\cdot}$	Ice-water interface quantity
$\cdot^{\infty}, \cdot_{\infty}$	Free stream quantity
$\cdot_{\mathrm{d}}$	Droplet quantity
$\cdot_{\mathrm{a}}$	Air quantity
$\cdot_{\mathrm{i}}$	Ice quantity
$\cdot_{\mathrm{w}}$	Water quantity
$\cdot_{s}$	Index of droplet phase associated with a fixed droplet diameter
$\hat{\cdot}$	Non-dimensional quantity
$\tilde{\cdot}$	Air-water interface quantity
$\underline{\cdot}$	Substrate quantity

Similarity parameters

Ma	Mach number

Nu	Nusselt number
Pe	Peclet number
Pr	Prandtl number
Re	Reynolds number
Sa	Stanton number
St	Stefan number

Variables

α	Volumetric liquid water content
β	Collection efficiency
Δt	Time-step
Λ	Pohlhausen parameter
λ	Wave speed
$\mathscr{C}$	Computational cell
ϕ	Scalar state
ρ	Density
τ	Stress
θ	Boundary layer thickness
ξ	Water layer thickness
ζ	Ice layer thickness
C_{D}	Drag coefficient
c_{f}	Skin friction coefficient
D	Aerodynamic drag

d_s	Representative diameter of droplet phase s
E	Total energy
e	Specific internal energy
F	Numerical flux approximation
f	Flux function
H	Enthalpy
h_c	Heat transfer coefficient
k	Surface roughness height (Chapter 3)
m	Mass
p	Pressure
Q	Flux function of thin film equation (Section 4.2)
Q, q	Heat flux or heat exchange
S	Source term
T	Temperature
t	Time
u	State
u	Velocity of water film (Section 4.2)
v	Velocity

Chapter 1

Introduction

As clouds of water droplets ascend through the atmosphere, they may be cooled to temperatures significantly lower than freezing (Rees, 1976). Due to the lack of ice nuclei, they remain in their liquid phase despite being at subzero temperatures. Droplets in this supercooled state can freeze almost instantly when coming into contact with a nucleation seed. Exposed surfaces of an aircraft such as pitot tubes or the leading edges of wings may act as nucleation seeds thereby collecting a significant amount of ice. Under certain conditions, these accretions form pointy horn shapes which disrupt the air flow and change lift and drag characteristics of the aircraft dramatically. This process traps very few air bubbles giving the ice a translucent appearance and making it almost impossible to be visually detected by pilots. Undetected ice accretion is a primary environmental hazard in the aviation industry and has been the subject of many numerical studies (Wright, 2008; Verdin, 2007; Leese, 2010; Cao and Huang, 2014; Cao et al., 2015; Peng and Xinxin, 2011).

Anti-icing and de-icing procedures have been developed for ice formation prevention and removal. Anti-icing techniques (i.e. precautionary measures) comprise chemical and thermal procedures. In the case of the former, a chemical solution is applied on exposed surfaces before take off, which lowers the freezing point of water. The latter heats the surface of the wing thereby preventing ice from forming. Energy consumption of heating devices is of the order of $100\,\mathrm{kW}$ (Myers and Hammond, 1999) which affects fuel efficiency. On the other hand, de-icing procedures such as de-icing boots and heating systems remove existing ice growth. De-icing boots consist of an additional rubber skin on the leading edge of the wing. If ice growth is detected, the rubber temporarily expands thereby breaking off the ice. Disadvantages are the additional drag of this system and the difficulty of equipping small wings with de-icing boots.

Even though advanced countermeasures exist, the following examples show that a better understanding of the atmospheric in-flight icing phenomenon would contribute to aircraft operation safety. In 1994 pilots of an ATR 72 aircraft lost control after a ridge of ice accreted beyond the de-icing boots (NTSB (National Transportation Safety Board), 1994). Furthermore, the *Bureau d'Enquêtes et d'Analyses* (BEA) concluded that the obstruction of the pitot probes of an Airbus A330 by ice crystals contributed to the loss of the aircraft on its way from Rio de Janeiro to Paris (BEA, 2012).

Experimental approaches to investigate aerodynamic problems such as wind tunnel studies are expensive but have proofed popular since the cost can be reduced by exploiting the scale invariance of the governing equations. Provided all quantities can be scaled appropriately, an equivalent problem can be designed which features a smaller length scale and consequently is suitable to be studied in a smaller wind tunnel. While this is commonly used for external aerodynamics problems such as studying lift and drag characteristics of aerofoils, such an approach is of limited utility when studying a droplet-laden flow since two independent length scales, the one of the droplets and the aerofoil, are present. They cannot be scaled simultaneously to give dynamic similarity. This makes experimental investigation significantly more expensive and the ability to have a predictive and practical simulation capability for this problem highly desirable.

This PhD project aims to improve simulations of ice accretion to understand in-flight icing better and enhance flight safety. To this end, we review existing software and discuss the mathematical models and the physical assumptions that were made. We find that mesh generation is a bottleneck in current simulations and we will develop an ice accretion simulation based on a Cartesian cut-cell method.

1.1 Terminology and contributing physical phenomena

In this section, we define terminology commonly used in icing literature and give a brief introduction into the physical effects that contribute to the ice accretion problem. A comprehensive overview of the problem and the work carried out before 2000 is given by Gent et al. (2000) and by Lynch and Khodadoust (2001). In this section, we will follow their work and briefly summarise their conclusions.

1.1.1 Ice producing precipitation

In this work, we focus on the classical case of ice accretion by impinging supercooled water droplets. It should be noted that there are various other hazards related to ice accumulation as pointed out by Gent et al. (2000) and Lynch and Khodadoust (2001).

In an everyday life situation, the phenomenon of supercooling is rarely observed. This is due to the presence of impurities or foreign particles in water which are often referred to as nucleation seeds or ice nuclei (Mason, 1971). Nucleation seeds initiate the freezing process and hence water at atmospheric pressure undergoes a phase change to the thermodynamically preferred solid state at roughly 0 °C. In the absence of a nucleation seed, it is possible to cool water to temperatures as low as −40 °C and retain a liquid state. In conditions colder than that, water droplets freeze spontaneously (Mason, 1971). Clouds typically consist of small water droplets with a typical droplet diameter of only a few microns. The probability of encountering a nucleation seed in such small amounts of water is low and droplets in clouds often remain in a liquid phase in temperatures as low as −20 °C. These are the droplet size and temperature ranges typically considered in ice accretion simulations. More recently the physics of supercooled large droplets (SLDs) has been studied by Wright and Potapczuk (2004) and Cober et al. (2001). Two categories further comprise supercooled large droplets.

Freezing drizzle: Freezing drizzle includes the smallest droplets within the SLD domain. Droplet diameters range from 50 µm to 400 µm and the water concentration is in the range $0.3\,\mathrm{g\,m^{-3}}$ to $0.4\,\mathrm{g\,m^{-3}}$. The trajectories of droplets of this category tend to be close to ballistic lines and impinge with hardly any deflection by the air flow. Therefore, the extent of the collection is considerably larger than classical collection efficiencies where only droplets with a diameter of less than 50 µm are considered. Moreover, due to the larger volume, spontaneous freezing is more likely. Hence, freezing drizzle is observed for higher temperatures.

Freezing rain: Clouds of freezing rain consist of considerably larger droplets. Diameters range up to 5 mm (Gent et al., 2000). Freezing rain clouds are only rarely found at low ambient temperatures as the presence of ice nuclei in the clouds becomes more likely. Typical freezing rain clouds are found at temperatures in the range from −15 °C to 5 °C. Due to the relatively big mass of water droplets in these type of cloud, inertial forces dominate over drag forces. Hence, the droplets trajectory is of a ballistic character.

1.1.2 Liquid water content (LWC)

A crucial parameter in the computation of ice accretion is the liquid water content (LWC) of the atmosphere. It is defined as the mass of liquid water in a unit volume. The LWC of a cloud typically ranges from $0.1\,\mathrm{g\,m^{-3}} - 0.5\,\mathrm{g\,m^{-3}}$ according to Gent et al. (2000).

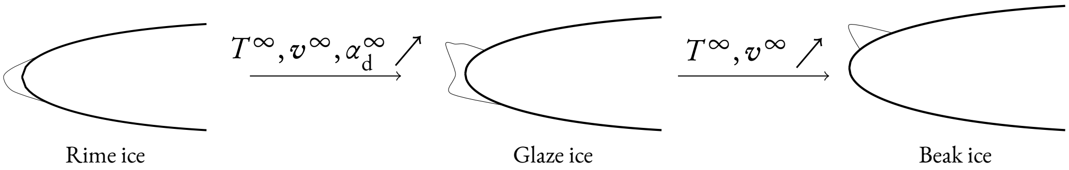

Figure 1.1: Illustration of the different types of accreting ice shape. In cold conditions, slow flight or low water content rime ice forms. This type of ice accretion has a milky opaque appearance. As the ambient temperature T^{∞}, the speed v^{∞} or the ambient water content $\alpha_{\mathrm{d}}^{\infty}$ increases a liquid water film appears which subsequently freezes resulting in glaze ice. In even milder conditions or very fast flow beak ice forms which is characterised by single horn shapes.

1.1.3 Types of ice shape

In general, three types of ice accretion can be distinguished in flight conditions. They are characterised by their appearance and shape which are illustrated in figure 1.1 as given in Gent et al. (2000):

Rime ice: This type of ice is found in very cold conditions, if the droplet concentration is low or if the flow is slow. The release of kinetic energy on impact is not sufficient to heat the water droplets above $0\,^{\circ}\mathrm{C}$ in this case. The water freezes almost instantly when it impinges on the surface. The rapid process often traps air bubbles giving rime ice a milky opaque appearance. This type of ice accretion tends to be streamlined, however, as the accretion time increases, less aerodynamic pointed shapes form. (Gent et al., 2000)

Glaze ice: As temperature, the speed of the aircraft or the water concentration increases, the kinetic energy may become sufficient to heat the droplets above $0\,^{\circ}\mathrm{C}$ and a liquid water film forms on the impinging surface. The thin film of water moves under the shear stress exerted by the air flow around the surface. Subsequently, the film freezes by adiabatic cooling. This slow process yields a translucent ice formation.

Beak ice: Beak ice is typically found in conditions of fast air flow such as the tip region of a rotor. The adiabatic expansion of the fast airflow cools the impinging water droplets. This type of ice forms pointy horn shapes which disrupt the air flow and consequently the source of cooling and the ice breaks away (Gent et al., 2000).

1.1.4 Outside air temperature

The outside air temperature is the temperature of the undisturbed free stream air and is an essential factor in an ice accretion scenario for two reasons.

Firstly, the type of ice shape depends on whether the water droplets freeze instantly or remain liquid on impingement which depends on the droplet temperature. Sufficiently far away from the icing body, the droplets are assumed to be in thermal equilibrium with the surrounding air. Secondly, the colder the water droplets are, the more likely they are to freeze. This effect is more pronounced for larger droplets in which the probability of a nucleation seed is higher. Hence, colder droplets tend to be smaller.

1.1.5 Airspeed

The airspeed affects ice accretion in two ways. Firstly, the collection efficiency, which is the flux of water onto the icing body, increases as the speed increases. This is due to inertial forces becoming dominant over drag forces. Secondly, as the airspeed increases, the kinetic energy of the droplets and the effects of convective cooling increase, potentially resulting in a different type of ice formation (see figure 1.1).

1.1.6 Median volumetric diameter (MVD)

Clouds contain a distribution of droplet sizes. This is an essential factor since drag and inertial forces depend on the diameter. Moreover, the droplet temperature is related to the droplet size as it is difficult to maintain a supercooled state for a significant amount of water. Droplets of a diameter of the order of mm freeze spontaneously at $-20\,^{\circ}\mathrm{C}$ after a short time (Gent et al., 2000). Surface tension forces act to minimise the surface area and are proportional to the curvature of the surface. Pan et al. (2018) studied the relationship between the Weber number and the droplet deformation parameter. The Weber number is a dimensionless parameter defined as the ratio of inertial forces and surface tension forces. The droplet deformation parameter is the ratio of the greatest diameter of a deformed droplet over the diameter of a spherical droplet of the same volume. According to Pan et al. (2018), a maximum deformation parameter of 1.2 implies a critical Weber number of the order of 1. Assuming atmospheric conditions for water and air, this means that the deformations are small even for a relative velocity between the air and the droplets on the order of $10\,\mathrm{m\,s^{-1}}$. Therefore, water droplets are commonly assumed to remain spherical and are modelled as rigid spheres. In general, the drag law for rigid spheres depends in a non-linear manner on the diameter. Therefore, we expect significantly varying trajectories as the droplet size changes.

Inertial forces also depend non-linearly on the droplet diameter. Light droplets are swept past the icing body easily. The collection efficiency for small droplet diameters vanishes on large parts of the icing body and only a small region around the stagnation point obtains significant collection.

On the other hand, large and heavy droplets travel almost uninfluenced by the air flow. They follow an almost ballistic trajectory resulting in a large extent of water accumulation.

Based on these two extreme cases and the fact that the droplet diameter varies significantly in clouds, we conclude that an accurate model for the droplet distribution is essential.

1.1.7 Gravity

Gravitational effects tend to be less important and are often neglected in literature. Gravity comes into play when modelling the water droplet trajectories where buoyancy and body forces may play a role for large droplets (Gent et al., 2000). Wright and Potapczuk (2004) quantitatively analyse the effect of gravity on the water droplet trajectories by non-dimensionalising the governing equations. Even for large droplets, the Froude number, which is the ratio of inertia forces over gravitational forces, is on the order of 10^3. They, therefore, conclude that gravitational forces may be neglected. We follow this argumentation and neglect gravity for the droplet trajectory calculation.

Moreover, gravity also influences the water dynamics on the aircraft surface. This is the only aspect of the ice accretion process where we explicitly model gravitational effects.

1.2 Modules of icing simulations

The physical laws that govern the problem of ice accretion consist of two categories characterised by their length scale. Firstly, the external aerodynamic problem, which comprises the simulation of the air flow, the droplet flow and eventually the computation of the collection efficiency, occurs on a length scale typically given by the chord length of the aerofoil. Secondly, the ice growth, which includes the thin film dynamics of the water on the geometry and the freezing process, is expressed in terms of the ratio of the horizontal to the vertical extent of the water film and is typically orders of magnitude smaller than the length scale of the external aerodynamic problem. The two issues are coupled only by a few critical parameters as illustrated in figure 1.2. Based on this separation we divide our discussion into the following topics.

1.2.1 Air flow

The air flow computation provides input for two other calculations. Firstly, the droplet flow is governed by the drag which depends on the velocity field of the air flow. Secondly, the ice growth and thin film dynamics depend on air pressure p_A, air temperature T_A, shear stress τ and heat transfer

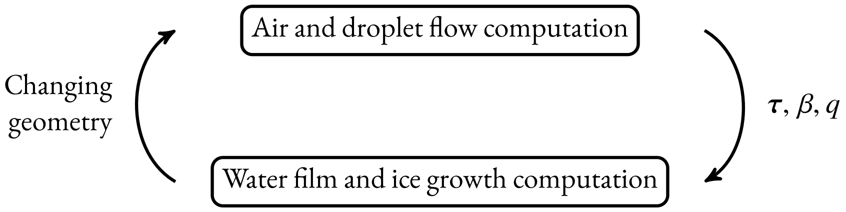

Figure 1.2: Illustration of the modular structure of ice accretion simulations. The air and droplet flow occurs on a larger length scale, typically the chord length of the icing body, than the water film. Hence, the full ice accretion process can be divided into two subproblems. Initially, the air and water droplet flow is computed giving parameters which are needed for the ice accretion such as collection efficiency β, shear stress τ and heat flux Q. Subsequently, the water film and ice extent is updated resulting in a slightly altered rigid geometry, which in turn changes the air and droplet flow.

coefficient h_c on the geometry surface. One of two approaches are commonly pursued to compute the air flow. Gent et al. (2000) termed these: *Coupled methods* and *Navier-Stokes methods*.

Coupled methods

Coupled methods make use of the large Reynolds number of the external aerodynamics problem and model the air as an inviscid flow. This approach gives accurate results for global parameters such as drag coefficients c_D and lift coefficients c_L for streamlined bodies (e.g. aerofoils). The parameters τ and h_c, which can only be determined by viscous methods, can be recovered by boundary layer methods in a subsequent calculation as done by Ruff and Berkowitz (1990). This approach effectively decouples the global air flow from the region close to the surface which is occupied by the boundary layer and allows the air flow to be modelled by the Euler equations with the ideal gas equation of state. One of the advantages of this approach is the low computational cost of solving the Euler equations as opposed to the viscous Navier-Stokes equations. On the downside, as the ice shape becomes more complicated, integral methods fail to predict the boundary layer accurately.

Viscous methods

These methods model the air flow with the viscous Navier-Stokes equations. In order to recover quantities such as shear stress, the simulation needs to resolve features smaller than a wall unit which is a length non-dimensionalised by the shear velocity and kinematic viscosity (Shan et al., 2005). In practical applications this is infeasible and approximations are used. Most commonly the Reynolds Averaged Navier-Stokes (RANS) equations with a turbulence model are solved. The RANS equations are derived from the Navier-Stokes equations by Reynolds decomposing the solution. Let $u(t,x,y,z)$ be the solution. The Reynolds decomposition is given by $u(t,x,y,z) = \bar{u}(x,y,z) + u'(t,x,y,z)$, where $\bar{u}$ is the time average and u' the fluctuating part of u. This approach gives rise to an extra term which is only expressed in terms of u'. There are various approaches to model the additional term such as the mixing length model, the Spalart-Allmaras model, the k-ε model and the k-ω model (Versteeg and Malalasekera, 2007). These methods are computationally more expensive than coupled methods but they tend to be more accurate especially for complicated geometries. RANS methods were employed by Bourgault et al. (2000b) using FENSAP-ICE with a k-ε turbulence model and da Silveira et al. (2003) using a Spallart-Almars turbulence model.

Mesh generation

Both methodologies require a high-quality grid on which the equations are discretised (Gent et al., 2000). Independent mesh generators create a grid around the icing body and need to be run before the fluid solver. While this process can take up a significant part of the simulation time, it is a feasible approach in conventional external aerodynamics simulations as the geometry is static and the mesh is generated only once. In ice accretion simulations, however, this approach fails for two reasons.

Firstly, geometries change due to growing ice layer thickness which requires continuous updating of the mesh. Current generation ice prediction software circumvents this problem by introducing a user-specified parameter Δt_{remesh}. It is assumed that the geometry does not change significantly in this time interval and hence remesh only every Δt_{remesh}. After a geometry update, the air and droplet solver computes the steady state solution, and the results are used for the next time step. Verdin (2007); Verdin et al. (2009); Verdin and Charpin (2013) extended this approach by using a predictor-corrector method. They concluded that the repeated steady-state computation uses significant computational resources and that a moving boundary approach may lead to a more efficient methodology (Verdin, 2007).

Secondly, as the ice grows, the surface shape becomes more complicated. Most grid generators produce a highly skewed mesh, especially in regions of high surface curvature e.g. in glaze ice conditions (see figure 1.1).

1.2.2 Droplet flow

In this section, we present the two most commonly used approaches to compute the droplet flow and the collection efficiency of a geometry. Classically, only clouds which consist of droplets of diameter less than $50\,\mu\text{m}$ are studied. This class does not include SLDs. Hence, droplet break-up, coalescence and ricocheting are not taken into account in the following models. Due to the small

LWC, it is generally assumed that droplets only interact with the surrounding air and not with one another. This assumption leads to two notions in the description of droplet flow: *Lagrangian droplet tracking* and *Eulerian droplet flow*.

Lagrangian droplet tracking

In the Lagrangian frame, droplets are tracked individually solving a governing equation for every single droplet. The forcing term in the equation of motion is given by the drag law $\boldsymbol{D}_\mathrm{L}$, which is given by the aerodynamic drag of rigid spheres as the droplets are assumed not to deform. This gives the equation of motion:

$$m \frac{\mathrm{d}^2 \boldsymbol{x}}{\mathrm{d}t^2}(t) = \boldsymbol{D}_\mathrm{L} \,, \tag{1.1}$$

where m is the mass of one water droplet and is a function of the droplet diameter, $\boldsymbol{x}$ is the position of the droplet parameterised by t, and $\boldsymbol{D}_\mathrm{L}$ is the drag law for a rigid sphere. The drag vanishes in the case of velocity equilibrium which is satisfied if the drag force depends only on the relative velocity of the droplets in the air flow. Two water droplets which were released in the vicinity of each other but infinitely far away from the aerofoil are commonly referred to by *representative droplets*. As we track those droplets, they enclose an area called a *stream tube* between their trajectories. Since the quantity of water within the stream tube is conserved, we can compute the LWC at the time of impingement using the ratio of the distances between two representative droplets infinitely far away and at impingement. The non-dimensionalised collection efficiency $\hat{\beta}$ is given by

$$\hat{\beta} = \frac{\Delta s_\infty}{\Delta s_\mathrm{imp}} \,, \tag{1.2}$$

where Δs_∞ is the distance between two representative droplets in the far field, and Δs_imp the distance between the droplets at the time of impingement.

Eulerian droplet flow

The Eulerian approach averages the water droplets over a control volume and models them as a continuum. This idea is analogous to the description of the air flow, which makes it easy to solve in the same framework. Due to the non-interaction assumption, a pressure-like quantity vanishes.

Therefore, the governing equations are

$$\partial_t \rho + \nabla_i \rho v^i = 0\,, \tag{1.3}$$
$$\partial_t \rho v^i + \nabla_j \rho v^i v^j = D^i_{\mathrm{E}}\,, \tag{1.4}$$

where ρ is the density of water and v the velocity. These equations, however, are weakly hyperbolic and the eigenvectors of the Jacobian do not span the whole solution space. For example, δ-shocks are a valid solution to some initial conditions, therefore making the equations difficult to solve numerically. However, as pointed out by Pelanti and LeVeque (2006), these numerically challenging solutions do not appear in practical situations due to the relaxation effect of the coupling with the air flow. A much more detailed discussion of the droplet flow can be found in Wutschitz (2014).

The equivalence of the Eulerian and the Lagrangian approach can easily be shown by expanding equation (1.4) and substituting equation (1.1). Without loss of generality, the expressions are considered in a Cartesian frame.

$$D^i_{\mathrm{E}} = \partial_t \rho v^i + \partial_j \rho v^i v^j = v^i \underbrace{\left(\partial_t \rho + \partial_j \rho v^j\right)}_{0} + \rho\left(\partial_t v^i + v^j \partial_j v^i\right) = \rho \frac{\mathrm{d}v^i}{\mathrm{d}t} = \frac{\rho}{m} D^i_{\mathrm{L}}\,. \tag{1.5}$$

The scaling factor ρ/m converts the drag term of a single droplet in the Lagrangian picture to the drag per unit volume required in the Eulerian picture.

1.2.3 Ice growth

Following the air and droplet flow simulation, we turn to the processes occurring on the icing body. The kinetic energy released on impact, convective cooling and other energy transfer mechanisms add up to an energy balance determining whether the impinging water droplet freezes or remains liquid. This process is essential for an accurate description of the ice shape. The majority of ice accretion simulation uses all or a subset of the following heat transfer processes which depend mainly on the water temperature T_{w}, the air temperature T_{a} and droplet temperature T_{d}:

Evaporation/Sublimation: Evaporation and sublimation of the water and ice, respectively, extracts heat. Typically, a linear approximation of this process is sufficient (Poots and Skelton, 1992; Myers and Hammond, 1999; Lowe, 1976). Consequently, a single evaporation coefficient governs the energy flux (Chilton and Colburn, 1934; Myers and Hammond, 1999).

Convective cooling: Convective cooling by the air flow is the main contributor to the formation of glaze ice as it is the most dominant heat exchange mechanism. The heat transfer coefficient h_c is a crucial parameter in this process and is obtained from the boundary layer model.

Droplet cooling: As the water droplets impinge on the film, they are assumed to reach temperature equilibrium. The energy required to heat them is extracted from the system. This process is dependent on the temperature of the impinging droplets T_d. However, it is commonly replaced by the free stream temperature T_∞ since it is assumed that the temperature of the droplets does not change.

Latent heat: Latent heat is released in a phase transition. In our case energy is released as the liquid water film freezes.

Kinetic energy from water: Upon impingement the kinetic energy is converted into heat and contributing to the energy balance.

All these contributions sum to an energy balance yielding a differential equation for the ice height ζ. A definition and more detailed discussion of the energy balance and the individual terms will be presented in section 4.7.

The Messinger model

The first attempt to describe the ice growth process dates back to the pioneering work of Messinger (1953). Many icing accretion simulation suites, including LEWICE and CANICE, are based on this model (Özgen and CanIbek, 2009; Wright, 2008; Morency et al., 1999). The approach of Messinger utilises control volumes and keeps a mass balance. The mass of liquid water in a control volume changes either by

1. impingement,
2. influx from a control volume upstream,
3. freezing,
4. outflux back to a control volume downstream.

The algorithm starts with the control volume at the stagnation point. Since contribution 2 vanishes, the only source of water is droplet impingement. The amount of liquid water is determined by the energy balance described earlier and is assumed to flow into the control volume downstream during the next time step. The flux of water is also often referred to by *water runback*. While this approach is successful for the prediction of rime ice Gent et al. (2000) concluded that the Messinger model is not sufficient for a realistic simulation of the water film and that a more sophisticated description is required. This is due to the unstable nature of a thin water film which frequently exhibits features that a control volume approach cannot capture such as finger formation. Myers and Hammond (1999); Myers et al. (2002a,b) developed a model based on lubrication theory and a dynamic boundary condition between the ice and the water — the Stefan condition.

The Stefan approach

There are two notable developments which extend the Messinger control volume approach. Firstly, Bourgault et al. (2000a) derived a set of governing equations based on the shallow water system called Shallow-Water Icing Model (SWIM). This set of equations is derived from the inviscid Euler equations under the assumption that variations of the solution in the direction perpendicular to the substrate are negligible. Myers and Hammond (1999) derived a set of partial differential equations which govern the thin film flow of water by reducing the Navier Stokes equations using lubrication theory. Since the latter approach includes surface tension terms and pressure gradients, phenomena such as finger formation can be described (Schwartz, 1989). However, Myers et al. (2002a) neglect inertia terms which are modelled in SWIM. These terms are commonly neglected in relatively slow flows such as gravity-driven coating applications but whether this assumption holds for aircraft icing is debatable.

1.2.4 Time stepping

The growing ice layer changes the air flow. This needs to be taken into account by recomputing the air flow and updating air flow and droplet parameters. Updating the air flow solution for a slightly different geometry, however, means remeshing the domain. This is computationally expensive and infeasible if done frequently. Early simulations were limited to a study of only small accretions, where the ice layer remains thin and does not alter the geometry significantly. Recent advancements in computing technology made remeshing possible. However, adapting the grid is still computationally expensive and cannot be done frequently, resulting in a discontinuous time evolution of the geometry (Bourgault et al., 2000b). Recently, Leese (2010) proposed an overlapping grid approach where only the region of the grid which covers the ice growth needs to be remeshed. This approach worked well for simple cases such as cylinders but it is difficult to extend to more complicated shapes such as multi-component aerofoils.

1.3 Previous work

In this section, we review the major current generation icing codes and explain which models they use for the individual modules discussed above.

LEWICE: Developed within the Glenn Research Center, formerly the NASA Lewis Research Center, in 1983, LEWICE is the most widely used ice accretion prediction software. Initially, incompressible panel methods and simple droplet tracking and ice growth models were employed, however, LEWICE was extended in many ways and is now one of the most comprehensive packages (Wright, 1995, 2008; Ruff and Berkowitz, 1990; Wright and Rutkowski, 1999; Potapczuk et al., 1993; Wright and Potapczuk, 2004). Extensions include: an improved air flow solver using a RANS approach with an algebraic eddy viscosity model developed by Potapczuk (1989); Potapczuk et al. (1993), and the ability to model super large droplet dynamics by Wright and Potapczuk (2004).

ONERA: The software of *Office National d'Etudes et de Recherches Aérospatiales* (ONERA) is known as the *ONERA icing code* and is used by Airbus (Bartels et al., 2015) among others. Similarly to the efforts by the Glenn Research Center, the ONERA code started with elementary models. It comprises an inviscid Euler model for the air flow, a Lagrangian method for the collection efficiency and a classical runback model based on Messinger's approach.

CANICE: Developed at *École Polytechnique Montreal* by order of Bombardier Aerospace (Paraschivoiu and Saeed, 2001), CANICE uses a simple and efficient panel methods with the Karman-Tsien compressibility correction, a Lagrangian droplet approach, and Messinger's model to determine runback (Saeed et al., 2001).

FENSAP-ICE: Developed as a commercial package by *Newmerical Technologies*, it comprises a RANS solver with a one or two-equation turbulence model for the air flow (Beaugendre et al., 2003), a Eulerian droplet solver (Bourgault et al., 2000b) and an ice growth module based on the shallow water equations (Bourgault et al., 2000a). Newmerical Technologies was acquired by ANSYS in 2005 which is now providing FENSAP-ICE.

ICECREMO3: Developed by a collaborative research partnership at Cranfield University, ICECREMO uses Lagrangian droplet tracking on inputs from external aerodynamics solvers. The phase transition is computed using the thin film approach by Myers et al. (2002a).

Package	Air solver	Boundary layer method	Droplet solver	Water dynamics
LEWICE	Panel + compr	Integral	Lagrangian	Messinger
ONERA	Euler	Mixing length	Lagrangian	Messinger
CANICE	Panel + compr	Integral	Lagrangian	Messinger
FENSAP-ICE	RANS	RANS	Eulerian	SWIM
ICECREMO3	RANS	RANS	Lagrangian	Thin film

Table 1.1: Overview of the models used by current generation icing codes

1.4 Conclusions of literature review

In this chapter, we have motivated the need for a robust and accurate methodology to predict ice accretion in in-flight conditions. Section 1.1 gives a brief description of the physical phenomena involved and highlights the challenges concerning numerical prediction.

Subsequently, we have introduced the components of ice accretion simulation packages and presented common modelling choices. A recurring issue is the failure of mesh generation routines to cope with the complicated geometries arising from the ice layer. The computational mesh is commonly updated infrequently (Verdin et al., 2009; Cao and Huang, 2014), or only simple icing bodies are studied (Leese, 2010). The collection efficiency is computed using Lagrangian or Eulerian approaches, but in both cases the droplets are assumed to only interact with the air according to the rigid sphere drag law. There have been extensions to conventional methodologies to account for SLDs, but most of them are of empirical nature. Recently, a promising novel approach based on quasi-molecular modelling has been proposed (Abdollahi et al., 2016). However at the moment, it seems to be too computationally expensive to be integrated into full ice accretion simulations.

Section 1.2.3 introduced the commonly used models for computation of the ice extent. Most implementations are still based on the approach by Messinger. Recently, more comprehensive models have been proposed based on the shallow water equations and thin film theory. Both of these methodologies, however, make simplifying assumptions which are not yet well studied. Further investigation is needed to determine the suitability of these models for the integration of full ice accretion simulations.

1.5 Thesis outline

Chapter 2 addresses the issue of the mesh generation bottleneck commonly found in in-flight ice accretion simulations. We present a methodology to compute air and water droplet flow based on a

Cartesian cut-cell routine. This novel approach allows us to study complex geometries while still providing fast mesh generation. The accuracy of the scheme is assessed by computing the air flow over several aerofoils. Subsequently, the scheme is integrated with an Eulerian droplet solver. Since this phase poses a challenge for solvers, we give a detailed analysis of the numerical methodology. In particular, the non-negativity preservation of the scheme is shown analytically. Finally, we validate the two-phase system by computing collection efficiencies around a cylinder, a sphere and an aerofoil. The meshing capability is demonstrated by simulating a showcase study of air and droplet flow over a realistic automotive body.

The second part of chapter 2 extends the model for the air and droplet flow giving a novel approach in the context of in-flight ice accretion simulations. Although the droplets are still modelled as rigid spheres, we include heat exchange terms in the governing equations. We present validation cases and assess the performance of our novel model by comparing it and conventional systems with experimental data. We find that the results of our novel approach agree significantly better with experimental data than conventional models. Finally, we present results for a multi-element aerofoil in in-flight conditions and observe a significant increase in droplet impingement temperatures of up to 4 K.

Chapter 3 provides details about the implementation of the coupling between the air and droplet flow routines, and the thin film solver of chapter 4. Interpolation routines are introduced and are applied to the transfer of data from the Cartesian cut-cell mesh to the mapped surface grid. Subsequently, the integral boundary layer method is described and results are qualitatively compared with computational data from literature.

The introduction of chapter 4 gives a review of surface ice accretion models. We conclude that none of the reviewed approaches stands out as the best candidate. The thin film methodology by Myers et al. (2002a) promises the most accurate results, however, further investigation is required into inertia terms and the order of truncation of the perturbation expansion. A model which does not assume an internal equilibrium was proposed by Rothmayer et al. (2002), however, it is not yet suitable to be used in an integrated ice accretion prediction.

The second part of chapter 4 generalises the thin film model to a more general class of surface parameterisations and extends the perturbation expansion to consistently include first order terms. A test case studying a gravity-driven thin flow around a cylinder is used to assess the performance of the extended scheme. We observe significantly more accurate results using the generalised model and conclude that first order terms play a pivotal part in the dynamics of the thin film. Finally, the heat flux computation at the free surface is extended to account for droplet temperatures made available by the improvements presented in chapter 2.

Finally, chapter 5 combines the methodologies introduced in chapter 2 – 4 to give a full ice accretion system. The performance of the final system is assessed by considering established ice accretion benchmark test cases. Ultimately, the methodology is extended to continuously moving boundaries.

1.6 Conventions and notation

Throughout this thesis, we try to keep variable names and conventions as consistent as possible. Some of the conventions appear repeatedly and are used in most chapters.

Einstein summation convention

The Einstein summation convention is used throughout this thesis. Whenever the same index of a vector or higher rank tensor appears in covariant and contravariant form in the same term, a summation over this index is implied. Unless otherwise stated, the summation ranges over $1, \dots, N$ for Latin indices, where N is the number of global dimensions, and over $1, \dots, N-1$ for Greek indices.

Labelling of quantities

Due to the many phases involved in this problem, some quantities exist for multiple phases. In general, we reserve upright lower case labels to denote individual phases. $\cdot_\mathrm{a}$ refers to air phase quantities, $\cdot_\mathrm{d}$ to droplet variables, $\cdot_\mathrm{w}$ to liquid water quantities, and $\cdot_\mathrm{i}$ ice variables.

Moreover, $\underline{\cdot}$ denote quantities on the substrate, $\bar{\cdot}$ on the ice-water interface, and $\tilde{\cdot}$ at the air-water interface.

States that are assumed to be infinitely far away, i.e. free stream quantities, carry a $\cdot_\infty$ subscript.

Finally, non-dimensionalised variables are labelled by $\hat{\cdot}$.

Chapter 2

Modelling of water droplet and air flow

The simulation of air and water droplet flow around an icing body is an important initial step towards a complete numerical description of the icing phenomenon. The next step in the process is the calculation of the collection efficiency β, which is the flux of water onto the geometry and it describes where and how much water impinges onto the icing body. The accurate computation of temperatures in this process is particularly important as it is an essential quantity in the determination whether the supercooled water droplets remain liquid or freeze on impact.

2.1 Introduction

Both industry leading icing simulation packages such as LEWICE (Wright, 2008) and FENSAP-ICE (Bourgault et al., 2000b) and more recent academic research by Jung and Myong (2013) Kim et al. (2013) and Capizzano and Iuliano (2014) treat the air and the water droplets as independent systems and the only coupling arises from drag forces which are exerted onto the droplets as they flow through the air. Thereby, keeping the water droplet temperature constant throughout the process. However, since the droplet temperature upon impingement is a crucial quantity for the process of freezing, accounting for droplet temperature variation is likely to improve the accuracy of an ice accretion simulation. To this end, we develop a methodology based on the model by Miura and Glass (1988), Saito (2002), and Pelanti and LeVeque (2006) which is able to differentiate the temperature of the air and water droplet phases.

Lagrangian approaches as in Morency et al. (1999) and Al-Khalil et al. (1997), and Eulerian approaches as developed by Jung and Myong (2013), Bourgault et al. (2000b), and Capizzano and Iuliano (2014) have been employed to solve the droplet flow equations. The equations governing the droplet flow in an Eulerian frame are called the pressureless Euler equation and a lot of theoretical research has been done on their mathematical structure. A rigorous and comprehensive analysis was discussed in Bouchut (1994) and Sheng and Zhang (1999). The analytical solution for these equations for the Riemann problem can contain vacuum states and numerical methods need to deal with it robustly. Numerical problems manifesting as negative densities occurring next to steep gradients or behind shading geometries were reported by LeVeque (2004), and Jung and Myong (2013). We will address this issue by showing that our numerical method, provided that the common CFL condition is met, is non-negativity preserving.

An integral part of the calculation is the representation of the icing body in discrete space, i.e. the mesh generation around the aerodynamic body. Mesh generation approaches include boundary conforming grids (da Silveira and Maliska, 2001; Al-Khalil et al., 1997; Morency et al., 1999; Bourgault et al., 2000b; Kim et al., 2013; Jung and Myong, 2013) and unstructured meshes (Batina, 1990; Abgrall, 1994).

Cartesian cut-cell techniques have gained popularity (Klein et al., 2009; Gokhale et al., 2018; Berger and Aftosmis, 2012; Colella et al., 2006) due to the relative ease with which good quality meshes are generated. These techniques promise low computational cost and straightforward parallelisation even for very complex geometries. Properties like that make the cut-cell approach a promising candidate for icing simulations in which the unpredictable geometry movement poses a particular challenge to mesh generation algorithms. Recently an immersed boundary method which is also based on a Cartesian mesh and shares many of the favourable properties with cut-cell methods has been applied to water droplet flow by Capizzano and Iuliano (2014).

Using the cut-cell methodology, the mesh away from the solid body remains rectangular, while cells of arbitrary shape and size are generated at the intersection of the solid body with the regular Cartesian mesh. Various numerical methodologies have been developed for the solution of the fluid flow equations at these irregular cells (Klein et al., 2009; Gokhale et al., 2018; Aftosmis et al., 2000; Hartmann et al., 2008) but the solution of the droplet flow equations, and the implementation of their boundary conditions has yet to be addressed. Key quantities for the icing process are extracted at the solid boundary which is discretised by the irregular cut-cells. An assessment of the quality of the solution of our proposed formulation is an essential part of this chapter.

2.1.1 Outline of this chapter

The remainder of this chapter is structured as follows: In section 2.2 the set of equations is introduced which governs collection efficiency and allows tracking of droplet temperatures. The employed model was used to study collection efficiencies in the author's Masters thesis (Wutschitz, 2014). For this reason, we only give a brief summary of the equations. However, substantial improvements were made to the numerical methods and solvers compared to the previous work and only novel results are presented in this chapter. An improved cut-cell method is used which is briefly summarised in section 2.3. This section also contains a discussion addressing the non-negativity preservation property of the method and introduces a modified flux stabilisation for the droplet phase. The proposed methodology is validated by comparing against experimental data and other numerical simulations in section 2.4. Finally, in section 2.5.2 a for ice accretion relevant case study is presented highlighting the capabilities of this formulation.

2.2 Mathematical models

The governing equations are based on the conservation of mass, momentum and energy of the air and the droplets. The droplets are sparse in the domain hence interaction between one with one another is neglected. The diameter of supercooled water droplets found in icing situation are typically of the order of $10\,\mu\text{m}$. Due to the high curvature of the air-water interface it is assumed that surface tension forces keep the droplets spherical. Hence, we model them as rigid spheres with constant microscopic density ρ_d. The particulate phase is coupled with the carrier phase by heat and momentum exchange. The interaction between the droplets and the air is described in section 2.2.2 and depends non-linearly on the droplet diameter. Typically, a distribution of droplet diameters is found in icing situations. In order to represent varying sizes, we divide the distribution into S bins. A representative diameter d_s is associated with every group and has its own set of equations[1].

---

[1] Throughout this article the index $\cdot_s$ is used to label a droplet quantity with diameter d_s. For the sake of brevity equations are not repeated for different droplet diameters.

2.2.1 Governing equations

Based on the assumptions presented in the previous subsection Saito (2002) proposed the following governing equations:

$$\begin{aligned}
\partial_t \alpha_a \rho_a + \nabla \cdot \alpha_a \rho_a \boldsymbol{v}_a &= 0\,, && (2.1a)\\
\partial_t \alpha_a \rho_a \boldsymbol{v}_a + \nabla \cdot \alpha_a \rho_a \boldsymbol{v}_a \otimes \boldsymbol{v}_a + \nabla \alpha_a p_a &= \sum_s \boldsymbol{D}_s(\boldsymbol{\Delta v}_s)\,, && (2.1b)\\
\partial_t \alpha_a E_a + \nabla \cdot \alpha_a (E_a + p_a) \boldsymbol{v}_a &= \sum_s \boldsymbol{D}_s(\boldsymbol{\Delta v}_s) \cdot \boldsymbol{v}_s + \sum_s Q_s(\Delta T_s)\,, && (2.1c)\\
\partial_t \alpha_s \rho_s + \nabla \cdot \alpha_s \rho_s \boldsymbol{v}_s &= 0\,, && (2.1d)\\
\partial_t \alpha_s \rho_s \boldsymbol{v}_s + \nabla \cdot \alpha_s \rho_s \boldsymbol{v}_s \otimes \boldsymbol{v}_s &= -\boldsymbol{D}_s(\boldsymbol{\Delta v}_s)\,, && (2.1e)\\
\partial_t \alpha_s E_s + \nabla \cdot \alpha_s E_s \boldsymbol{v}_s &= -\boldsymbol{D}_s(\boldsymbol{\Delta v}_s) \cdot \boldsymbol{v}_s - Q_s(\Delta T_s)\,, && (2.1f)
\end{aligned}$$

where ρ is the density, $\boldsymbol{v}$ the velocity, p the pressure, E the total energy per unit volume, $\boldsymbol{D}_s$ the momentum exchange term for droplets with diameter d_s and Q_s the heat exchange term. The heat and the momentum exchange functions only depend on the relative velocities $\boldsymbol{\Delta v}_s = \boldsymbol{v}_s - \boldsymbol{v}_a$ and temperatures $\Delta T_s = T_s - T_a$. The subscript $\cdot_a$ denotes the air phase and the index $\cdot_s$ the droplet phase with droplet diameter d_s where $s = 1, \ldots, S$. α is the volume fraction occupied by the indicated phase. Consistency requires

$$\alpha_a + \sum_s \alpha_s = 1\,. \tag{2.2}$$

For every phase, the total energy E is related to specific internal energy e and temperature T by

$$E = \rho\left(\frac{1}{2}v^2 + e\right)\,, \qquad e = c_v T\,, \tag{2.3}$$

where c_v is the heat capacity at constant volume and assumed to remain constant. The set of governing equations (2.1) can be decomposed into a system of conservation laws for the gas and the droplet phase:

$$\begin{aligned}
\partial_t \boldsymbol{u}_a + \nabla_i \boldsymbol{f}_a^i(\boldsymbol{u}_a) &= \boldsymbol{S}_a(\boldsymbol{u}_a, \boldsymbol{u}_s)\,, && (2.4a)\\
\partial_t \boldsymbol{u}_s + \nabla_i \boldsymbol{f}_d^i(\boldsymbol{u}_s) &= \boldsymbol{S}_s(\boldsymbol{u}_a, \boldsymbol{u}_s)\,, && (2.4b)
\end{aligned}$$

where $\boldsymbol{u}$ are the state vectors, $\boldsymbol{f}$ the flux functions and $\boldsymbol{S}$ the source terms and are given by

$$\boldsymbol{u}_{\mathrm{a}}=\begin{pmatrix}\alpha_{\mathrm{a}}\rho_{\mathrm{a}}\\ \alpha_{\mathrm{a}}\rho_{\mathrm{a}}\boldsymbol{v}_{\mathrm{a}}\\ \alpha_{\mathrm{a}}E_{\mathrm{a}}\end{pmatrix},\ \boldsymbol{f}_{\mathrm{a}}^{i}(\boldsymbol{u}_{\mathrm{a}})=\begin{pmatrix}\alpha_{\mathrm{a}}\rho_{\mathrm{a}}v_{\mathrm{a}}^{i}\\ \alpha_{\mathrm{a}}\rho_{\mathrm{a}}\boldsymbol{v}_{\mathrm{a}}v_{\mathrm{a}}^{i}\\ \alpha_{\mathrm{a}}(E_{\mathrm{a}}+p_{\mathrm{a}})v_{\mathrm{a}}^{i}\end{pmatrix},\ \boldsymbol{S}_{\mathrm{a}}(\boldsymbol{u}_{\mathrm{a}},\boldsymbol{u}_{s})=\begin{pmatrix}0\\ \sum_{s}\boldsymbol{D}_{s}\\ \sum_{s}(\boldsymbol{D}_{s}\cdot\boldsymbol{v}_{s}+Q_{s})\end{pmatrix}, \tag{2.5a}$$

$$\boldsymbol{u}_{s}=\begin{pmatrix}\alpha_{s}\rho_{d}\\ \alpha_{s}\rho_{d}\boldsymbol{v}_{s}\\ \alpha_{s}E_{s}\end{pmatrix},\ \boldsymbol{f}_{\mathrm{d}}^{i}(\boldsymbol{u}_{s})=\begin{pmatrix}\alpha_{s}\rho_{s}v_{s}^{i}\\ \alpha_{s}\rho_{s}\boldsymbol{v}_{s}v_{s}^{i}\\ \alpha_{s}E_{s}v_{s}^{i}\end{pmatrix},\ \boldsymbol{S}_{s}(\boldsymbol{u}_{\mathrm{a}},\boldsymbol{u}_{s})=\begin{pmatrix}0\\ -\boldsymbol{D}_{s}\\ -\boldsymbol{D}_{s}\cdot\boldsymbol{v}_{s}-Q_{s}\end{pmatrix}. \tag{2.5b}$$

The homogeneous parts of the phases are independent of each other. The interaction between the phases is explicitly modelled by source terms which are integrated by means of operator splitting. This decomposition allows us to treat the homogeneous portion effectively as a single-phase flow. In the remainder of this section the individual components of the governing equations are discussed.

2.2.2 Coupling terms

The source terms $\boldsymbol{S}$ model the coupling between the droplet and the carrier phases. Since

$$\boldsymbol{S}_{\mathrm{a}}+\sum_{s}\boldsymbol{S}_{s}=0\,, \tag{2.6}$$

total mass, momentum and energy are conserved. Two means of interaction are modelled: heat exchange and momentum exchange.

Droplet drag law

Aerodynamic drag governs the momentum exchange between the droplets and the carrier phase and is given by

$$\boldsymbol{D}_{s}(\Delta\boldsymbol{v}_{s})=\frac{3\,C_{\mathrm{D}}\,\alpha_{s}\,\rho_{\mathrm{d}}\,\alpha_{\mathrm{a}}}{4\,d_{s}}\,||\Delta\boldsymbol{v}_{s}||\,\Delta\boldsymbol{v}_{s}\,, \tag{2.7}$$

where C_{D} the drag coefficient. The drag $\boldsymbol{D}_{s}$ respects the natural limits. It vanishes in mechanical equilibrium of the two phases i.e. $\Delta\boldsymbol{v}_{s}=0$ and is symmetric about the origin. The Reynolds number Re is defined as the ratio of inertial forces to viscous forces. For an air flow around a particle of diameter d_{s}, Re_{s} is given by

$$\mathrm{Re}_{s}=\frac{||\Delta\boldsymbol{v}_{s}||\,d_{s}\,\rho_{\mathrm{a}}}{\mu_{\mathrm{a}}}\,, \tag{2.8}$$

where μ_a is the dynamic viscosity of air. Throughout this work we assume that μ_a is constant. Since the droplet diameter are small the forces are dominated by surface tension which suggests we can assume that the droplet surface is approximately minimal. Hence, the drag coefficient C_D of a rigid sphere is used. An empirical relation for the drag coefficient of a rigid sphere in a viscous fluid with a no-slip boundary condition is given by

$$C_\mathrm{D}(\mathrm{Re}) = \begin{cases} \frac{24}{\mathrm{Re}}\left(1 + 0.15\,\mathrm{Re}^{0.687}\right) & \mathrm{Re} < 1300 \\ 0.4 & \mathrm{Re} \geq 1300 \end{cases} . \tag{2.9}$$

This expression is only valid for approximately $\mathrm{Re} < 10^5$. Beyond this threshold a transition to turbulent flow occurs. However, Leese (2010) argued that even for large droplets (on the order of $d = 100\,\mu\mathrm{m}$) and fast flows (on the order of $||\boldsymbol{\Delta v}|| = 100\,\mathrm{m\,s^{-1}}$) the Reynolds number does not exceed 10^5. For even larger droplets the minimal surface assumption breaks down and other effects such as droplet break-up and splashing need to be modelled which are beyond the scope of this work.

Heat transfer

The heat transfer function is given by

$$Q_s(\Delta T_s) = \frac{6\,\mathrm{Nu}_s\, k_\mathrm{a}\, \alpha_s}{d_s}\Delta T_s\,, \tag{2.10}$$

where Nu_s is the Nusselt number and k_a the thermal conductivity of air. Similarly to the droplet drag law in the previous section, the heat transfer function is odd and vanishes in thermal equilibrium. The energy exchange is expressed in terms of the Nusselt number which is defined by the ratio of convective heat transfer and conductive heat transfer and is given by

$$\mathrm{Nu}_s = \frac{h\, d_s}{k_\mathrm{a}}\,, \tag{2.11}$$

where h is the convective heat transfer coefficient with dimensions of power over area. Knudsen and Katz (1958) reviewed empirical relations for the Nusselt number for the forced heat convection of spheres. An over a wide range of Reynolds numbers applicable relation is given by

$$\mathrm{Nu}_s = 2 + 0.6\,\mathrm{Re}_s^{\frac{1}{2}}\,\mathrm{Pr}^{\frac{1}{3}}\,, \tag{2.12}$$

where Pr is the Prandtl number which is defined as the ratio of viscous diffusion and thermal diffusion and is given by

$$\mathrm{Pr} = \frac{c_{\mathrm{pa}}\mu_{\mathrm{a}}}{k_{\mathrm{a}}}\,, \tag{2.13}$$

where c_{pa} is the specific heat capacity of air at constant pressure and assumed to be constant.

2.2.3 Homogeneous equations

Having discussed the coupling terms, we now turn to the homogeneous part of the equations. The air is modelled as an ideal gas. Hence, the closure relation is given by

$$p_{\mathrm{a}} = e_{\mathrm{a}}(\gamma_{\mathrm{a}} - 1)\rho_{\mathrm{a}}\,, \tag{2.14}$$

where γ_{a} is the ratio of specific heats of the gaseous phase and assumed to be constant.

Droplet flow

The governing equations for the droplet flow as they are given in the multi-phase model (2.1) are the Eulerian equivalent to particle tracking and are commonly referred to as the pressureless Euler equations. In one-dimensional quasi-linear form they read

$$\left(I_2\frac{\partial}{\partial t} + \begin{pmatrix} 0 & 1 \\ -v^2 & 2v \end{pmatrix}\frac{\partial}{\partial x}\right)\begin{pmatrix} \rho \\ \rho v \end{pmatrix} = \mathbf{0}\,. \tag{2.15}$$

The Jacobian of the flux function only has one distinct eigenvalues v and lacks a set of eigenvectors that spans the full solutions space. Therefore, the system is weakly hyperbolic and the standard theory of obtaining wave solutions does no longer apply. However, a measure valued solution based on a generalised Rankine Hugoniot condition can be formulated. A derivation using this approach in rigorous detail is given by Sheng and Zhang (1999). In conclusion, the degeneracy of the eigenvalues allows vacuum states and delta waves as solutions and makes the system difficult to solve robustly in an Eulerian frame. Appropriate numerical methods are required which we introduce in the next section.

2.3 Numerical methods

The conserved nature of the homogeneous governing equations suggests a finite volume scheme. Throughout this thesis, we solve these equations using the high-resolution Monotonic Upwind Scheme for Conservation Laws (MUSCL) Hancock flux method with an exact Riemann solver. This method adaptively chooses the order of reconstruction, thereby suppressing spurious oscillations of second order methods around discontinuities while reducing the error by using a second order reconstruction in regions of a smooth solution. Methods of higher order than two require stencil sizes of more than five cells which is incompatible with the employed cut-cell methods and is topic of ongoing research. Riemann problem based methods are generally more accurate, albeit, computationally more expensive. Very efficient Riemann solvers exist for the ideal gas Euler equations and for the droplet phase even a closed form solution exists. Therefore, we decided not to use centred methods and instead rely on Riemann problem based flux methods. Here we only introduce the novel aspects of the stabilisation methodology required by the cut-cell space discretisation and the solution strategy for the coupling terms. More details about the implementation of Riemann solvers and its application for the ideal gas and pressureless Euler equations can be found in Wutschitz (2014); Wutschitz and Nikiforakis (2016); Toro (2009).

2.3.1 Non-negativity preservation

Droplet concentration may vanish in regions of the computational domain e.g. when the flow is shaded by the solid geometry. This behaviour poses a difficulty to Eulerian solvers since they have to deal robustly with vacuum states and arbitrarily small droplet concentrations. Numerical problems arising from vacuum states manifesting as negative densities were reported by LeVeque (2004) and Jung and Myong (2013). LeVeque corrected this shortcoming of Eulerian methods by checking for negative densities and replacing them with a fixed value of 10^{-20} after every time step. This approach violates conservation of mass, albeit, to negligible orders for practical applications. Jung and Myong (2013) proposed a modification to the governing equations. They introduced a perturbation which renders the system strictly hyperbolic and resembles the shallow water equations for which positivity preserving solvers exist. Subsequently, the perturbation was corrected in a source routine. Unfortunately, no claims about the positivity preservation properties of the source solver were made.

The use of an appropriate method eliminates the requirement of perturbing the original system. To this end, we show that the Godunov method with an exact Riemann solver is non-negativity preserving. This result can be used to devise a non-negativity preserving high resolution method.

Perthame and Shu (1996) construct a non-negativity preserving high order method provided a non-negativity preserving first order scheme exists.

The non-negativity of the density can be shown by extending the analysis by Einfeldt et al. (1991). We use the exact solution to the Riemann problem for the pressureless Euler equations derived by Bouchut (1994). He solves the equations by interpreting the mass m as a measure. The update formula for the Godunov method for a computational cell $\mathscr{C}$ then becomes

$$\rho^{n+1} = \frac{1}{|\mathscr{C}|} m^{n+1}(\mathscr{C})\,, \tag{2.16}$$

where the measure is defined as

$$m^{n+1}(\mathscr{C}) := \int_{\mathscr{C}} \rho(t^{n+1}, x)\,\mathrm{d}x\,, \tag{2.17}$$

where ρ is the solution sampled at t^{n+1} to the Riemann problems at the interfaces of the piecewise constant data at t^n. The density ρ is non-negative $\rho^{n+1} \geq 0$ which implies that the Godunov method is non-negativity preserving.

2.3.2 Boundary conditions

The choice of boundary condition is crucial for accurate steady state solutions in a transient framework. We will discuss the boundary conditions for the domain edges and the icing body in the next two sections.

Computational domain boundary conditions

The free flow variables infinitely far away are denoted by the superscript $\cdot^{\infty}$. Since the homogeneous system can be decomposed into two subsystems, we can discuss the boundary conditions independently for each phase. The air phase is typically in a subsonic state whereas the droplet phase is always supersonic. In subsonic conditions characteristics travel up and down stream and therefore information leaves the domain at the inflow boundary. In order to represent this behaviour numerically, we need to extrapolate values from the domain. One solution of the characteristic equations for the air phase is that entropy is constant along non-linear waves (LeVeque, 2002). Therefore, the entropy is an obvious choice of a variable to specify at the inflow boundary. For the remaining quantities we follow the work by Jameson et al. (1981) and specify momentum at the inflow boundary and pressure at the outflow boundary. The other air phase variables are extrapolated from the domain.

The droplet phase is always supersonic, therefore, all state variables are specified at inflow boundaries and extrapolated from the domain at outflow boundaries. At inflow boundaries, the droplet density is defined by the LWC and the remaining state variables are obtained by assuming velocity and temperature equilibria between the phases.

Semi-reflective boundary condition for collection efficiencies

Similarly to the domain boundaries, we can consider each phase independently at the fluid-solid interface. A no-penetration condition is imposed for the air flow, which is given by

$$\boldsymbol{v}_{\mathrm{a}} \cdot \hat{\boldsymbol{n}} = 0 \,, \tag{2.18}$$

where $\hat{\boldsymbol{n}}$ is the outward pointing unit normal vector to the surface.

In order to represent the impingement of droplets, they must be able to leave the computational domain, which suggests transmissive conditions at the fluid-solid interface. However, transmissive conditions also allow unphysical high particle concentration to enter the domain from the geometry. Therefore, we need to apply a fix to prevent the droplet concentration rising. We achieve that by distinguishing between two cases and applying different conditions. If $\boldsymbol{v}_s \cdot \hat{\boldsymbol{n}} < 0$, characteristics leave the domain and transmissive boundary conditions are applied. In this case, all droplet phase quantities are extrapolated from the computational domain to the ghost cells. On the other hand, if $\boldsymbol{v}_s \cdot \hat{\boldsymbol{n}} \geq 0$, characteristics travel into the domain and we need to define the ghost state to maintain well-posedness. This is done by imposing a vacuum state which prevents the droplet concentration from rising. Mathematically, this is equivalent to reflective boundary conditions. Reflective boundary conditions combined with the condition of characteristics entering the domain give a vacuum state as a solution to the boundary Riemann problem (see (Wutschitz and Nikiforakis, 2016; Sheng and Zhang, 1999) for more details about the Riemann problem solutions). This type of boundary condition was used by da Silveira et al. (2003), Kim et al. (2013) and Wutschitz (2014) to compute the non-dimensional collection efficiency $\tilde{\beta}$ by

$$\tilde{\beta} = -\frac{\sum_s \alpha_s \boldsymbol{v}_s \cdot \hat{\boldsymbol{n}}}{\sum_s \alpha_s^{\infty} ||\boldsymbol{v}^{\infty}||} \,. \tag{2.19}$$

2.3.3 Cut-cell method

The cut-cell approach employed in this work is based on a Cartesian mesh which can be generated efficiently. This approach, however, gives rise to cut-cells that contain both solid and fluid at the boundary of the geometry which need special treatment when updating their values. Klein, Bates, and Nikiforakis (2009) circumvented the problem by introducing a stabilised flux which extends the domain of influence of the small cell to its neighbours. For the sake of brevity, we will refer to a flux which is stabilised using this method as KBN flux. The stabilisation is based on the shape of the cut-cell. In particular, volume and face fractions are required to define the KBN flux and the cell updates. In this work we employ an approach that defines the cut-cell geometry parameters in terms of a signed distance function (SDF). For performance reasons, we approximate the geometry by a polygon. Highly optimised signed distance algorithms exist (Roosing et al., 2018; Mauch, 2003). Details about the polygonisation of the parameterised surface are given in appendix A. Furthermore, implementation details for the cut-cell geometry computation from the SDF are given in Barton et al. (2011) and Gokhale et al. (2018).

Gokhale et al. (2018) extended the KBN approach by taking into account local wave speeds. Their *Localised Proportional Flux Stabilisation* (LPFS) approach relaxes the stabilisation criterion if the local wave speed allows a larger update. Detailed comparisons of the two methods for dry air flows over aerofoils were carried out by Gokhale et al. (2018). They found that the LPFS method performs significantly better near stagnation points. Since capturing the stagnation point flow accurately is essential for ice accretion simulation, we base our implementation on the LPFS method. The stabilised flux $\boldsymbol{F}^{\mathrm{LPFS}}$ is given by an area and wave speed weighted linear combination of the conventional flux and the flux obtained at the domain boundary. Figure 2.1 depicts a typical cut-cell situation, where a regular fluid cell $\mathscr{C}_i$ is situated next to a cut-cell $\mathscr{C}_{i+1}$ which is bordering a boundary ghost cell $\mathscr{C}_{i+2}$. In this case the LPFS flux is given by

$$\boldsymbol{F}^{\mathrm{LPFS}}_{i+\frac{1}{2}} = \left(1-(1-\hat{\lambda}_{i+1})^2\right)\boldsymbol{F}_{i+\frac{1}{2}} + (1-\hat{\lambda}_{i+1})^2\boldsymbol{F}_{i+\frac{3}{2}} \,. \tag{2.20}$$

The ratio of the global to the local stable time step of cell $\mathscr{C}_i$ is denoted by $\hat{\lambda}_i$ and is given by

$$\hat{\lambda}_i = \min\left\{1, \alpha_i \frac{\max_j \max|\lambda_j|}{\max|\lambda_i|}\right\} , \tag{2.21}$$

where $\max|\lambda_i|$ is the maximum wave speed of cell $\mathscr{C}_i$. Consequently, the finite volume update scheme for a cut-cell becomes

$$\boldsymbol{U}^{n+1}_{i+1} = \boldsymbol{U}^{n}_{i+1} - \frac{\Delta t}{\alpha_{i+1}\Delta x}\left[\boldsymbol{F}_{i+\frac{3}{2}} - \boldsymbol{F}^{\mathrm{LPFS}}_{i+\frac{1}{2}}\right] . \tag{2.22}$$

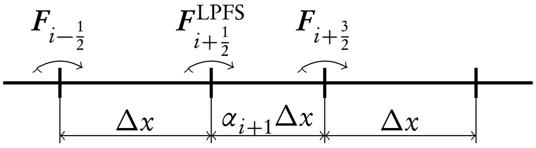

Figure 2.1: Cut-cell geometry

This method is consistent with the update scheme of a regular cell since equation (2.20) recovers the regular flux $\boldsymbol{F}_{i+\frac{1}{2}}$ as $\alpha_{i+1} \to 1$ and $\boldsymbol{F}_{i+\frac{3}{2}}$ as $\alpha_{i+1} \to 0$. The boundary flux $\boldsymbol{F}_{i+\frac{3}{2}}$ is obtained by solving the Riemann problem of the cut-cell $\mathscr{C}_{i+1}$ and the ghost cell $\mathscr{C}_{i+2}$ with the Godunov method. The ghost cell state is obtained by the boundary condition. In multiple dimensions it is important to keep this state constant throughout the global time step and not to apply the boundary condition after a one-dimensional sweep. Otherwise unphysical directionalities may be introduced or conservation may be lost.

In the remainder of this section we focus on the implications of using the LPFS stabilisation to solve the dusty gas model. Details about the general LPFS implementation are omitted and can be found in Gokhale et al. (2018).

Non-negativity preservation in the presence of cut-cells

The boundary flux $\boldsymbol{F}_{i+\frac{3}{2}}$ is obtained by solving a boundary Riemann problem and for most cut-cell applications the boundary condition is a reflective wall. In such a case, the advective flux vanishes and the analysis from section 2.3.1 holds true for the stabilised update from equation (2.22) rendering the cut-cell update non-negativity preserving. However, the non-negativity preservation argument from section 2.3.1 does not generalise to a semi-reflective boundary condition on an irregular grid. The following example demonstrates this problem.

Consider a setup as illustrated in figure 2.1 where a regular cell is next to a cut-cell which is to the left of the boundary. For the sake of brevity, we only consider the droplet phase. The ghost cell state is obtained by using transmissive boundary conditions which extrapolate all state variables from the computational domain to the ghost cell. Moreover, we assume the initial conditions are chosen such that they are represented by figure 2.2 i.e. $v_{i-1} < v_i < 0 < v_{i+1}$.

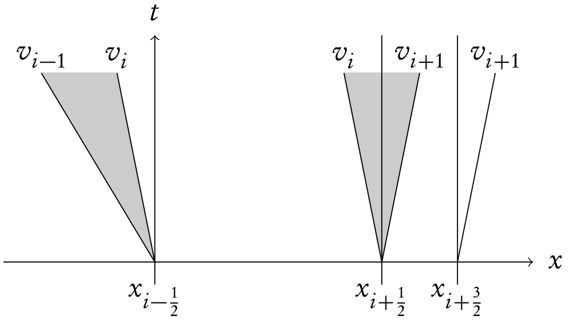

Figure 2.2: A wave solution for the Riemann problem of the pressureless Euler equations. A cut-cell is bordering a regular cell and the ghost state is extrapolated using a transmissive boundary condition.

In this case, the update formula of density for a cut-cell gives

$$\begin{aligned}
\rho_{i+1}^{n+1} &= \rho_{i+1} - \frac{\Delta t}{\alpha_{i+1}\Delta x}\left[\rho_{i+1}v_{i+1} - (1-\hat{\lambda}_{i+1})^2\rho_{i+1}v_{i+1}\right] = \\
&= \rho_{i+1} - \frac{\Delta t}{\alpha_{i+1}\Delta x}\left(1-(1-\hat{\lambda}_{i+1})^2\right)\rho_{i+1}v_{i+1} = \\
&= \rho_{i+1} - \frac{\Delta t}{\alpha_{i+1}\Delta x}\left(2-\hat{\lambda}_{i+1}\right)\alpha_{i+1}\frac{\max_j|v_j|}{|v_{i+1}|}\rho_{i+1}v_{i+1} = \\
&= \left(1-C_{\mathrm{CFL}}(2-\hat{\lambda}_{i+1})\right)\rho_{i+1}\,.
\end{aligned} \tag{2.23}$$

Given a CFL condition of $C_{\mathrm{CFL}} \leq 1/2$, the density is guaranteed to remain non-negative.

However, the situation for the neighbouring cell is different. The update formula for density for the cell next to the cut-cell becomes

$$\begin{aligned}
\rho_i^{n+1} &= \rho_i - \frac{\Delta t}{\Delta x}\left[(1-\hat{\lambda}_{i+1})^2\rho_{i+1}v_{i+1} - \rho_i v_i\right] = \\
&= \left(1-\frac{\Delta t}{\Delta x}|v_{i+1}|\right)\rho_i - (1-\hat{\lambda}_{i+1})^2|v_{i+1}|\frac{\Delta t}{\Delta x}\rho_{i+1} \leq \\
&\leq \rho_i - (1-\hat{\lambda}_{i+1})^2\frac{\Delta t}{\Delta x}|v_{i+1}|\rho_{i+1}\,.
\end{aligned} \tag{2.24}$$

Compared to the update of a regular cell we have gained a term which arises from the *extension of influence of the cut-cell.* This term depends only on quantities of cell $\mathcal{C}_{i+1}$. We can choose them freely and they will not affect the way the update for cell $\mathcal{C}_i$ is computed as long as $v_{i+1} > 0$. The ratio $\hat{\lambda}_{i+1}$ depends only on v_{i+1}, hence, we can choose ρ_{i+1} sufficiently large such that the flux contribution from the cut-cell $\mathscr{C}_{i+1}$ is large enough to produce a negative density in the updated state.

This problem can be rectified by exploiting the structure of the wave solution of the Riemann problem for the pressureless Euler equations. The sampled flux at the interface $x_{i+\frac{3}{2}}$ is either $\boldsymbol{u}_{i+1}$ for outgoing droplets or $\boldsymbol{u}_{\mathrm{vac}}$ for incoming. We consider first the case of outgoing waves. Since the pressureless flow is always supersonic no information travels upstream and therefore no stabilisation is required. Hence, we can set $\hat{\lambda} = 1$ and recover non-negativity preservation. By definition of the semi-reflective boundary condition, incoming characteristics are always vacuum states. Plugging a vacuum state into equation (2.24), we can see that the last term vanishes and non-negativity preservation is maintained.

In summary, we can recover non-negativity preservation of the stabilised pressureless flux for a semi-reflective boundary condition by altering the stabilisation parameter $\hat{\lambda}$ for outgoing waves without sacrificing stability. This method shows greatly increased robustness over the approach in Wutschitz (2014).

2.3.4 Source terms

The source and homogeneous parts of the system (2.1) are solved subsequently using an operator splitting approach proposed by Strang (1968). Given a time step Δt, the splitting method initially advances the source problem by half the time step $\Delta t/2$, followed by the homogeneous problem by a full time step Δt, and finally the source problem by another half time step $\Delta t/2$.

The source problem takes the form of an ordinary differential equation (ODE) given by

$$\frac{\mathrm{d}\boldsymbol{u}}{\mathrm{d}t} = \boldsymbol{S}^{\mathrm{Q}} + \boldsymbol{S}^{\mathrm{D}}, \tag{2.25}$$

and consists of two non-linear terms $\boldsymbol{S}^{\mathrm{Q}}$, which represents the heat coupling, and $\boldsymbol{S}^{\mathrm{D}}$ which denotes the drag coupling term. The non-linear terms are given by

$$\boldsymbol{S}^{\mathrm{D}} = \begin{pmatrix} 0 \\ \sum_s D_s(\Delta \boldsymbol{v}_s) \\ \sum_s D_s(\Delta \boldsymbol{v}_s) \cdot \boldsymbol{v}_s \\ 0 \\ D_s(-\Delta \boldsymbol{v}_s) \\ D_s(-\Delta \boldsymbol{v}_s) \cdot \boldsymbol{v}_s \end{pmatrix}, \qquad \boldsymbol{S}^{\mathrm{Q}} = \begin{pmatrix} 0 \\ 0 \\ \sum_s Q_s(\Delta T_s) \\ 0 \\ 0 \\ Q_s(-\Delta T_s) \end{pmatrix}. \tag{2.26}$$

The source problem is advanced by first solving the drag coupling and subsequently the heat coupling ODE. This sequence can be thought of as another application of an operator splitting approach.

Since the governing equations are a system of ODEs the stability restriction of an explicit numerical solver does not depend on the cell size. This can have a problematic effect when solving the equations on a grid with adaptive mesh refinement (AMR) since different refinement levels are advanced at different time steps. Indeed, we have found that larger time steps arising from coarse base grids violate the stability restrictions of most explicit ODE solvers. However, analytic solutions of the ODEs are available thereby completely removing the need for a numerical solver.

Drag coupling

The drag coupling ODE consists of a momentum source term and an energy update. However, it is sufficient to find a solution for the momentum component since $\partial_t e_s = 0$ which means that the energy update only reflects the change in kinetic energy. Under the assumption that the Reynolds number remains constant throughout the time step an analytic solution for the momentum equation was derived by Pelanti and LeVeque (2006), which reads:

$$(\alpha_s \rho_s \boldsymbol{v}_s)(\Delta t) = (\alpha_s \rho_s \boldsymbol{v}_s)^0 - \frac{\Delta \boldsymbol{v}_s^0}{r_s^0} \left(\frac{1}{A_s^0 r_s^0 ||\Delta \boldsymbol{v}_s^0|| \Delta t + 1} - 1 \right) , \tag{2.27}$$

where the superscript $\cdot^0$ labels initial values and the following substitutions were made for the harmonic sum of the densities and the coefficients of the drag force (2.7)

$$r_s = \frac{1}{\alpha_s \rho_s} + \frac{1}{\alpha_\mathrm{a} \rho_\mathrm{a}} , \qquad A_s = \frac{3\, C_\mathrm{D}\, \alpha_s\, \rho_s\, \alpha_\mathrm{a}}{4\, d_s} . \tag{2.28}$$

Heat coupling

Similarly, Pelanti and LeVeque (2006) derived an analytical solution for the heat coupling ODE which is given by

$$(\alpha_s E_s)(\Delta t) = (\alpha_s E_s)^0 - \frac{\Delta T^0}{q^0} \left(\exp(-Q^0 q^0 \Delta t) - 1 \right) , \tag{2.29}$$

where

$$q = \frac{1}{c_{\mathrm{v}s} \alpha_s \rho_s} + \frac{1}{c_{\mathrm{va}} \alpha_\mathrm{a} \rho_\mathrm{a}} , \qquad Q_s = \frac{6\, \mathrm{Nu}\, k_\mathrm{a}\, \alpha_s}{d_s} . \tag{2.30}$$

2.3.5 Adaptive mesh refinement

A hierarchical adaptive mesh refinement (H-AMR) methodology, where patches of higher resolution exist above coarser levels, is used in this work. Restriction operators then project the high-resolution solution onto the lower levels. This allows capture of the solution in high accuracy in regions of interest and increases efficiency in the remaining part of the domain. This approach was originally presented by Berger and Colella (1989) and Bell et al. (1994).

2.4 Validation

In this section, we present test cases to validate our implementation of the cut-cell algorithm and the air and water droplet Riemann solver. Firstly, the solver is validated by considering a one-dimensional shock tube test. The results obtained are compared against data published by Saito (2002) and Pelanti and LeVeque (2006) who use these equations to model volcanic eruptions. Following this, the flow of air and water droplets over a NACA 0012 aerofoil is considered. The numerically obtained collection efficiency is compared to numerical results by Al-Khalil et al. (1997) who used the LEWICE software suite and by Morency et al. (1999) who employed the CANICE package. More comprehensive validation studies of our implementation of the reduced Eulerian droplet flow model (without temperature tracking) and the cut-cell method for external aerodynamic problems were presented by Wutschitz and Nikiforakis (2016).

2.4.1 Validation of air and droplet coupling

The implementation of the analytic source term solvers is validated using a numerical shock tube experiment. The problem was initially described by Saito (2002) and results for this test were also published by Pelanti and LeVeque (2006). The initial condition consists of a Riemann problem. A high pressure and high density ideal gas section is separated from a particle laden gas at a resting reference state with a reference velocity v_{ref} of $\sqrt{p_{\mathrm{ref}}/\rho_{\mathrm{ref}}}$. The particles are n mechanical and thermal equilibrium with the carrier phase. A physically negligible small droplet concentration is introduced in the driver section for numerical robustness reasons. The initial conditions with respect to a reference state are given in table 2.1.

We chose the carrier phase to be air with the reference state being at atmospheric conditions. The particles represent crown glass with a density $\rho_{\mathrm{d}} = 2500\,\mathrm{kg\,m^{-3}}$ and a droplet diameter of $d = 10\,\mu\mathrm{m}$. All of the results are presented in a normalised form relative to the reference state. A characteristic length λ is given by $\frac{4}{3}\frac{\rho_{\mathrm{d}}}{\rho_{\mathrm{ref}}}d$ and a characteristic time τ by $\frac{\lambda}{u_{\mathrm{ref}}}$. Also, the non-dimensional

		driver section	driven section
macroscopic pressure	$\alpha_\mathrm{a} p / p_\mathrm{ref}$	10	1
macroscopic air density	$\alpha_\mathrm{a} \rho_\mathrm{a} / \rho_\mathrm{ref}$	10	1
macroscopic particle density	$\alpha_\mathrm{d} \rho_\mathrm{d} / \rho_\mathrm{ref}$	1/10000	1
air velocity	$v_\mathrm{a} / v_\mathrm{ref}$	0	0
particle velocity	$v_\mathrm{d} / v_\mathrm{ref}$	0	0
air temperature	$T_\mathrm{a} / T_\mathrm{ref}$	1	1
particle temperature	$T_\mathrm{d} / T_\mathrm{ref}$	1	1

Table 2.1: Initial conditions for Saito's shock tube experiment for the dusty gas model

heat capacities of the particles and the gas are assumed to be equal and are given by $\frac{1}{\gamma - 1}$. Saito (2002) employs a temperature dependent viscosity relation and heat transfer coefficient. In order to compare our implementation to his data we use the same expressions for this test case. The results presented in the rest of the chapter were obtained using a constant viscosity and heat transfer coefficient. The physical domain $[0, 100\lambda]$ is discretised using 1000 computational cells. The membrane is located at 40λ and separates the driver section on the left hand side from the driven section on the right hand side.

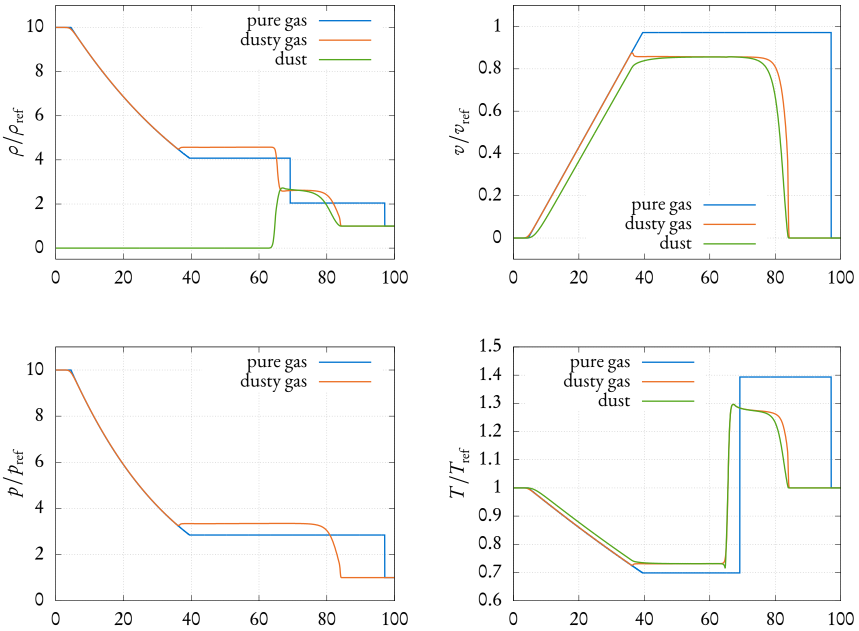

Figure 2.3: Saito's test for the full particle and gas model at $t = 30\tau$

The results of the numerical experiment are illustrated in figure 2.3. The graphs compare density, velocity, pressure and temperature of a pure ideal gas with a fluid containing particles. In the absence of dust particles, the Riemann problem for the pure gas can be solved exactly and the solution is plotted. The dusty gas solution was obtained using the MUSCL Hancock flux method with an exact Riemann solver. The results are taken after the initial condition has been advanced by 30τ.

The driver section transfers heat and momentum to the particles in the driven section. Consequently, the maximum velocity and temperatures are smaller compared to the pure gas case. However, the pressure is higher since the particles hinder the relaxation process. Pelanti and LeVeque (2006) observed slight oscillations in the temperature quantity which they attributed to the second order reconstruction of the flux method. We find similar oscillations around the contact wave. Those oscillations are not present in conserved quantities. Overall, our results agree very well with the data published by Saito (2002) and Pelanti and LeVeque (2006). Therefore, we consider the implementation of the analytic solver of the source problem to be correct.

2.4.2 Validation of collection efficiency boundary condition

One of the reasons for using the LPFS cut-cell method by Gokhale et al. (2018) over the KBN method (Klein et al., 2009) is the improved performance near stagnation points. Detailed validation of the method was carried out by Gokhale et al. (2018). The numerical results were compared to experiments by Amick (1950) for dry air flows over aerofoils. We consider this validation comprehensive for our applications and do not repeat dry air flow validation.

However, the numerical performance of the LPFS method in the presence of water droplets is still to be assessed. We are mainly interested in the modification to the flux stabilisation for the droplet phase for computing collection efficiencies. To this end, we compare the results of our numerical experiments to data from literature.

Morency et al. (1999) has studied the collection efficiency of a NACA 0012 aerofoil in typical icing conditions. They use the CANICE software which employs a Lagrangian approach to solve the droplet equations. A flow of Mach number 0.14 around an aerofoil of chord length $0.9144\,\mathrm{m}$ was considered. The free stream temperature was set to $265.55\,\mathrm{K}$ and the free stream pressure to $94\,540\,\mathrm{Pa}$. Morency et al. (1999) models the droplet distribution with a Log-normal distribution. The underlying Gaussian has parameters $\mu = 0$ and $\sigma = 0.119$ about MVD $= 20\,\mu\mathrm{m}$. The discretisation of the model is given in table 2.2. The water droplet concentration of the free stream is $0.78\,\mathrm{g\,m^{-3}}$

		d_s / MVD	
Bin s	Weight	Log-normal	Langmuir D
1	0.05	0.792	0.31
2	0.10	0.859	0.52
3	0.20	0.923	0.71
4	0.30	1.000	1.00
5	0.20	1.083	1.37
6	0.10	1.164	1.74
7	0.05	1.262	2.22

Table 2.2: Discretisation of the model for the droplet diameter distribution. Two commonly used models are the Langmuir D distribution which is based on a Γ-distribution (Langmuir and Suits, 1961) and a Log-normal distribution.

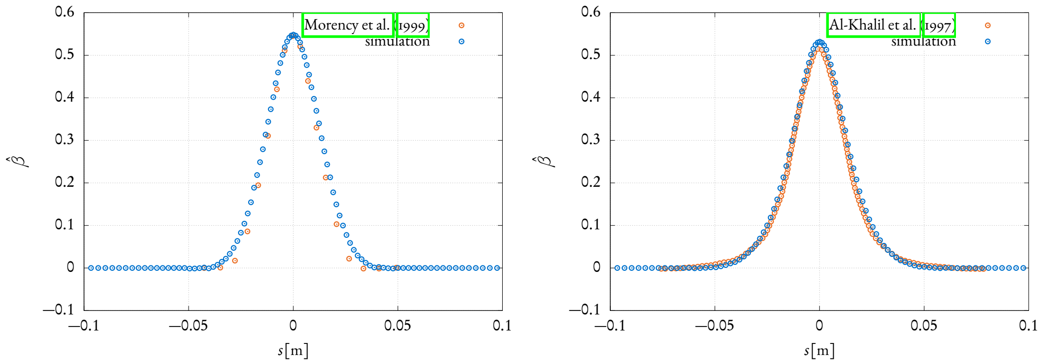

(a) Log-normal distribution

(b) Langmuir-D distribution

Figure 2.4: Non-dimensionalised collection efficiency $\hat{\beta}$ for a NACA 0012 aerofoil over the surface distance from the stagnation point. Two different models for the droplet diameter are used and both agree very well with results from literature.

The results are illustrated in figure 2.4a. The agreement around the peak collection is excellent. However, the extent of the droplet impingement is slightly larger for our results. Nevertheless, given that the results were obtained using two significantly different methodologies we consider the agreement to be satisfactorily.

The second test uses a Langmuir D distribution (Langmuir and Suits, 1961) of a median value diameter (MVD) of $20\,\mu\mathrm{m}$ to model the droplet diameters. The discretisation of distribution is given in table 2.2 The collection efficiency for this case has been numerically studied by Al-Khalil et al. (1997) using the LEWICE software suite which employs a Lagrangian method to calculate β. The results of our numerical experiments of the NACA 0012 aerofoil are illustrated in figure 2.4b. Contrary to the previous test case, the two simulations match for the extent of water droplet impingement, whereas, the peak collection is slightly higher in our simulation. Overall, we still consider the solution to show good agreement.

Both plots also illustrate the correct physical behaviour of the semi-reflective boundary condition. If characteristics enter the domain from the icing body (i.e. $v_s \cdot \hat{n} > 0$), the reflective condition creates a vacuum state which can be seen as a vanishing collection efficiency in those regions.

In summary, we conclude that the modification for the flux stabilisation of the droplet phase is able to predict accurate collection efficiencies of two-dimensional aerofoil geometries. None of the simulations showed non-physical states such as negative densities and handled the test cases robustly.

Three-dimensional droplet flow over a sphere

The third test case demonstrates the method's capability to model three-dimensional flow. As mentioned earlier, one of the advantages of describing the droplet phase in the Eulerian frame is the easy extension to three-dimensional problems. The air flow is modelled by the inviscid Euler equations. The initial conditions are irrotational and due to Kelvin's circulation theorem rotational flow as found in boundary layers cannot be modelled.

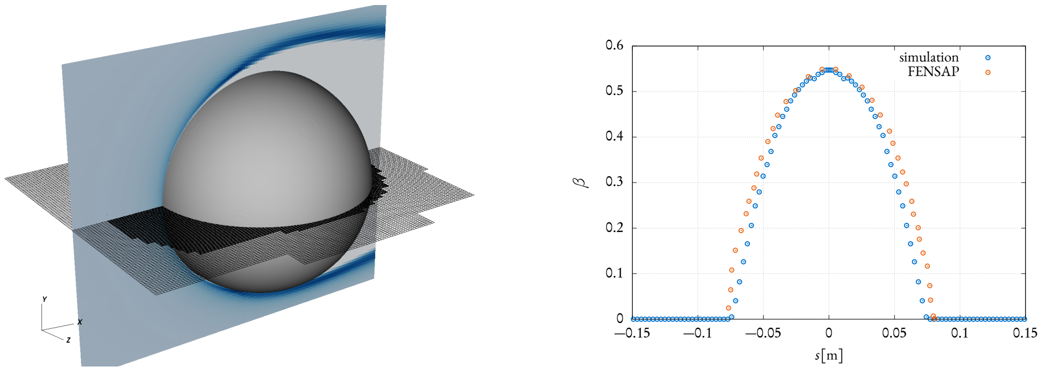

(a) Illustration of the simulation setup for the air and droplet flow around a sphere. The slice in the xy-plane shows the water concentration and the xz-plane the mesh. Only the two finest AMR levels are shown. The refinement criteria is based on the droplet concentration.

(b) Non-dimensionalised collection efficiency $\hat{\beta}$ for a sphere. The horizontal axis s denotes the surface distance from the stagnation point in a slice perpendicular to $(0, -1, 1)$ and intercepting the origin of the sphere.

Figure 2.5: Flow of air and droplets around a sphere.

This setup replicates the validation test by Bourgault et al. (2000b). A sphere of diameter $0.1504\,\mathrm{m}$ in a flow of Mach number 0.22 and a Reynolds number of $785,000$ is considered. A droplet phase of a single diameter of $18.6\,\mu\mathrm{m}$ is introduced. AMR is used to refine regions of higher droplet concentration and around the geometry.

The results are shown in figure 2.5. The data obtained by the cut-cell implementation agrees very well with published collection efficiency results. Both the peak catch as well as the extent of droplet impingement are captured accurately.

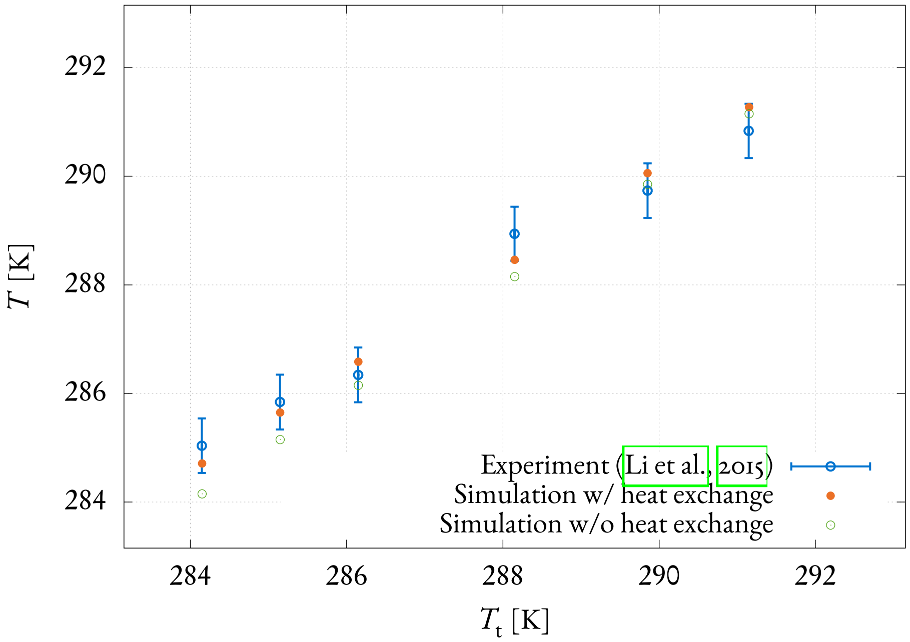

Figure 2.6: This illustration compares water droplet temperatures of the conventional pressureless model, our new augmented model and experimental results. Water droplets are released and their temperature is measured after they travelled for 100 cm. The horizontal axis denotes the temperature of the droplets when they are released and the vertical axis the temperature after they interacted with the ambient air. If the water droplet temperature is close to the ambient air temperature both models give accurate results, however, as the water droplet and air temperature diverge heat exchange needs to be taken into account. At larger temperature differences, only the methodology that models energy transfer agrees with experimental results.

2.4.3 Validation of heat exchange modelling

The heat exchange terms are validated by comparing the numerical results to experiments done by Li et al. (2015). The experimental setup is as follows. Water droplets of a diameter of 450 µm are generated using a piezoelectric device. The water is sourced from a tank which is kept at a lower temperature T_t than the ambient air. The water droplets are released with an initial velocity of $2.01\,\mathrm{m\,s^{-1}}$. The water droplet temperature T is measured at a distance of 100 cm from the source. The air temperature T_a is kept constant at 293.15 K.

Li et al. carried out the experiment at various water tank temperatures T_t between 284.15 K and 291.15 K and the results are shown in as blue error bars in figure 2.6. We have reconstructed this setup by considering a one-dimensional simulation. The domain size is 200 cm divided into 201 cells to make the coordinate 100 cm a cell centre. The standard physical parameters were used which are denoted in table 2.3.

Quantity	Symbol	Value
Dynamic air viscosity	μ_a	$1.725 \times 10^{-5}\,\mathrm{Pa}$
Thermal air conductivity	k_a	$2.428 \times 10^{-2}\,\mathrm{W\,m^{-1}\,K}$
Droplet heat capacity	c_d	$4192\,\mathrm{J\,kg^{-1}}$

Table 2.3: Values for physical constants for the air and water droplet simulations.

At the left hand side, a subsonic-air-supersonic-droplet boundary condition is imposed which consists of atmospheric conditions with a temperature of T_a and vanishing velocity for the air phase. The droplet phase velocity is set to $2.01\,\mathrm{m\,s^{-1}}$ and the temperature to T_t. A high-resolution MUSCL Hancock flux method with a van Leer type limiter and an exact Riemann solver was used. The simulation was run until a steady state was reached. The result of this simulation is illustrated in figure 2.6 as orange data points.

In general, we observe excellent agreement between the experimental data and results obtained using our methodology which takes heat transfer into account. We have also plotted the conventional model (without heat exchange) as green symbols. As the droplets are near temperature equilibrium with the air phase both the model with and without heat exchange gives accurate answers, however, as the temperature difference increases only the our model captures temperatures accurately. We therefore conclude that the augmented pressureless model with heat exchange is able to give accurate results over a wider range of situations.

2.5 Case studies

Following the successful validation of the numerical method and verification of the mathematical model we turn to the study of the temperature of the droplet phase and collection efficiencies. In this section, we present three case studies which demonstrate the capability of recovering droplet temperatures and the robustness of the cut-cell mesh generation.

2.5.1 Droplet temperature dependence on free-stream Mach number and angle of attack

As mentioned earlier we are not aware of an icing simulation that describes the droplet phase with a model other than the pressureless equations which implies that the system of droplets remains at its initial temperature. This, however, is only true in the case of single phase particulate flow where the only sources of temperature changes are compressibility effects which are particularly prominent at the stagnation point. In icing conditions two aspects of the flow affect the scale of the heat exchange. Firstly, the maximum temperature of the carrier phase and secondly the extent of the region of high air temperature. The former contribution is expressed in terms of the Mach number of the flow. In general, the temperature of a resting ideal gas, which has gotten to that state by an adiabatic change, is called the *total temperature* T_{tot}. At a stagnation point, all of the kinetic energy of the gas has transformed into internal energy and we observe a higher gas temperature. The explicit function for the total air temperature (Anderson, 2011) is given by

$$T_{\text{tot}} = T_{\infty}\left(1 + \frac{\gamma - 1}{2}\,\mathrm{Ma}^2\right). \tag{2.31}$$

Secondly, the extent of high air temperature depends on the shape of the solid geometry. A stagnation point of low surface curvature causes a greater deflection of streamlines and consequently a greater extent of decelerated flow. This gives the droplet phase more time to interact with the air phase and results in higher droplet temperatures. In the context of ice accretion prediction this is especially prevalent during take offs and landings. In these stages of the flight high angle of attack flows are common where the stagnation point moves from the leading edge of the aerofoil towards a flatter part of the wing. Hence, we expect the maximum droplet temperature to increase with the angle of attack.

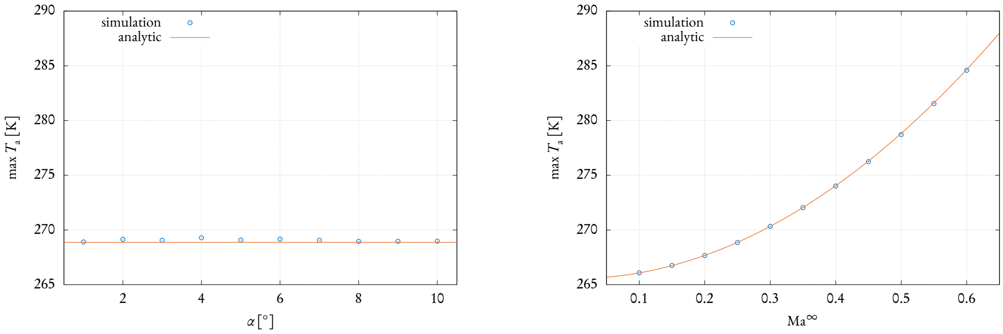

(a) Stagnation point air temperatures for varying angles of attack and Mach number of 0.25

(b) Stagnation point air temperatures for varying Mach number at zero angle of attack

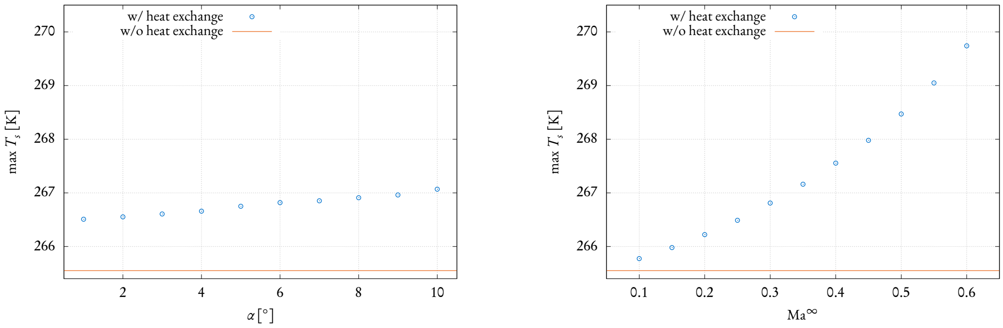

(c) Droplet temperatures at stagnation points for varying angles of attack and Mach number of 0.25

(d) Droplet temperatures at stagnation points for varying Mach number at zero angle of attack

Figure 2.7: Surface temperatures of air and impinging water droplets at the stagnation point. The top two subfigures compare the maximum air temperature observed in the simulation to the analytical prediction. Whereas the illustrations at the bottom depict the temperature of the water droplets. The results for the dispersed phase demonstrate the effects of the heat exchange term. A temperature increase is observed if heat exchange terms are considered. On the other hand, the conventional pressureless or isothermal model produce constant droplet temperatures.

In order to demonstrate this behaviour, we study the air and droplet flow with a free stream pressure of 94 540 Pa and a free stream temperature of 265.55 K around a NACA 0012 aerofoil. Figure 2.7 depicts the outcome of the simulations. Subfigures 2.7a and 2.7c show the results for the air and droplet temperatures and the stagnation point for varying angle of attacks and a constant Mach number of 0.25. The subfigures on the right hand side (2.7b and 2.7d) present the outcome of the simulation for varying Mach numbers at zero angle of attack.

The air phase stagnation point temperatures (figure 2.7a and b) are known analytically (see equation (2.31)). The theoretical predictions are plotted alongside the numerical results of the stagnation point temperature and excellent agreement is observed.

Contrary to the air phase we expect the maximum droplet temperature to increase with both the angle of attack and the Mach number of the flow. Indeed, as shown in figure 2.7c and d an increase in droplet temperature is observed in both cases. The results are compared to commonly used models for water droplets without heat exchange. At an angle of attack of 4° a for icing application relevant temperature increase of more than 1 K is observed. Similarly, the droplet temperature also depends on the Mach number. Figure 2.7d illustrates this relation for a constant angle of attack of 0°

2.5.2 GA-W-1 aerofoil with Fowler flap system

In order to demonstrate the effect of heat exchange between droplets and air in a more applied scenario we consider the flow around a multi-element aerofoil. The free stream Mach number of the flow is 0.3, the free stream temperature is 270 K and the free stream pressure is 94 540 Pa. The aerofoil is placed at an angle of attack 10°, the flap is extended by an angle of 30°. A detailed description of the geometries is given by Wentz and Seetharam (1974). We introduce a water droplet phase of 16 μm diameter with a LWC of $1\,\mathrm{g\,m^{-3}}$.

(a) Liquid water content

(b) Air temperature

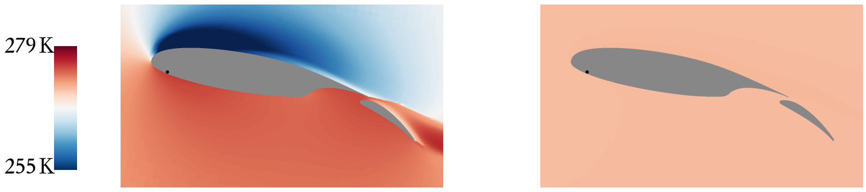

(c) Droplet temperature with heat coupling as proposed in this work

(d) Droplet temperature without heat coupling as used by previous models

Figure 2.8: Illustration of temperature coupling effects of water droplet flow around a GA-W-1 aerofoil with extended Fowler flap system. The black circle indicates the position of the stagnation point.

The results of this simulation are presented in figure 2.8. Subfigure (a) illustrates the liquid water content around the multi-element aerofoil. It can be seen how the geometry shields the region downstream from the water droplets. Subfigure (b) shows the air temperature field. A maximum temperature of 274.9 K is observed at the stagnation points matching theoretical predictions of 274.8 K using equation (2.31). Subfigures (c) and (d) compare the effect of the temperature tracking. It should be noted that even though mathematically a temperature can be assigned to regions of almost vanishing droplet content such as downstream of the geometry the value does not carry physical meaning. On the left hand side, the results with activated heat exchange terms are shown. A temperature increase of 4 K is found at the stagnation point of the main element of the aerofoil. On the right hand side, the results using the conventional system which omits heat exchange term are shown.

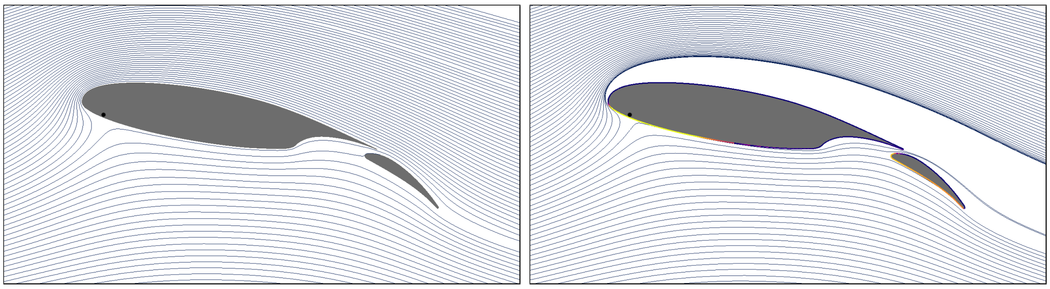
(a) Air streamlines.

(b) Droplet streamlines. Additionally, the LWC is illustrated as pseudocolour boundary of the aerofoil.

Figure 2.9: Illustration of streamlines of air and droplet phases around a GA-W-1 aerofoil with extended Fowler flap system. The black circle indicates the position of the stagnation point.

The streamlines of both phases are illustrated in figure 2.9. Subfigure (a) shows the streamlines of the air flow. Due to the high angle of attack, the stagnation point, which is indicated by the black circle, has moved from the leading edge to the underside of the aerofoil. This causes a high curvature of the streamlines around the leading edge. Subfigure (b) illustrates the trajectories of the water droplets (or streamlines). The inertia of the droplets prevents them from following the air streamlines closely in regions of high curvature. This is particularly visible around the leading edge where a significant area of vanishing droplet concentration is formed.

2.5.3 DrivAer model

Lastly, we demonstrate the capability of this approach of dealing with complex geometries. This approach was developed with the application of ice accretion in mind which requires robust and autonomous mesh generation. However, this model is transferable to other fields. An example is presented in figure 2.10 from the automotive industry. The car model was designed by the Technical

University Munich (2018) with the motivation of providing a more realistic example to study automotive flows and is referred to as the *DrivAer* model. It was designed to replace more simplistic automotive bodies such as the Ahmed body and the SAE model. In our case, it doubles as a complex real world example of an aerodynamic body which poses challenges to the mesh generation method. The relevant geometrical cut-cell parameters are extracted from a STL file of the car. The high level of detail exhibited by the door handles, wing mirrors and rims pose a challenge to conventional mesh generation algorithms. Figure 2.10 shows the collection efficiency of the DrivAer model. To the best of our knowledge no experimental or computational results of collection efficiencies for the DrivAer model are available in literature. Therefore, we want to stress that this test case primarily demonstrates the meshing capability and not to compute a physically accurate solution. However, the results obtained look qualitatively plausible with high collections around exposed surfaces such as wing mirrors, bumpers and wind shields.

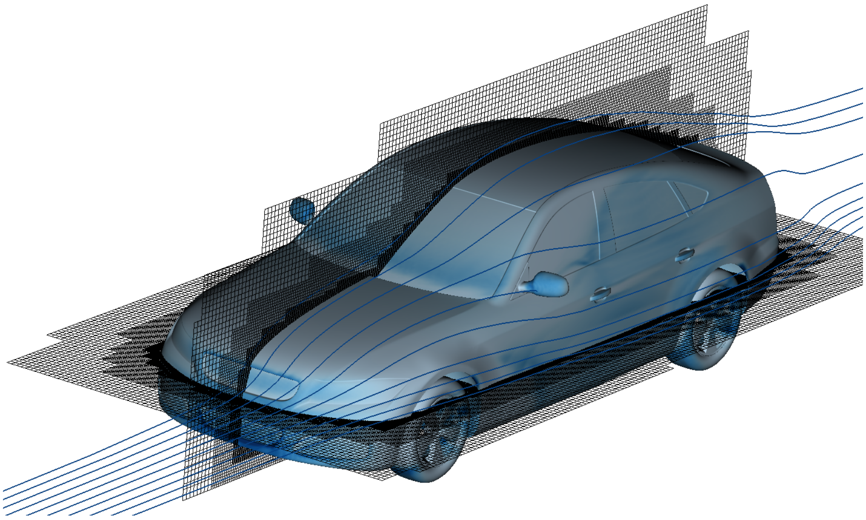

Figure 2.10: DrivAer model

2.6 Conclusion

We have presented two novel improvements for the simulation of water droplet flow in the context in-flight ice accretion.

Firstly, we have extended the mathematical model of the two-phase flow to facilitate for heat-exchange between the droplet and the carrier phase. The model was validated against experimental results and found to be accurate over a broader range of flow conditions compared to conventional formulations. Subsequently, the new set of equations was applied to test cases relevant for atmospheric icing. The results showed a significant droplet temperature difference of up to $2\,\mathrm{K}$ when comparing the new and conventional models.

Secondly, we have implemented the solver in a Cartesian cut-cell framework based on the LPFS method. We have devised a boundary treatment that guarantees non-negative droplet phase states while maintaining stability of the air phase. The approach is validated against experiment and other icing codes. The results show comparable accuracy while allowing for the study of more complex geometries.

Chapter 3

Surface models

In this chapter we, introduce the mathematical models and numerical techniques that are used to link the air and water droplet flow around the icing body with the water film dynamics and phase transition model. Two aspects are important when linking the two simulations, firstly, how to extract the flow data from the air and droplet solver, and, secondly, how to convert the data to an appropriate format for the thin film model.

The process of extracting surface states from a Cartesian cut-cell mesh requires is not as trivial as for a boundary following mesh. Associating the finite volume cut-cell state with a point on the surface introduces an implicit dependency on the projection of the gradient onto the surface normal. We rectify this issue by using a linear least squares gradient reconstruction in order to compensate for the dependency.

The inviscid description of the air flow lacks a physical model for quantities which are governed by the flow within the boundary layer. These include surface friction and heat transfer which are important for the thin film dynamics We discuss the modelling of these variables by means of an integral boundary layer approach.

Finally, the mathematical models and numerical techniques are validated by examining surface data of a flow over a NACA 0012 aerofoil in icing conditions. The test is based on a NATO/RTO *Ice Accretion Simulation Evaluation Test* core case described by Kind (2001).

3.1 Extraction of external flow states

In order to compute the boundary layer, the external flow states need to be extracted at the surface of the rigid body. The aim is to obtain data in the form of pairs (s_i, ϕ_i) where s_i denotes the surface coordinate and ϕ_i the flow state at this coordinate. Without loss of generality, we assume that ϕ is scalar since all of the following operations generalise to a vector quantity by applying them component wise. In the case of a conventional boundary following mesh, the pairs are easily found by using the cell centre states in the first layer of the computational mesh as shown in figure 3.1.

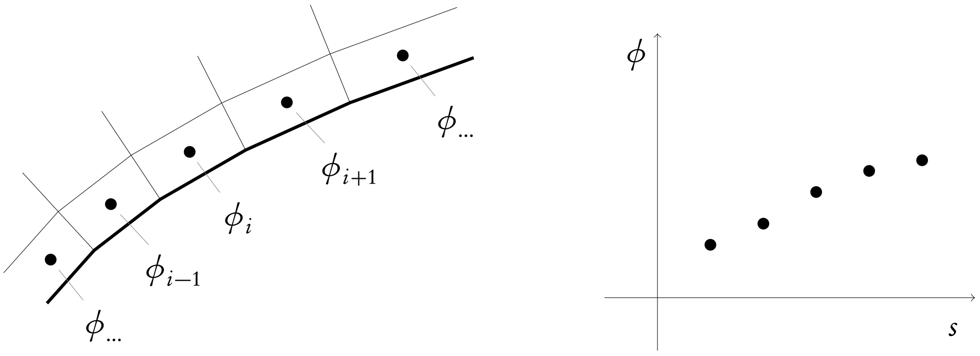

(a) $t = 0$ (b) $t = 0$

Figure 3.1: Illustration of surface data extraction for boundary following computational meshes. Using the flow states ϕ in the first layer of cells gives physically smooth data in the surface coordinate s.

In the case of a Cartesian cut-cell mesh, however, this is no longer possible. Performing the naïve extraction leads to a non-physically high variation in the data as illustrated in figure 3.2. This is due to the varying distance between the surface and the extraction point. If the gradient of the solution has a significant component normal to the surface then the extracted data will depend to first order on the probing distance and potentially cause spurious oscillations. In order to avoid the dependency

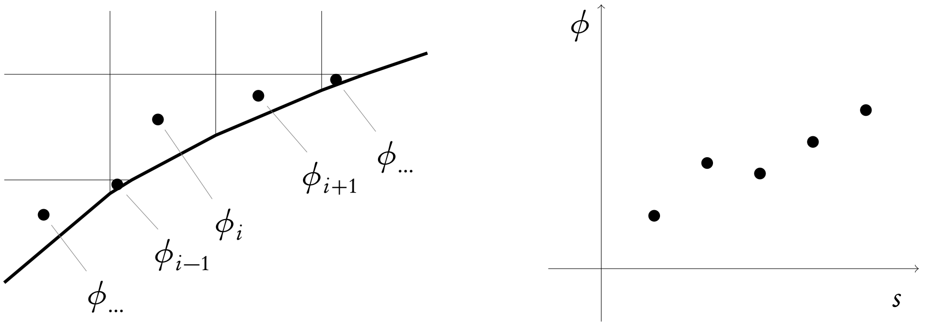

(a) $t = 0$ (b) $t = 0$

Figure 3.2: Illustration of a naïve surface data extraction for cut-cell meshes. Sampling the cell states of the cut-cell implicitly extracts data at varying distances to the surface. A significant component of the gradient perpendicular to the surface can cause spurious oscillations in the extracted data.

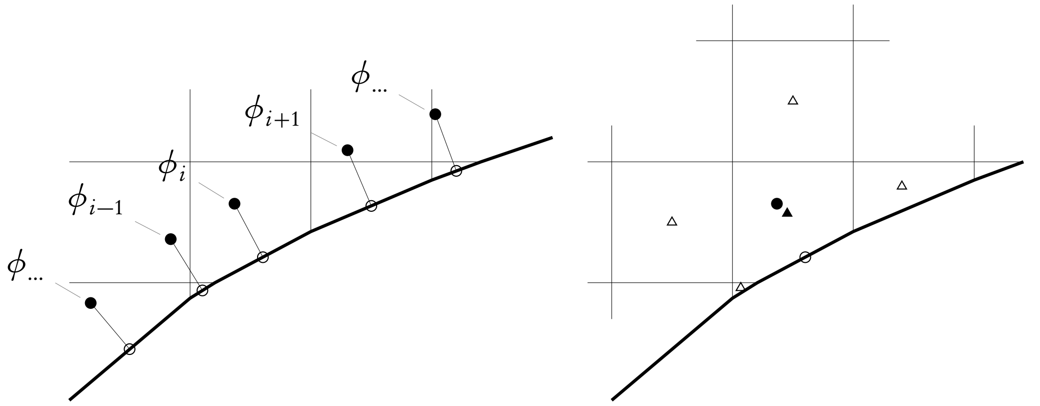

(a) Illustration of determining the extraction points. The interface centroids ○ are extended into the normal direction by a constant distance to give the extraction point ●.

(b) Illustration of the computation of the interpolation of the flow states associated with a surface point. The symbol ▲ denotes the cell centroid of the central cell and △ the cell centroid of the neighbouring cells.

Figure 3.3: Illustration of surface data extraction for a Cartesian cut-cell mesh using a constant distance between extraction position and rigid body surface. This approach is analogous to boundary following grids.

on the distance between the sampling point and the rigid body the surface data has to be extracted using a fixed spacing. The correct sampling points are illustrated in figure 3.3. The extraction distance is chosen to be $\frac{1}{2}\sqrt{\boldsymbol{\Delta x}\cdot\boldsymbol{n}}$, where $\boldsymbol{\Delta x}$ is the cell size of a regular cell. Consequently, the extraction point $\boldsymbol{x}^{\bullet}$ for a cell with outward pointing normal $\boldsymbol{n}$ and interface centroid $\boldsymbol{x}^{\circ}$ is given by

$$\boldsymbol{x}^{\bullet} = \boldsymbol{x}^{\circ} + \boldsymbol{n}\frac{1}{2}\sqrt{\boldsymbol{\Delta x}\cdot\boldsymbol{n}}\,. \tag{3.1}$$

In general, the extraction point $\boldsymbol{x}^{\bullet}$ does not coincide with a cell centroid and the flow state has to be interpolated. We use a first order Taylor expansion about the cell centroid approach which is illustrated in figure 3.3b. The first order terms are reconstructed using a least squares approach. Let us assume that the extrapolation point $\boldsymbol{x}^{\bullet}$ lies within cell $\mathscr{C}$ with cell centroid $\boldsymbol{x}^{\blacktriangle}$. Note that in general $\boldsymbol{x}^{\circ}$ is not in the same cell as $\boldsymbol{x}^{\bullet}$. Let $\mathscr{N}(\mathscr{C})$ be the neighbourhood of $\mathscr{C}$ which is defined to be the set of cells that share a face with $\mathscr{C}$. Then, the following first order approximation can be constructed for every cell in $\mathscr{N}$

$$\phi(\boldsymbol{x}_n^{\triangle}) = \phi(\boldsymbol{x}^{\blacktriangle}) + (\nabla\phi)(\boldsymbol{x}^{\blacktriangle})\cdot(\boldsymbol{x}_n^{\triangle} - \boldsymbol{x}^{\blacktriangle}) \qquad n \in \mathscr{N}\,, \tag{3.2}$$

where $\boldsymbol{x}_n^{\triangle}$ is the cell centroid of a cell $n \in \mathcal{N}$. Let us assume[1] that $\{\boldsymbol{x}_n^{\triangle} - \boldsymbol{x}^{\blacktriangle} | n \in \mathcal{N}\}$ generates the domain. The set of equations (3.2) gives either an overdetermined or a unique system with the unknown $(\nabla\phi)(\boldsymbol{x}^{\blacktriangle})$ which is solved in a least squares sense. Having obtained the gradient, the extraction state is calculated by

$$\phi^{\bullet} = \phi^{\blacktriangle} + (\nabla\phi)^{\blacktriangle} \cdot (\boldsymbol{x}^{\bullet} - \boldsymbol{x}^{\blacktriangle}) \,. \tag{3.3}$$

In summary, using the described routine we can associate a surface state $\phi^{\bullet}$ with every cut-cell in the domain. Although this approach can be used to extract the whole external flow state only a subset is relevant for the boundary layer computation and the water film model. In order to save memory only the following components are extracted:

$$\boldsymbol{u}^{\text{ext}} = \begin{pmatrix} \rho_{\text{a}} \\ \tilde{\boldsymbol{v}}_{\text{a}} \\ p_{\text{a}} \\ T_{\text{a}} \\ \sum_s \frac{1}{2}\rho_s \boldsymbol{v}_s^2 \\ \sum_s \rho_s \tilde{\boldsymbol{v}}_s \\ \sum_s e_s \end{pmatrix} , \tag{3.4}$$

where ρ denotes densities, $\boldsymbol{v}$ velocities, p pressures, T temperatures and e internal energies. The subscript $\cdot_{\text{a}}$ labels the air phase and $\cdot_s$ the droplet phase associated with the droplet diameter d_s. Vector components appended by $\tilde{\cdot}$ indicate that they are taken in the free surface frame i.e. the components are transformed to give tangential and normal components.

The other element of the data pair (s_i, ϕ_i), the surface coordinate s_i, is computed by finding the coordinate which minimises the distance between $\boldsymbol{x}^{\circ}$ and the substrate. Consequently, for every cut-cell the following optimisation is solved

$$s = \inf_{s \in U} d(\boldsymbol{x}^{\circ}, \underline{\boldsymbol{x}}(s)) \,, \tag{3.5}$$

where U is the coordinate space and $\underline{\boldsymbol{x}}$ the surface parameterisation. Details about the definition of these quantities are given in appendix A.

Finally, we need to map the data pairs (s_i, ϕ_i) which exist for every cut-cell to the surface mesh

---

[1] This may not be the case for concave regions with a large curvature compared to the cell size. However, we have not found this assumption to be restrictive.

on which the water and ice dynamic equations are solved. This is done by a straightforward piecewise cubic spline interpolation. The derivatives of the endpoints are determined by evaluating a finite difference approximation of the cut-cell data.

3.2 Boundary layer model

The inviscid methodology for the air flow requires an additional model to retrieve heat and shear stress transfer onto the ice film. These quantities are governed by the thermal and momentum boundary layer. Integral boundary layer methods have proven to be robust and efficient and are commonly used within ice accretion software e.g. LEWICE (Ruff and Berkowitz, 1990) and CANICE (Paraschivoiu and Saeed, 2001). More recently, research has been done on improving integral boundary layer models. Radenac et al. (2018) derived a model based on the Aupoix-Grigson-Colebrook (AGC) method and Blanchard et al. (2017) devised a method capable of modelling three-dimensional flow.

A comprehensive review of the available methods is beyond the scope of this thesis. Since we want to highlight improvements in the modelling of the droplet flow and the thin film dynamics, we implement a widely used method based on the Pohlhausen approximation. This allows us to compare our results against a wide selection of data from literature.

The employed boundary layer model does not feedback to the air flow or the droplet flow and we therefore restrict the following discussion to the air quantities only.

3.2.1 Pohlhausen method

Following the works by Ruff and Berkowitz (1990) and Leese (2010), we employ the Pohlhausen approximation to recover the velocity profile in the laminar boundary layer which is given by

$$\frac{v(\sigma,\hat{\eta})}{v^{\infty}(\sigma)} = 2\hat{\eta} - 2\hat{\eta}^3 + \hat{\eta}^4 + \frac{\Lambda}{6}\hat{\eta}(1-\hat{\eta})^3 \,. \tag{3.6}$$

Let $\hat{\eta} := \eta/\delta$, where η is the distance in the normal direction from the icing surface and δ is the boundary layer thickness. The symbol σ is the surface distance from the stagnation point which is determined by search for the root of the tangential velocity. The Greek letter Λ denotes the dimensionless Pohlhausen parameter which can be thought of as the ratio of pressure to viscous forces and is defined by

$$\Lambda = \frac{\delta^2}{\nu}\frac{\mathrm{d}\,v^{\infty}(\sigma)}{\mathrm{d}\sigma} \,. \tag{3.7}$$

The boundary layer thickness δ is approximated by $\delta \approx 8.5\theta$ according to Ruff and Berkowitz (1990) and for the momentum thickness θ the Thwaites quadrature approximation given by White and Corfield (2006) is used

$$\theta^2 \approx \frac{0.45\nu}{v^\infty(\sigma)} \int_0^\sigma v^\infty(s)\,\mathrm{d}s\,. \tag{3.8}$$

Plugging equation (3.6) into the definition of the shear stress and evaluating the derivative at the surface gives

$$\tau := \mu \left.\frac{\mathrm{d}v}{\mathrm{d}\eta}\right|_{\eta=0} = \mu\left(2+\frac{\Lambda}{6}\right)\frac{v^\infty}{\delta}\,. \tag{3.9}$$

The heat transfer coefficient h_c is directly related to the conduction thickness of the thermal boundary layer (White and Corfield, 2006). A simple approximation was developed by Smith and Spalding. Details about the approximation are given in White and Corfield (2006), and Spalding and Pun (1962). For a Prandtl number Pr of approximately 0.72 the approximation is given by

$$h = 0.296 k_\mathrm{a}\left(\nu_\mathrm{a}\left(v^\infty(\sigma)\right)^{-2.88}\int_0^\sigma \left(v^\infty(s)\right)^{-1.88}\mathrm{d}s\right)^{-\frac{1}{2}}\,. \tag{3.10}$$

In summary, equation (3.9) and (3.10) are used to compute the missing state variables required by the thin film dynamics model.

3.2.2 Transition to turbulence

So far, we have only considered a laminar boundary layer. However, in icing condition surface roughness plays an important role and can trip the flow producing a turbulent state. Kerho and Bragg (1997) experimentally investigated the difference in transition location for a smooth and rough aerofoil. They studied a NACA0012 and measured the transition point at various Reynolds numbers. For clean aerofoils, laminar boundary layers were found well past 30% of the chord length whereas rough surfaces induced a transition much earlier. Ice growth occurs in the vicinity of the leading edge. We therefore only consider roughness induced transitions in this work.

Criteria to determine the point of a roughness induced transition to a turbulent boundary layer were reported by von Doenhoff and Horton (1958). They performed experiments on a NACA 65-series aerofoil to determine how sand-grain type roughness affects the position of the turbulent transition and proposed a criteria based on the projection Reynolds number Re_k which is given by

$$\mathrm{Re}_k := \frac{v(\sigma, k_\mathrm{s})k_\mathrm{s}}{\nu}, \tag{3.11}$$

where k_s is the sand-grain roughness height of the ice surface. von Doenhoff and Horton (1958) found that if $\mathrm{Re}_k \leq 600$ the sand-grain roughness does not cause any disturbances to the laminar flow. For values larger than that turbulent spots appear.

If this is the case, then it turns out that the skin friction coefficient c_f is independent of viscosity according to Kays and Crawford (1980). This suggests that the pressure drag on the roughness elements is the leading effect as described by Ruff and Berkowitz (1990). The skin friction coefficient can then be approximated in terms of only the turbulent boundary layer thickness θ_t using a mixing length approach. Under the assumption of a constant free-stream velocity, the approximation is given by

$$\frac{c_\mathrm{f}}{2} = \left(\frac{0.41}{\log\left(\frac{864\theta_\mathrm{t}}{k_\mathrm{s}} + 2.568\right)} \right)^2 . \tag{3.12}$$

In order to calculate the boundary layer thickness of a point in the turbulent section the thickness of the laminar boundary layer of the transition point σ_tr is required.

$$\sigma_\mathrm{tr} = \inf\{\sigma \,|\, \mathrm{Re}_k(\sigma) > 600\} . \tag{3.13}$$

Once, the transition point is determined the turbulent boundary layer thickness θ_t is given by evaluating the following integral

$$\theta_\mathrm{t} = \theta(\sigma_\mathrm{tr}) + \left(\frac{0.0156\nu^{0.25}}{(v^\infty)^{4.11}} \int_{\sigma_\mathrm{tr}}^{\sigma} (v^\infty)^{3.86} \,\mathrm{d}s \right)^{0.8} . \tag{3.14}$$

The shear stress is given in terms of the skin friction coefficient:

$$\tau_\mathrm{t} = \frac{\rho (v^\infty)^2}{2} c_\mathrm{f} . \tag{3.15}$$

Similarly to the momentum boundary layer, Kays and Crawford (1980) model the thermal boundary layer using a mixing length approach. Additionally to the constant free-stream velocity assumption of the momentum boundary layer, Kays and Crawford (1980) assume that the momentum and thermal boundary layer are of the same thickness which is valid only in turbulent regimes. Under these constraints, the heat transfer coefficient for a fully rough surface is given by

$$h_\mathrm{t} = \rho v^\infty c_\mathrm{p} \frac{c_\mathrm{f}\,\mathrm{Sa}_k}{2\,\mathrm{Pr}_\mathrm{t}\,\mathrm{Sa}_k + \sqrt{2c_\mathrm{f}}} , \tag{3.16}$$

where c_p is the specific heat of air, Sa_k the roughness Stanton number and Pr_t the turbulent Prandtl number. Experimental data for air in icing conditions suggests using $\mathrm{Pr}_t \approx 0.9$ (Ruff and Berkowitz, 1990) and an empirical relation for the roughness Stanton number is given by

$$\mathrm{Sa}_k = 1.16\left(\frac{v_\tau k_\mathrm{s}}{\nu}\right)^{-0.2}, \tag{3.17}$$

where v_τ is the shear velocity which is given by

$$v_\tau = \sqrt{\frac{\tau_\mathrm{t}}{\rho}} = v^\infty \sqrt{\frac{c_\mathrm{f}}{2}}\,. \tag{3.18}$$

3.3 Surface roughness

We have seen in the previous section that the transition to a turbulent boundary layer depends on the surface roughness. Most ice accretion software use an empirical relation to determine the value of k_s.

The original LEWICE code defines an expression dependent on LWC the free stream temperature and the free stream velocity. However, numerical experiments carried out by Shin et al. (1991) suggest replacing the dependency on the velocity by the MVD. The improved roughness height relation is given by

$$k_s = 0.6839\, k_\mathrm{LWC}\, k_T\, k_\mathrm{MVD}\, k_\mathrm{base}\, c\,, \tag{3.19}$$

where c is the chord length and k_base is the baseline roughness assumed to be 0.00117. The remaining quantities modifier take into account the effect of the variables indicated by subscripts.

$$k_\mathrm{LWC} = 0.5714 + 245.7\alpha_\mathrm{d}\rho_\mathrm{d} + 1257100\alpha_\mathrm{d}^2\rho_\mathrm{d}^2\,, \tag{3.20}$$

where $\alpha_\mathrm{d}\rho_\mathrm{d}$ is the free stream LWC.

$$k_T = 0.047T - 11.27\,, \tag{3.21}$$

where T is the free stream equilibrium temperature.

$$k_\mathrm{MVD} = \sup\{0, \inf\{1, 1.666 - 33300 d_\mathrm{MVD}\}\}\,, \tag{3.22}$$

where d_MVD is the median of the droplet diameter distribution.

A different approach was presented as an improvement to LEWICE by Wright et al. (1997). The global roughness height is replaced by an expression taking into account the local state as described by Gent et al. (2000). More recently, Fortin et al. (2006) developed a roughness model based on the freezing process of the water film.

However, we employ the most widely used approach which is based on single global roughness height. Implementing the most popular method helps highlighting differences between the performance of the other improvements proposed in this work and existing methodologies. A comprehensive study and comparison of all roughness models is beyond the scope of this work, however, improving the boundary layer model constitutes an interesting and valuable direction of future research.

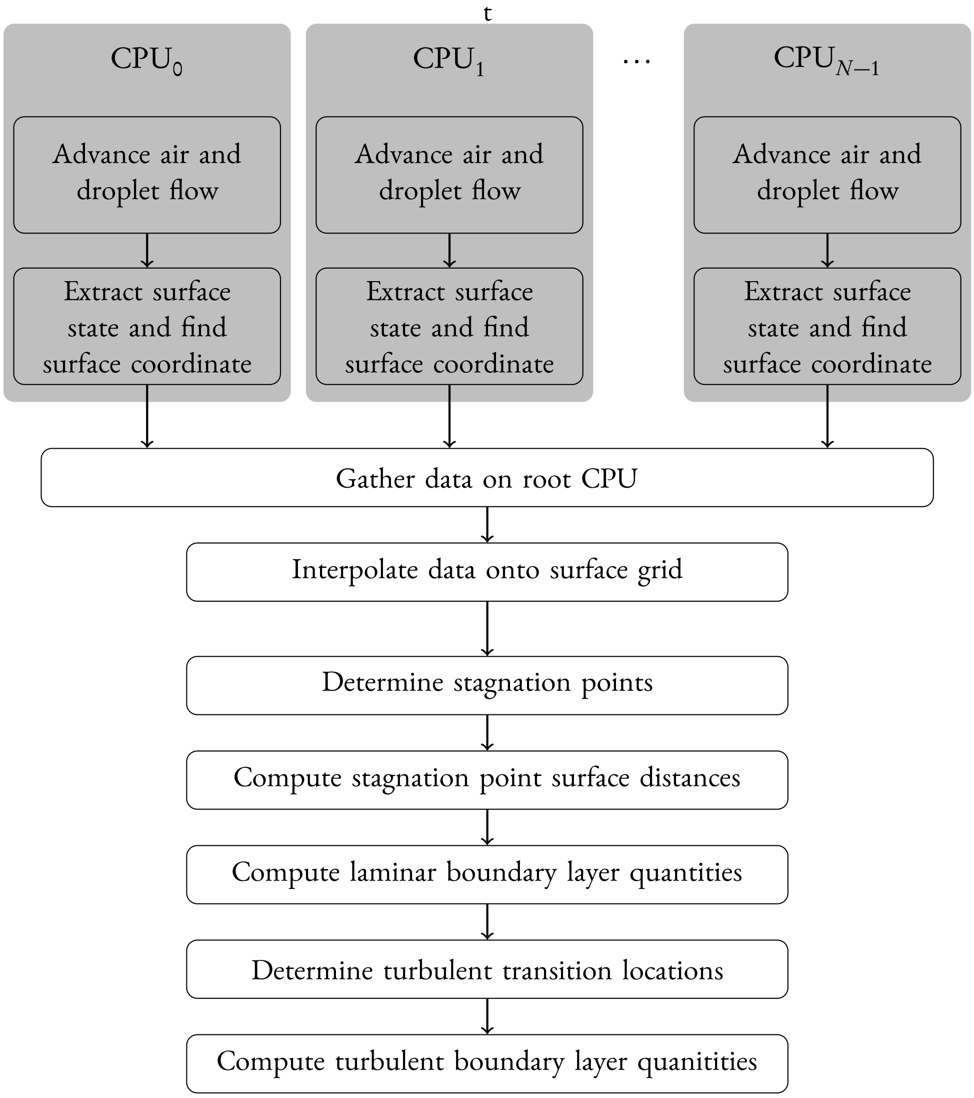

Figure 3.4: Flowchart of boundary layer computation. After the air and droplet flow is computed, the surface data is extracted in parallel. The data is gathered on the root CPU where the interpolation and boundary layer computation take place in serial.

3.4 Implementation

The extraction of surface states and boundary layer model routines presented in this chapter act as the link between two standalone frameworks: the air and droplet flow solver, and the thin film dynamics. For the sake of clarity, we present the implementation details of the approach to link the two codes. A flowchart of the implementation is illustrated in figure 3.4. Most importantly, the air and droplet simulation is built on the patch based Adaptive Mesh Refinement (AMR) approach by Bell et al. (1994). Every patch has a layer of ghost cells which allows the solvers to act on every patch without any information from neighbouring patches.

Every CPU has a list of local patches for which the updates need to be computed. After every advance routine, the presence of cut-cells is checked and the surface states are extracted and stored in a local buffer. After all patches are advanced the local buffers containing the surface states are gathered on the root process, interpolated and the remaining boundary layer quantities computed.

3.5 Validation

The purpose of this test is to validate the surface state extraction method described in section 3.1 and the integral boundary layer method introduced in section 3.2.1. In this section we study the air and droplet flow for typical icing conditions and a relevant geometry.

A similar approach was presented by Myers et al. (2002a) where they presented the surface results for pressure, collection efficiency, shear stress and heat transfer coefficient for a NACA 0012 geometry. Unfortunately, the initial and boundary conditions of the setup were not fully reported. We, therefore, cannot present a direct comparison with the results by Myers et al. (2002a), however, we expect the flow exhibit the same features and a qualitative comparison is possible. We use the core test case 4 from the NATO/RTO icing workshop by Kind (2001). A flow with a free stream velocity of $77.2\,\mathrm{m\,s^{-1}}$ a free stream temperature of $270.5\,\mathrm{K}$ and a free stream pressure of $99.6\,\mathrm{kPa}$ over a NACA 0012 is considered. Water droplets with a diameter of $18\,\mu\mathrm{m}$ and a liquid content of $0.32\,\mathrm{g\,m^{-3}}$ were introduced. The representation of the geometry is described in appendix A.

The initial conditions and the geometry are symmetric about the axis along the chord. We, therefore, expect an odd solution for tangential components of vector quantities and a solution which is even for scalar quantities. Due to these symmetries, it suffices to compute the boundary layers on either the upper or lower half of the aerofoil and extend the solution using the even (or odd) property from above. However, we decide to calculate the boundary layer on both sides of the aerofoil since the computation is inexpensive and we can assess the symmetry preservation properties of our implementation of the numerical method. In order to compare our data with the results by Myers et al. (2002a) we disable the turbulent transition and treat the whole boundary layer as laminar.

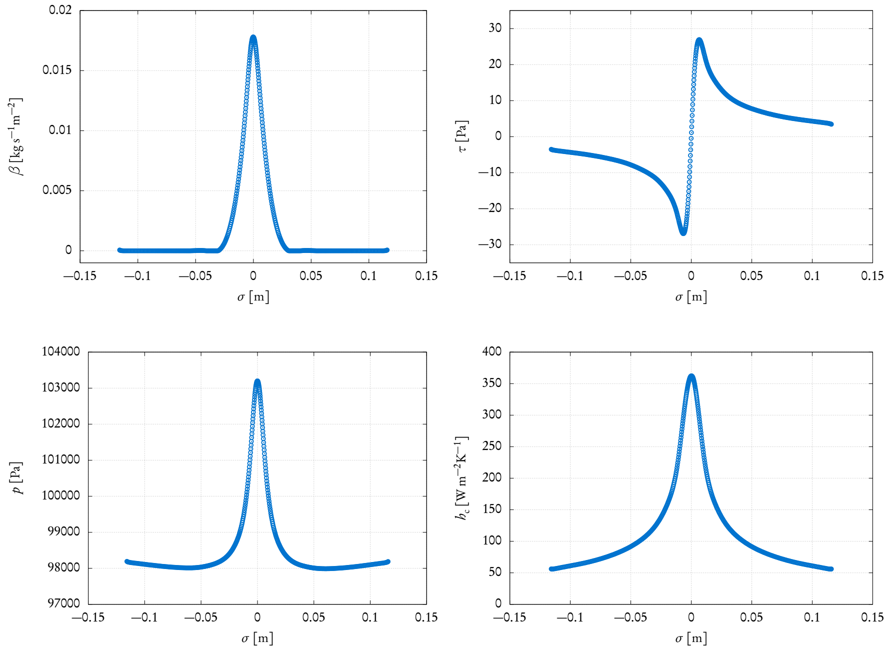

Figure 3.5: Validation test for surface extraction routine and boundary layer model. The surface data are extracted using the interpolation methodology described above. The quantities h_c and τ are computed using the integral boundary layer model. The models are applied to the NATO C4 test case.

The results are illustrated in figure 3.5. The first subfigure shows the collection efficiency which was validated in chapter 2. The other subfigures illustrate the surface shear stress, surface air pressure and surface heat transfer coefficient. We observe close qualitative agreement to the results by Myers et al. (2002a) for all quantities. Moreover, all solutions exhibit the expected symmetries.

Chapter 4

Modelling thin water film freezing

A crucial stage of an atmospheric ice accretion simulation is the prediction of water runback and ice growth. In rime ice conditions, only a simple conservation of mass equation is required. All of the impinging water droplets freeze immediately and stick to the surface. In milder conditions, i.e. if a liquid phase is present, the runback water becomes a significant part of the process. The water film dynamics may exhibit complex features such as finger formation and capillary ridges. Moreover, if SLDs are present, phenomena such as droplet splashing and rebounding complicate the problem even further. This chapter presents a novel framework of how to model the freezing of thin water film on a curved surface.

4.1 Introduction

We begin the chapter by introducing approaches which are most commonly used in ice accretion simulations. Following the discussion of the literature, we briefly summarise caveats and assumptions that went into the reviewed models and propose generalisations, extensions, and improvements.

4.1.1 Previous approaches

There are three methodologies commonly used in ice accretion simulations.

The control volume approach of Messinger

The first widely used attempt of simulating atmospheric ice accretion dates back to work by Messinger (1953). His approach is still the most commonly used model and employed ice accretions simulations such as TRAJICE2, LEWICE and CANICE (Kind, 2001). We only present a summary, more detail about his approach can be found in Messinger (1953) and Gent et al. (2000). The underlying idea is to track the water layer along the geometry surface. The process starts at the stagnation point where the only source of water is the droplet flux from the air. A mass ratio N_f of ice and water is computed using a thermodynamic balance. All of the liquid phase is subsequently pushed back into the next control volume and the energy balance is computed again.

One of the primary caveats of the control volume approach is that the runback water only depends on the thermodynamic balance. Physical forces such as shear stress exerted by the airflow, pressure gradients in the airflow and surface tension are not taken into account. Bourgault et al. (2000a) addressed these shortcomings by developing a shallow-water icing model.

The shallow-water icing model (SWIM)

Bourgault et al. (2000a) replaced the control volume approach with a continuum model of the water film. Since the water film remains thin, they assume that the velocity profile is linear in the substrate normal direction. A no-slip boundary condition and a continuity of shear stress constraint at the free surface close the system. These simplifications allow the analytic integration of the perpendicular conservation of momentum equation resulting in a system of two partial differential equations (PDEs). This approach extends the Messinger model in two essential ways. Firstly, air shear is included in the model basing the calculation of runback water on physical forces. Secondly, inertia effects of the film are included producing explicit time derivatives in the equations and allowing the capturing of mass fluxes within the film. Rothmayer and Tsao (2000) have found these effects to be an essential modelling component for thicker films.

The model has two inherent limitations. Firstly, Rothmayer and Tsao (2000) found that thicker films are mainly driven by air pressure gradients. However, the only modelled driving force in SWIM is shear stress making this model less suitable for thicker films. Secondly, the model's depth averaging approach cannot capture mode decay rates and equilibrium film heights simultaneously. This is an inherent but frequently overlooked issue in depth averaging methods as demonstrated by Roberts (2015, p. 299).

Stefan approach by Myers et al.

Myers and Hammond (1999) and Myers et al. (2002a,b) developed a system which is based on ideas similar to SWIM namely to model the runback water by physical forces. Instead of using a shallow water approach their model is based on lubrication theory. The inclusion of shear stress as a driving force as well as surface tension and air pressure gradients makes it physically more accurate than

SWIM. The set of governing equations splits into a subset for rime ice and glaze ice. In rime ice conditions the model is given by

$$\rho_\mathrm{i}\partial_t\zeta = -\rho_\mathrm{d}\alpha_\mathrm{d}\boldsymbol{v}_\mathrm{d}\cdot\bar{\boldsymbol{n}} + \mathcal{O}(\varepsilon^2, \mathrm{Pe}), \tag{4.1}$$

where ρ_i is the ice density, α_d is the droplet volume fraction, ρ_d is the microscopic droplet density, and $\boldsymbol{v}_\mathrm{d}$ is the droplet velocity. The symbol ζ denotes the ice height, $\bar{\boldsymbol{n}}$ the ice normal, ε the geometrical scaling factor and Pe the Peclet number, defined in section 4.2. In glaze ice conditions the governing equations are:

$$\frac{\partial\xi}{\partial t} + \boldsymbol{\nabla}\cdot\left(-(\boldsymbol{\nabla}p - \mathrm{Bo}\,\boldsymbol{g})\frac{\xi^3}{3} + \tau\frac{\xi^2}{2}\right) = -\frac{\rho_\mathrm{i}}{\rho_\mathrm{w}}\frac{\partial\zeta}{\partial t} - \alpha_\mathrm{d}\rho_\mathrm{d}\boldsymbol{v}_\mathrm{d}\cdot\tilde{\boldsymbol{n}} + \mathcal{O}(\varepsilon, \varepsilon^2\mathrm{Re}), \tag{4.2a}$$

$$p = p_\mathrm{a} - \sigma\tilde{H} + \mathcal{O}(\varepsilon^2), \tag{4.2b}$$

$$\mathrm{St}\,\frac{\partial\zeta}{\partial t} = \frac{1}{\zeta} - \frac{k_\mathrm{w}}{k_\mathrm{i}}\frac{E_{(0)} - E_{(1)}}{1 + E_{(1)}\zeta} + \mathcal{O}(\varepsilon^2, \mathrm{Pe}), \tag{4.2c}$$

where p denotes the water pressure, $\boldsymbol{g}$ gravity, τ the shear stress at the air-water surface, ρ_w the water density, and k_w and k_i the thermal conductivity of water and ice respectively. The remaining quantities are introduced in more detail in section 4.2. We list their names for completion here: ξ denotes the water height, $\tilde{H}$ the free surface curvature, Bo the Bond number, Re the Reynolds number, St the Stefan number. The factors $E_{(0)}$ and $E_{(1)}$ depend on the heat exchange at the free surface and are defined by Myers et al. (2002b).

Expressing the heat fluxes in this form implies an affine dependency on $T - T_\mathrm{a}$. This assumption is insufficient if more information about the droplet temperatures is available as another dependency on $T - T_\mathrm{d}$ is required.

Another caveat is the neglecting of internal forces. The film is assumed to be in equilibrium and the time derivative only enters through the dynamic surface. This makes the model less accurate for fast flows where inertial forces become essential as shown in literature (Oron and Bankoff, 1997; Roberts and Li, 2006; Sivapuratharasu et al., 2016; Rothmayer and Tsao, 2000).

Myers et al. (2002b) neglect several linear terms of ε in equation (4.2a). These expressions arise from the curvilinear coordinate system and are absent for thin films on a flat plate. Myers et al. (2002b) argues that the order ε of curvilinear terms is comparable to $\varepsilon^2\,\mathrm{Re}$ of inertia terms and therefore also negligible. However, as research by Rothmayer and Tsao (2000) has shown, inertia terms are significant rendering neglecting $\mathcal{O}(\varepsilon)$ problematic.

Moreover, system (4.1)-(4.2c) was derived under the assumption that the surface is parameterised in principal directions. Although such a representation always exists, it may not be known for complex surfaces arising from real-world wing geometries with slats and flaps.

Other related work

More recently primarily theoretical research has been directed towards coupling between the air boundary layer, roughness and the thin film flow. Rothmayer and Tsao (2000) and Rothmayer et al. (2002) studied interfacial waves on thin liquid films. They found that the lubrication theory model holds as long as the film remains thin and that the primary driving force is air shear. As the film grows, however, the air shear stress is replaced by air pressure gradients as the dominant driver. Moreover, inertia effects, i.e. mass fluxes within the film, become significant. Moore et al. (2017) and Nelson et al. (1995) studied the ice formation in a Blasius boundary layer. These coupled methods are beyond the scope of this work but comprise an exciting direction for future extensions of a full ice accretion software.

4.1.2 Conclusions of literature review

In summary, there are two regimes for thin film flow. Thin films are driven by air shear and are well approximated by lubrication theory. Films thicker than a critical depth are governed by interfacial waves driven by air pressure gradients. In order to capture this behaviour, the interaction between the water and the air needs to be modelled. A lubrication theory approach does not suffice. Models that capture these phenomena are not mature enough to be used in a full ice accretion simulation and are therefore beyond the scope of this work. We will, however, keep the shortcomings in mind and point to possibilities of future work where the application of a coupled model is advisable.

4.1.3 Outline of this chapter

The remainder of this chapter is based on the thin film approach by Myers et al. (2002b). We address the shortcomings of the model by Myers presented in section 4.1.1. Section 4.2.1 defines essential symbols, notations and conventions of this chapter. In section 4.2 we generalise the derivation of the governing equations to arbitrarily parameterised surfaces. We also extend the discussion to coherently include all linear terms in ε. Subsequently, the model and implementation are validated. The effects of the linear terms are demonstrated by studying the drop formation on the underside of a cylinder In section 4.7 the Stefan problem is extended to incorporate dependencies on the droplet temperature to make use of the novel improvements introduced in chapter 2.

4.2 The generalisation for arbitrarily parameterised surfaces

In this section, we derive the thin film limit of the Navier Stokes equations on an arbitrary smoothly curved surface. The derivation of this kind of equation for a flat substrate, which can be expressed in Cartesian coordinates, can be found in many elementary fluid dynamic textbooks, e.g. Batchelor G. K. (2000).

The general approach is as follows: The governing equations are expressed in a Cartesian coordinate system with the orthonormal basis $\{\boldsymbol{e}_x, \boldsymbol{e}_y, \boldsymbol{e}_z\}$. The xy-plane describes the substrate and a parameter ε is introduced to scale the perpendicular component. Hence, a point in space $\boldsymbol{x} \in \mathbb{R}^3$ can be written as:

$$\boldsymbol{x} = x\boldsymbol{e}_x + y\boldsymbol{e}_y + \varepsilon z\boldsymbol{e}_z \; . \tag{4.3}$$

A suitable choice of ε scales the perpendicular component such that it matches the order of the tangential components. This is effectively the ratio of the height over the extent of the film. The assumptions that the film remains thin implies that ε is small allowing the power series expansion of the governing equations in terms of order ε. Truncating second and higher order terms, we analytically integrate the series over the normal component giving a single partial differential equation governing the height of the film.

In order to generalise this approach to curved substrates, we follow the same underlying approach as in the flat plate derivation. The main difference is that the governing equations are expressed in terms of tangential coordinates which determine the position on the substrate and a scaled perpendicular coordinate which describes the distance to the surface.

Roy et al. (2002) studied gravity-driven flows on surfaces parameterised in principal directions. Thiffeault and Kamhawi (2006) generalised the system to arbitrary parameterisation. Myers et al. (2002a) included shear stress at the free surface and air pressure gradients. However, they also restricted the surface representation to a diagonal second fundamental form. In what follows, we present a lubrication theory approach to shear stress driven thin film flow. We consistently include linear terms and lift the restriction to a principal parameterisation. To the best of our knowledge, a derivation of this level of generality is the first in the literature.

4.2.1 Surfaces, manifolds and notation

The problem consists of four domains: the substrate, the ice layer, the water layer and the surrounding air as illustrated in figure 4.1. These domains are separated by three interfaces which are mathematically represented by manifolds.

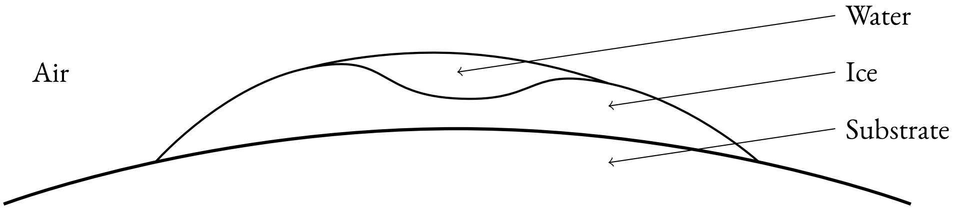

Figure 4.1: Illustration of the problem to be modelled to predict the extent of the ice layer. Supercooled water droplets impinge onto the surface which is at subzero temperature. Some of the water freezes forming an ice layer on top of the substrate and some of the water will remain liquid forming a water layer.

Cartesian coordinate system

The Euclidean space $\mathbb{R}^3$ with the natural basis $\{\boldsymbol{e}_1, \boldsymbol{e}_2, \boldsymbol{e}_3\}$ equipped with the dot product $\langle\cdot|\cdot\rangle$ acts as an embedding space. This space induces a metric and fundamental forms and is suited to define other relevant geometrical concepts such as curvature.

Substrate

At the base of our considerations is the substrate which we define in the following manner. Let $\underline{\mathcal{M}}$ be a parametric surface given by the parameterisation $\underline{\boldsymbol{x}} : \mathbb{R}^2 \supseteq U \to \mathbb{R}^3$ with $(s^1, s^2) \mapsto \underline{\boldsymbol{x}}(s^1, s^2)$. The substrate consists of all the points in the image of the parameterisation $\underline{\boldsymbol{x}}(U)$. This is a generalisation over the approach of Myers et al. (2002a) and Roy et al. (2002) which requires the parameterisation to be in principal directions. Even though there always exists a parameterisation in principal directions for complicated surfaces, it might be hard to find, or it might produce in a poor surface mesh.

We use the parameterisation which induces many useful concepts. Primarily, a basis of the tangent space $T\underline{\mathcal{M}}$ given by $\{\underline{\boldsymbol{x}}_\mu\}$ where $\underline{\boldsymbol{x}}_\mu = \partial_\mu \underline{\boldsymbol{x}}$ and the first fundamental form of the substrate $\underline{a}$ which is defined by:

$$\underline{a}_{\mu\nu} = \langle \underline{\boldsymbol{x}}_\mu | \underline{\boldsymbol{x}}_\nu \rangle \,, \tag{4.4}$$

where the indices $\mu, \nu \in \{1,2\}$. In general, we adopt the convention that Latin indices range over $(1,2,3)$ and indicate quantities that live in the three-dimensional space whereas Greek indices range only over $(1,2)$ and are associated with quantities that are defined on a submanifold such as the substrate. Furthermore, quantities that live on the substrate are labelled by $\underline{\cdot}$. Another essential quantity of the substrate is the normal field $\underline{\boldsymbol{n}}$ which is defined by

(i) $||\underline{\boldsymbol{n}}|| = 1$,

(ii) $\langle \underline{\boldsymbol{n}} | \underline{\boldsymbol{x}}_{\mu} \rangle = 0$,

(iii) $\underline{\boldsymbol{n}}$ is outward pointing.

The second fundamental form of the substrate $\underline{b}$ is defined by

$$\underline{b}_{\mu\nu} = \langle \underline{\boldsymbol{x}}_{\mu\nu} | \underline{\boldsymbol{n}} \rangle \,, \tag{4.5}$$

where $\underline{\boldsymbol{x}}_{\mu\nu} = \partial_{\mu} \partial_{\nu} \underline{\boldsymbol{x}}$. These are essential geometrical quantities and straightforwardly computed when given a parameterisation.

Substrate coordinate system

Based on the manifold $\underline{\mathscr{M}}$ introduced in the previous section a three-dimensional coordinate system is constructed. We define this coordinate system such that the surface normal maps to a single coordinate, thereby reducing the effective dimensionality. This is done analogously to the thin film derivation on a flat substrate (see equation (4.3)). Components one and two of the position vector describe the position on the substrate and the third coordinate measures the distance perpendicular to the substrate. The parameterisation is given by:

$$\boldsymbol{x}(s^1, s^2, \eta) = \underline{\boldsymbol{x}}(s^1, s^2) + \varepsilon\, \eta\, \underline{\boldsymbol{n}}(s^1, s^2) \,, \tag{4.6}$$

where ε is a small constant which scales the normal coordinate to be of the same order of magnitude as the position on the substrate. The induced metric g of this coordinate system is given by:

$$g_{ij} = \langle \boldsymbol{x}_i | \boldsymbol{x}_j \rangle \,. \tag{4.7}$$

The notion of a metric g is identical to that of a first fundamental form a. We use the convention of calling it g or metric in three-dimensional space and a or first fundamental form on a surface. The non-vanishing elements of g are:

$$\begin{aligned} g_{\alpha\beta} &= \underline{a}_{\alpha\beta} - 2\varepsilon\eta \underline{b}_{\alpha\beta} + \varepsilon^2 \eta^2 \underline{b}_{\alpha\gamma} \underline{b}^{\gamma}_{\beta} \,, \\ g_{33} &= \varepsilon^2 \,, \end{aligned} \tag{4.8}$$

where we have used the Einstein summation convention which implies a summation if an index appears twice in an expression — once as subscript and once as superscript. For example, equation (4.8) is summed over γ. Indices are lowered by using the metric g_{ij} or where appropriate the first fundamental form $a_{\mu\nu}$. Indices are raised by using the inverse metric g^{ij}. The tensor g_{ij} is block diagonal, therefore, it is sufficient to find the inverse of the top left block. Terms of the order ε^2 are neglected as customary. In order to find the inverse of the submatrix, we consider the following lemma. Let A be an invertible matrix, B a square matrix and $||BA^{-1}|| < 1$ then

$$(A-B)^{-1} = \sum_{k=0}^{\infty} A^{-1}\left(BA^{-1}\right)^k \,, \tag{4.9}$$

which can be shown by considering:

$$\begin{aligned}
\lim_{n\to\infty}(A-B)\sum_{k=0}^{n}A^{-1}\left(BA^{-1}\right)^k &= \lim_{n\to\infty}\sum_{k=0}^{n}AA^{-1}\left(BA^{-1}\right)^k - \sum_{k=0}^{n}BA^{-1}\left(BA^{-1}\right)^k \\
&= \lim_{n\to\infty}\sum_{k=0}^{n}\left(I-BA^{-1}\right)\left(BA^{-1}\right)^k = \\
&= \left(I-BA^{-1}\right)\lim_{n\to\infty}\sum_{k=0}^{n}\left(BA^{-1}\right)^k \,.
\end{aligned} \tag{4.10}$$

The infinite sum in the last expression is a Neumann series which concludes the proof of this lemma. The form of the submatrix $g_{\alpha\beta}$ in (4.8) can be recovered by setting $A = \underline{a}$ and $B = 2\varepsilon\eta\underline{b} - \varepsilon^2\eta^2\underline{a}^{-1}\,\underline{b}$. We do not give a proof for convergence, but it is a reasonable assumption since $||BA^{-1}|| = \mathcal{O}(\varepsilon)$. Hence, the inverse up to the order ε^2 is given by:

$$\begin{aligned}
\left(\underline{a} - 2\varepsilon\eta\underline{b} + \varepsilon^2\eta^2\underline{a}^{-1}\underline{b}\right)^{-1} &= \sum_{k=0}^{\infty}\underline{a}^{-1}\left[\left(2\varepsilon\eta\underline{b} - \varepsilon^2\eta^2\underline{a}^{-1}\underline{b}\right)\underline{a}^{-1}\right]^k \\
&= \underline{a}^{-1} + 2\varepsilon\eta\underline{a}^{-1}\underline{b}\,\underline{a}^{-1} + \mathcal{O}(\varepsilon^2)\,.
\end{aligned} \tag{4.11}$$

Giving for the non-vanishing components of the inverse metric

$$\begin{aligned}
g^{\alpha\beta} &= \underline{a}^{\alpha\beta} + 2\varepsilon\eta\underline{b}^{\alpha\beta} + \mathcal{O}(\varepsilon^2)\,, \\
g^{33} &= \varepsilon^{-2}\,.
\end{aligned} \tag{4.12}$$

In a non-Cartesian space, the covariant derivative[1] has to also take into account the change of the embedding which can be expressed in terms of the Christoffel symbols Γ^k_{ij}. The Christoffel symbols

---

[1] Since we use an embedding into Euclidean space, we use covariant derivative, affine connection and Levi-Civita connection interchangeably.

of the second kind in coordinate form are defined in terms of the metric by

$$\Gamma^i_{jk} = \frac{1}{2} g^{im} \left(\partial_j g_{mk} + \partial_k g_{jm} - \partial_m g_{jk} \right) . \tag{4.13}$$

The non-vanishing elements of relevant order are

$$\begin{aligned} \Gamma^3_{\mu\nu} &= \Gamma^3_{\nu\mu} = \varepsilon^{-1} \underline{b}_{\mu\nu} - \eta \underline{c}_{\mu\nu} , \\ \Gamma^\lambda_{3\mu} &= \Gamma^\lambda_{\mu 3} = -\varepsilon \underline{b}^\lambda_\mu + \mathcal{O}(\varepsilon^2) , \\ \Gamma^\lambda_{\mu\nu} &= \Gamma^\lambda_{\nu\mu} = \underline{\Gamma}^\lambda_{\mu\nu} + \mathcal{O}(\varepsilon) , \end{aligned} \tag{4.14}$$

where $\underline{c}$ is the third fundamental form and $\underline{\Gamma}$ are the substrate Christoffel symbols which are computed using the substrate first fundamental form

$$\underline{\Gamma}^\lambda_{\mu\nu} = \frac{1}{2} \underline{a}^{\lambda\sigma} \left(\partial_\mu \underline{a}_{\sigma\nu} + \partial_\nu \underline{a}_{\mu\sigma} - \partial_\sigma \underline{a}_{\mu\nu} \right) . \tag{4.15}$$

Ice-water interface

The manifold representing the ice-water interface $\overline{\mathcal{M}}$ is obtained by using the parameterisation (4.6). The normal coordinate η is replaced by a function $\zeta : \mathbb{R}_+ \times U \to \mathbb{R}_+$ which is time-dependent and governs the height of the ice layer scaled by ε. The quantities are illustrated in figure 4.2. The parameterisation of the ice-water manifold is given by:

$$\bar{\boldsymbol{x}}(t, s^\mu) = \boldsymbol{x}(s^\mu, \zeta(t, s^\mu)) = \underline{\boldsymbol{x}}(s^\mu) + \varepsilon\, \zeta(t, s^\mu)\, \underline{\boldsymbol{n}}(s^\mu) . \tag{4.16}$$

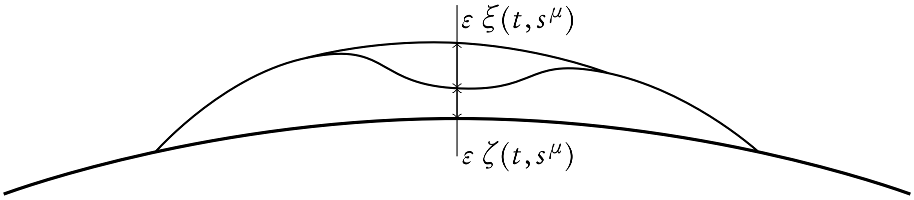

Figure 4.2: Illustration of the quantisation of the ice and water layer. The functions ζ and ξ which describe the ice height and water height in the direction normal to the substrate i.e. along $\underline{\boldsymbol{n}}$ scaled by ε.

Water-air interface

The manifold representing the free surface $\tilde{\mathscr{M}}$ is obtained setting $\eta = (\zeta + \xi)(t, s^\mu)$ in equation (4.6) where $\xi : \mathbb{R}^+ \times U \to \mathbb{R}^+$ represents the height of the water film scaled by a constant ε (see figure 4.2). Consequently, the manifold parameterisation is given by

$$\tilde{\boldsymbol{x}} = \boldsymbol{x}(s^\mu, (\zeta + \xi)(t, s^\mu)) = \underline{\boldsymbol{x}}(s^\mu) + \varepsilon\,(\zeta + \xi)(t, s^\mu)\,\underline{\boldsymbol{n}}(s^\mu)\,, \tag{4.17}$$

Similarly to the previous surfaces, quantities on this manifold are denoted by $\tilde{\cdot}$.

We construct the normal to the free surface $\tilde{\boldsymbol{n}}$ using a Gram-Schmidt approach. We choose $\underline{\boldsymbol{n}}$ as the starting vector which is linearly independent of the free surface tangent space under the thin film assumption. The normal is then given by

$$\tilde{\boldsymbol{n}} = \underline{\boldsymbol{n}} - \varepsilon \underline{a}^{\alpha\beta}\partial_\alpha(\zeta + \xi)\underline{\boldsymbol{x}}_\beta + \mathcal{O}(\varepsilon^2)\,. \tag{4.18}$$

The proof is straightforward by, firstly, checking $\langle \tilde{\boldsymbol{n}} | \tilde{\boldsymbol{x}}_\mu \rangle = 0$ and, secondly, that the expression is normalised. Plugging in expressions (4.18) and (4.17) we find that the only non-orthogonal terms are:

$$\langle \tilde{\boldsymbol{n}} | \tilde{\boldsymbol{x}}_\mu \rangle = \varepsilon(\zeta + \xi)_\mu - \varepsilon \underline{a}^{\alpha\beta}(\zeta + \xi)_\alpha \langle \underline{\boldsymbol{x}}_\beta | \underline{\boldsymbol{x}}_\mu \rangle + \mathcal{O}(\varepsilon^2) = \mathcal{O}(\varepsilon^2)\,. \tag{4.19}$$

Hence, $\tilde{\boldsymbol{n}} \in (T\tilde{\mathscr{M}})^\perp$. Since $\underline{\boldsymbol{n}} \in (T\underline{\mathscr{M}})^\perp$ the norm up to second order can be expressed as

$$||\tilde{\boldsymbol{n}}|| = \left\| \underline{\boldsymbol{n}} - \varepsilon \underline{a}^{\alpha\beta}(\zeta + \xi)_\alpha \underline{\boldsymbol{x}}_\beta \right\| = \left(1 + ||\varepsilon \underline{a}^{\alpha\beta}(\zeta + \xi)_\alpha \underline{\boldsymbol{x}}_\beta||^2\right)^{\frac{1}{2}} = 1 + \mathcal{O}(\varepsilon^2)\,, \tag{4.20}$$

and we find that the expression is normalised.

Let us now turn to the computation of the second fundamental form at the free surface $\tilde{b}$ which is given by

$$\tilde{b}_{\alpha\beta} = \langle \tilde{\boldsymbol{x}}_{\alpha\beta} | \tilde{\boldsymbol{n}} \rangle\,. \tag{4.21}$$

Plugging in the expression for $\tilde{\boldsymbol{x}}_{\alpha\beta}$ gives

$$\tilde{b}_{\alpha\beta} = \langle \underline{\boldsymbol{x}}_{\alpha\beta} | \tilde{\boldsymbol{n}} \rangle + \varepsilon(\zeta + \xi)\langle \underline{\boldsymbol{n}}_{\alpha\beta} | \tilde{\boldsymbol{n}} \rangle + \varepsilon(\zeta + \xi)_\alpha \langle \underline{\boldsymbol{n}}_\beta | \tilde{\boldsymbol{n}} \rangle + \varepsilon(\zeta + \xi)_\beta \langle \underline{\boldsymbol{n}}_\alpha | \tilde{\boldsymbol{n}} \rangle + \varepsilon(\zeta + \xi)_{\alpha\beta} \langle \underline{\boldsymbol{n}} | \tilde{\boldsymbol{n}} \rangle\,. \tag{4.22}$$

Further substitution of equation (4.18) gives

$$\begin{aligned}\tilde{b}_{\alpha\beta} = \langle \underline{\boldsymbol{x}}_{\alpha\beta} | \underline{\boldsymbol{n}} \rangle + \varepsilon(\zeta+\xi)\langle \underline{\boldsymbol{n}}_{\alpha\beta} | \underline{\boldsymbol{n}} \rangle + \varepsilon(\zeta+\xi)_{\alpha}\langle \underline{\boldsymbol{n}}_{\beta} | \underline{\boldsymbol{n}} \rangle + \varepsilon(\zeta+\xi)_{\beta}\langle \underline{\boldsymbol{n}}_{\alpha} | \underline{\boldsymbol{n}} \rangle + \\ + \varepsilon(\zeta+\xi)_{\alpha\beta}\langle \underline{\boldsymbol{n}} | \underline{\boldsymbol{n}} \rangle - \varepsilon \underline{a}^{\gamma\delta}(\zeta+\xi)_{\gamma}\langle \underline{\boldsymbol{x}}_{\alpha\beta} | \underline{\boldsymbol{x}}_{\delta} \rangle + \mathcal{O}(\varepsilon^2)\,.\end{aligned} \tag{4.23}$$

According to the Weingarten equations $\langle \underline{\boldsymbol{n}}_{\alpha} | \underline{\boldsymbol{n}} \rangle = -\underline{b}_{\alpha}^{\beta}\langle \underline{\boldsymbol{x}}_{\beta} | \underline{\boldsymbol{n}} \rangle = 0$ and a number of terms vanish giving

$$\tilde{b}_{\alpha\beta} = b_{\alpha\beta} + \varepsilon(\zeta+\xi)\langle \underline{\boldsymbol{n}}_{\alpha\beta} | \underline{\boldsymbol{n}} \rangle + \varepsilon(\zeta+\xi)_{\alpha\beta} - \varepsilon \underline{a}^{\gamma\delta}(\zeta+\xi)_{\gamma}\langle \underline{\boldsymbol{x}}_{\alpha\beta} | \underline{\boldsymbol{x}}_{\delta} \rangle + \mathcal{O}(\varepsilon^2)\,. \tag{4.24}$$

Plugging in the definition of the Christoffel symbols of the second kind by Frankel (2011, p. 229) we can express the derivative of $(\zeta+\xi)$ as the covariant derivative $\underline{\nabla}_{\alpha}$

$$\begin{aligned}\tilde{b}_{\alpha\beta} &= \underline{b}_{\alpha\beta} - \varepsilon(\zeta+\xi)\langle \partial_{\alpha}\underline{b}_{\beta}^{\gamma}\underline{\boldsymbol{x}}_{\gamma} | \underline{\boldsymbol{n}} \rangle + \varepsilon(\zeta+\xi)_{\alpha\beta} - \varepsilon(\zeta+\xi)_{\gamma}\underline{\Gamma}_{\alpha\beta}^{\gamma} + \mathcal{O}(\varepsilon^2) = \\ &= \underline{b}_{\alpha\beta} + \varepsilon(\zeta+\xi)\underline{b}_{\beta}^{\gamma}\underline{b}_{\gamma\alpha} - \varepsilon(\zeta+\xi)(\partial_{\alpha}\underline{b}_{\beta}^{\gamma})\langle \underline{\boldsymbol{x}}_{\gamma} | \underline{\boldsymbol{n}} \rangle + \varepsilon(\zeta+\xi)_{\alpha\beta} - \varepsilon(\zeta+\xi)_{\gamma}\underline{\Gamma}_{\alpha\beta}^{\gamma} + \\ &\qquad + \mathcal{O}(\varepsilon^2) = \\ &= \underline{b}_{\alpha\beta} + \varepsilon(\zeta+\xi)\underline{b}_{\alpha}^{\gamma}\underline{b}_{\gamma\beta} + \varepsilon\underline{\nabla}_{\alpha}(\zeta+\xi)_{\beta} + \mathcal{O}(\varepsilon^2)\,.\end{aligned} \tag{4.25}$$

The second fundamental form of the free surface $\tilde{b}$ is an essential factor in the dynamics of the thin film. It encodes information about the curvature of the air-water interface which according to the Young-Laplace equation exerts a pressure onto the water film proportional to the surface tension.

4.2.2 Dimensional analysis of the Navier Stokes equations

In this section, we express the governing equations in terms of the substrate coordinate system given in (4.6). The introduction of the aspect ratio ε earlier allows the quantification of the *thinness* of the problem.

After determining the metric of the conveniently constructed coordinate system $\boldsymbol{x}$, we can rewrite the differential operators of the Navier-Stokes equations. Recall the incompressible steady Navier-Stokes equation.

$$\boldsymbol{\nabla} \cdot \boldsymbol{u} = 0\,, \tag{4.26a}$$

$$(\boldsymbol{u} \cdot \boldsymbol{\nabla})\,\boldsymbol{u} = -\frac{1}{\rho}\nabla p + \nu\nabla^2\boldsymbol{u}\,. \tag{4.26b}$$

We will later see that many of terms contain ε^{-2}. We preemptively multiply by ε^2 to keep the smallest order to be ε^0. Written in terms of the coordinate basis $\{\boldsymbol{x}_i\}$ we obtain

$$\varepsilon^2 u^j \nabla_j u^i = -\frac{\varepsilon^2}{\rho} g^{ij} \nabla_j p + \varepsilon^2 \nu \nabla_j g^{jk} \nabla_k u^i \,. \tag{4.27}$$

The next step separates the thin direction from the tangential ones. Two differential operators appear in the equation: the vector Laplacian and the convective operator.

The vector Laplacian is defined in an analogous way to the scalar Laplacian as the divergence of the gradient. Applying it to a vector field $\boldsymbol{u}$ gives

$$\nabla^2 u^k = \partial_i g^{ij} \left(\partial_j u^k + u^l \Gamma^k_{jl}\right) + \Gamma^i_{mi} g^{mj} \left(\partial_j u^k + u^l \Gamma^k_{jl}\right) + \Gamma^k_{mi} g^{ij} \left(\partial_j u^m + u^l \Gamma^m_{jl}\right) \,. \tag{4.28}$$

The convective operator of a vector field $\boldsymbol{u}$ is given by:

$$u^j \nabla_j u^i = u^j \partial_j u^i + u^j u^k \Gamma^i_{jk} \,. \tag{4.29}$$

For clarity, we discuss the differential operators in tangential and perpendicular directions separately.

Tangential equation

The μ component of the convective operator of u takes the form

$$\begin{aligned} u^j \nabla_j u^\mu &= u^j \partial_j u^\mu + u^j u^k \Gamma^\mu_{jk} = u^j \partial_j u^\mu + u^\nu u^\rho \underline{\Gamma}^\mu_{\nu\rho} + \mathcal{O}(\varepsilon) = \\ &= u^3 \partial_3 u^\mu + u^\nu \partial_\nu + u^\nu u^\rho \underline{\Gamma}^\mu_{\nu\rho} + \mathcal{O}(\varepsilon) = u^3 \partial_3 u^\mu + u^\nu \underline{\nabla}_\nu u^\nu u^\mu + \mathcal{O}(\varepsilon) \,. \end{aligned} \tag{4.30}$$

The first term of the vector Laplacian given in equation (4.28) takes the expanded form

$$\begin{aligned} &\varepsilon^2 \partial_i g^{ij} \left(\partial_j u^\mu + u^l \Gamma^\mu_{jl}\right) = \\ &\quad = \varepsilon^2 \left(\partial_\alpha g^{\alpha j} + \partial_3 g^{3j}\right)\left(\partial_j u^\mu + u^\beta \Gamma^\mu_{j\beta} + u^3 \Gamma^\mu_{j3}\right) = \\ &\quad = \varepsilon^2 \partial_\alpha g^{\alpha\gamma} \left(\partial_\gamma u^\mu + u^\beta \Gamma^\mu_{\gamma\beta} + u^3 \Gamma^\mu_{\gamma 3}\right) + \partial_3 \left(\partial_3 u^\mu + u^\beta \Gamma^\mu_{3\beta} + u^3 \Gamma^\mu_{33}\right) = \\ &\quad = \partial_3 \left(\partial_3 u^\mu + u^\beta \Gamma^\mu_{3\beta}\right) + \mathcal{O}(\varepsilon^2) = \partial_3^2 u^\mu - \varepsilon \underline{b}^\mu_\beta \partial_3 u^\beta + \mathcal{O}(\varepsilon^2) \,, \end{aligned} \tag{4.31}$$

the second term:

$$\begin{aligned}\varepsilon^2\Gamma^i_{mi}g^{mj}\left(\partial_j u^k + u^l\Gamma^k_{jl}\right) &= \varepsilon^2\Gamma^i_{mi}\left(g^{m\beta}\partial_\beta u^k + g^{m\beta}u^l\Gamma^k_{\beta l} + g^{m3}\partial_3 u^k + g^{m\beta}u^l\Gamma^k_{3l}\right)\\ &= \varepsilon^2\Gamma^i_{mi}\left(g^{m3}\partial_3 u^k + g^{m3}u^\beta\Gamma^k_{3\beta} + g^{m3}u^3\Gamma^k_{33}\right) + \mathcal{O}(\varepsilon^2) =\\ &= \varepsilon^2\Gamma^\alpha_{3\alpha}\left(\varepsilon^{-2}\partial_3 u^k + \varepsilon^{-2}u^\beta\Gamma^k_{3\beta}\right) + \mathcal{O}(\varepsilon^2) =\\ &= -\varepsilon^3\underline{b}^\alpha_\alpha\left(\varepsilon^{-2}\partial_3 u^k - \varepsilon^{-1}u^\beta\underline{b}^k_\beta\right) + \mathcal{O}(\varepsilon^2) =\\ &= -\varepsilon\underline{b}^\alpha_\alpha\partial_3 u^k + \mathcal{O}(\varepsilon^2)\,,\end{aligned} \tag{4.32}$$

and the third term:

$$\begin{aligned}\varepsilon^2\Gamma^\mu_{mi}g^{ij}\left(\partial_j u^m + u^l\Gamma^m_{jl}\right) &= \varepsilon^2\left(\Gamma^\mu_{m\nu}g^{\nu j} + \Gamma^\mu_{m3}g^{3j}\right)\left(\partial_j u^m + u^l\Gamma^m_{jl}\right) =\\ &= \varepsilon^2\Gamma^\mu_{m\nu}g^{\nu\alpha}\left(\partial_\alpha u^m + u^l\Gamma^m_{\alpha l}\right) + \Gamma^\mu_{m3}\left(\partial_3 u^m + u^l\Gamma^m_{3l}\right) =\\ &= \Gamma^\mu_{\nu 3}\left(\partial_3 u^\nu + u^l\Gamma^\nu_{3l}\right) + \mathcal{O}(\varepsilon^2) = -\varepsilon\underline{b}^\mu_\nu\partial_3 u^\nu + \mathcal{O}(\varepsilon^2)\,.\end{aligned} \tag{4.33}$$

The spatial quantities are already non-dimensionalised by the introduction of the parameter ε in the previous section. Consequently, the extent of the film is of order 1 and the height of the film is of order ε. Non-geometrical terms still carry a dimensional scale. In order to assess the scaling of these terms, the remaining quantities are scaled as follows.

$$u^i = U\hat{u}^i\,, \qquad p = P\hat{p}\,, \tag{4.34}$$

where $\hat{\cdot}$ denotes non-dimensional quantities and capital letters the scale. As it is the convention, we drop the $\hat{\cdot}$ notation from now on. The tangential momentum equations read

$$\varepsilon^2 u^j\nabla_j u^i = -\varepsilon^2\frac{P}{\rho}g^{\mu i}\partial_i p + \varepsilon^2\nu U\nabla_i g^{ij}\nabla_j u^\mu\,. \tag{4.35}$$

Multiplying by $\nu^{-1}U^{-1}$, plugging in the results from equations (4.31) — (4.33), and collecting terms of order ε^2 gives

$$0 = -\frac{P\varepsilon^2}{\rho\nu U}g^{\mu\nu}\partial_\nu p + \partial_3^2 u^\mu - 2\varepsilon\underline{b}^\mu_\nu\partial_3 u^\nu - \varepsilon\underline{b}^\nu_\nu\partial_3 u^\mu + \mathcal{O}(\varepsilon^2)\,. \tag{4.36}$$

We assume that shear stress exerted by the air flow and the pressure gradients are the dominating forces which gives

$$U = \frac{\tau\varepsilon}{\mu}, \qquad P = \frac{\rho\nu U}{\varepsilon^2}, \tag{4.37}$$

where τ is the shear stress exerted by the air flow and μ is the dynamic viscosity. Thus, the final equation is given by:

$$0 = -\underline{a}^{\mu\nu}\partial_\nu p - 2\varepsilon\eta\underline{b}^{\mu\nu}\partial_\nu p + \partial_3^2 u^\mu - 2\varepsilon\underline{b}^\mu_\nu\partial_3 u^\nu - \varepsilon\underline{b}^\nu_\nu\partial_3 u^\mu + \mathcal{O}(\varepsilon^2)\,. \tag{4.38}$$

Perpendicular equation

$$u^j\nabla_j u^3 = -\frac{P}{\rho}g^{3i}\partial_i p + \nu U\nabla_i g^{ij}\nabla_j u^3\,. \tag{4.39}$$

Using the scaling factor P from equation (4.37) and expanding the metric terms in the pressure gradient we find the pressure terms to be of order $\mathcal{O}(\varepsilon^{-4})$. Multiplying by ε^4 gives

$$\varepsilon^4 u^j\nabla_j u^3 = -\partial_3 p + \varepsilon^4\nu U\nabla_i g^{ij}\nabla_j u^3\,. \tag{4.40}$$

We now examine the remaining terms up to relevant order:

$$\varepsilon^4 u^j\nabla_j u^3 = \varepsilon^4 u^j\partial_j u^3 + \varepsilon^4 u^j u^k\Gamma^3_{jk} = \mathcal{O}(\varepsilon^3)\,. \tag{4.41}$$

The third component of the first term of the vector Laplacian in equation (4.28) gives

$$\begin{aligned}\varepsilon^4\partial_i g^{ij}\left(\partial_j u^3 + u^l\Gamma^3_{jl}\right) &= \varepsilon^4\left(\partial_\alpha g^{\alpha j} + \partial_3 g^{3j}\right)\left(\partial_j u^3 + u^\beta\Gamma^3_{j\beta} + u^3\Gamma^3_{j3}\right) = \\ &= \varepsilon^4\partial_\alpha g^{\alpha\gamma}\left(\partial_\gamma u^3 + u^\beta\Gamma^3_{\gamma\beta}\right) + \varepsilon^2\partial_3\left(\partial_3 u^3 + u^\beta\Gamma^3_{3\beta}\right) = \mathcal{O}(\varepsilon^2)\,.\end{aligned} \tag{4.42}$$

The expansion of the second term of the vector Laplacian given in the previous section for the tangential momentum equation as given in (4.32) still holds for the perpendicular component.

$$\varepsilon^4\Gamma^i_{mi}g^{mj}\left(\partial_j u^3 + u^l\Gamma^3_{jl}\right) = -\varepsilon^3\underline{b}^\alpha_\alpha\partial_3 u^3 + \mathcal{O}(\varepsilon^4) = \mathcal{O}(\varepsilon^3)\,. \tag{4.43}$$

Finally, the third term:

$$\varepsilon^4\Gamma^3_{mi}g^{ij}\left(\partial_j u^m + u^l\Gamma^m_{jl}\right) = \varepsilon^4\left(\Gamma^3_{m\nu}g^{\nu j} + \Gamma^3_{m3}g^{3j}\right)\left(\partial_j u^m + u^l\Gamma^m_{jl}\right) = \mathcal{O}(\varepsilon^3)\,. \tag{4.44}$$

Plugging in the vector Laplacian in the coordinate frame $\underline{\boldsymbol{x}}_i$, we obtain.

$$0 = \partial_3 p + \mathcal{O}(\varepsilon^2)\,. \tag{4.45}$$

4.2.3 Continuity equation

Under the incompressibility assumption, the continuity equation becomes merely a divergence-free constraint on the velocity field.

$$0 = \nabla_i u^i = \frac{1}{\sqrt{|g|}}\partial_i \sqrt{|g|}u^i = \frac{1}{\sqrt{|g|}}\left(\partial_\alpha \sqrt{|g|}u^\alpha + \partial_3 \sqrt{|g|}u^3\right)\,. \tag{4.46}$$

In order to simplify this equation, we need to compute $\sqrt{\det g}$ where g is the covariant form of the metric. Let us start by noting that the characteristic polynomial p_A of a matrix $A \in M^{n\times n}$ can be written in terms of its trace and determinant according to Vieta's formulas

$$p_A(\lambda) = (-\lambda)^n + (-\lambda)^{n-1}\operatorname{tr}A + c_{n-2}\lambda^{n-2}\cdots + c_1\lambda + \det A\,, \tag{4.47}$$

where $c_1, \dots, c_{n-2}$ are other unspecified coefficients dependent on A. Using this relation, we can express the determinant of a perturbed identity matrix by

$$\det(I - \varepsilon A) = (-\varepsilon)^n p_A(\varepsilon^{-1}) = 1 - \varepsilon \operatorname{tr}A + \mathcal{O}(\varepsilon^2)\,. \tag{4.48}$$

Applying this relation to simplify the determinant of the metric gives

$$\sqrt{\det g} = \varepsilon\sqrt{\det\underline{a}}\sqrt{\det(I - 2\varepsilon\eta\underline{a}^{-1}\underline{b})} + \mathcal{O}(\varepsilon^3) = \varepsilon\sqrt{\det\underline{a}}(1 - \varepsilon\,\eta\,\underline{H}) + \mathcal{O}(\varepsilon^3)\,. \tag{4.49}$$

The determinant of the metric g depends on the perpendicular η component in a simple linear fashion allowing us to integrate equation (4.46) analytically over the film. For clarity, we discuss the tangential and normal terms in expression (4.46) individually. On the one hand, evaluating the integral of the tangential components over the interval $[\zeta, \zeta+\xi]$ gives

$$
\begin{aligned}
\frac{-1}{\varepsilon\sqrt{|\underline{a}|}}\int_{\zeta}^{\zeta+\xi} \partial_\alpha \sqrt{|g|}u^\alpha \,\mathrm{d}\eta &= \frac{-1}{\varepsilon\sqrt{|\underline{a}|}}\left[\partial_\alpha \int_{\zeta}^{\zeta+\xi} \sqrt{|g|}u^\alpha \,\mathrm{d}\eta - \sqrt{|\tilde{g}|}\tilde{u}^\alpha \partial_\alpha(\zeta+\xi) + \sqrt{|\bar{g}|}\bar{u}^\alpha \partial_\alpha \zeta\right] \\
&= -\frac{1}{\sqrt{|\underline{a}|}}\partial_\alpha \sqrt{|\underline{a}|}\int_{\zeta}^{\zeta+\xi} (1-\varepsilon \underline{H}\eta)u^\alpha \,\mathrm{d}\eta + \\
&\quad + (1-\varepsilon(\zeta+\xi)\underline{H})\tilde{u}^\alpha \partial_\alpha(\zeta+\xi) - (1-\varepsilon\zeta\underline{H})\bar{u}^\alpha \partial_\alpha \zeta + \mathcal{O}(\varepsilon^2)\,.
\end{aligned}
\tag{4.50}
$$

Let $Q^\alpha := \int_{\zeta}^{\zeta+\xi}(1-\varepsilon\underline{H}\eta)u^\alpha \,\mathrm{d}\eta$ which can be interpreted as the mass flux. This substitution allows us to rewrite the expression in terms of the covariant derivative on the substrate $\underline{\nabla}$

$$
\begin{aligned}
\frac{-1}{\varepsilon\sqrt{|\underline{a}|}}\int_{\zeta}^{\zeta+\xi} \partial_\alpha \sqrt{|g|}u^\alpha \,\mathrm{d}\eta = -\underline{\nabla}_\alpha Q^\alpha + (1-\varepsilon(\zeta+\xi)\underline{H})\tilde{u}^\alpha \partial_\alpha(\zeta+\xi) - \\
- (1-\varepsilon\zeta\underline{H})\bar{u}^\alpha \partial_\alpha \zeta + \mathcal{O}(\varepsilon^2)\,.
\end{aligned}
\tag{4.51}
$$

On the other hand, the perpendicular component integrated over the film reads

$$
\frac{1}{\varepsilon\sqrt{|\underline{a}|}}\int_{\zeta}^{\zeta+\xi} \partial_3 \sqrt{|g|}u^3 \,\mathrm{d}\eta = (1-\varepsilon(\zeta+\xi)\underline{H})\tilde{u}^3 - (1-\varepsilon\zeta\underline{H})\bar{u}^3\,,
\tag{4.52}
$$

which finally gives

$$
(1-\varepsilon\underline{H}(\zeta+\xi))\big(\tilde{u}^3 - \tilde{u}^\alpha \partial_\alpha(\zeta+\xi)\big) - (1-\varepsilon\underline{H}\zeta)\big(\bar{u}^3 - \bar{u}^\alpha \partial_\alpha \zeta\big) = -\underline{\nabla}_\alpha Q^\alpha\,.
\tag{4.53}
$$

The expressions on the left-hand side are subject to the boundary conditions which we discuss in the next section.

4.2.4 Boundary conditions

The boundary conditions close the system and incorporate the interaction between the ice layer and the air flow. Firstly, we discuss the boundary conditions imposed on the tangential momentum equation, and subsequently, we address the normal direction.

Tangential momentum equation

Two boundary conditions are imposed: a no-slip constraint at the ice-water surface and a continuity of surface stress at the free surface. The no-slip condition at the interface represented by $\overline{\mathscr{M}}$ is given by

$$0 = \langle \bar{\boldsymbol{u}} | \bar{\boldsymbol{x}}_\alpha \rangle \,. \tag{4.54}$$

Plugging in the basis vectors, we can simplify the previous expression to give

$$\langle \bar{\boldsymbol{u}} | \bar{\boldsymbol{x}}_\alpha \rangle = \bar{u}^i \langle \boldsymbol{x}_i | \bar{\boldsymbol{x}}_\alpha \rangle = \bar{u}^\beta \langle \boldsymbol{x}_\beta | \bar{\boldsymbol{x}}_\alpha \rangle + \bar{u}^3 \varepsilon \langle \underline{\boldsymbol{n}} | \bar{\boldsymbol{x}}_\alpha \rangle = \bar{u}^\beta \bar{a}_{\alpha\beta} + \mathscr{O}(\varepsilon^2) \,. \tag{4.55}$$

Multiplying by $\bar{a}^{\alpha\gamma}$ yields

$$0 = \bar{u}^\gamma + \mathscr{O}(\varepsilon^2) \,. \tag{4.56}$$

A continuity of surface stress constraint is imposed at the free surface. This condition transfers stress from the air flow to the water film and causes the *pushing* of the water film downstream. We follow the work by Myers et al. (2002b) and ignore momentum transfer from the droplet phase to the film. Williams et al. (2012) investigated the effect of momentum transfer across the interface for a constant impact angle and cylindrical symmetry but does not consider more general scenarios. Since we focus on more complex geometries, we proceed with the assumptions of Myers et al. (2002b). The boundary condition in coordinate-free form then reads

$$\tau_{\mathrm{a}} \left(\tilde{\boldsymbol{x}}_\mu \otimes \tilde{\boldsymbol{n}} \right) = \tilde{\tau} \left(\tilde{\boldsymbol{x}}_\mu \otimes \tilde{\boldsymbol{n}} \right) , \tag{4.57}$$

where τ_{a} is the deviatoric stress tensor of the air and $\tilde{\tau}$ is the deviatoric stress tensor of the water at the interface. In general, the deviatoric stress tensor is defined as the symmetric gradient of the velocity field:

$$\tau_{ij} = \mu \left(\nabla_i u_j + \nabla_j u_i \right) , \tag{4.58}$$

where μ is the dynamic viscosity.

We now compute the tangential shear stress component of $\tilde{\tau}$ in coordinate form. Similarly to equation (4.27), we will find a common factor of ε^{-1} in the normal component. Therefore, we multiply preemptively by ε in order to obtain a leading order of ε^0. The shear stress tangential to the free surface $\tilde{\mathscr{M}}$ in the water film is then:

$$\tilde{\tau}_{ij} (\mathrm{d}x^i \otimes \mathrm{d}x^j)(\tilde{\boldsymbol{x}}_\alpha \otimes \varepsilon \tilde{\boldsymbol{n}}) \,. \tag{4.59}$$

In order to compute the shear stress in coordinate form the vectors $\tilde{\boldsymbol{n}}$ and $\tilde{\boldsymbol{x}}_\alpha$ are required in the substrate coordinate system (4.6).

$$\varepsilon\tilde{\boldsymbol{n}} = \varepsilon\underline{\boldsymbol{n}} + \mathcal{O}(\varepsilon^2) = \boldsymbol{x}_3 + \mathcal{O}(\varepsilon^2)\,, \tag{4.60}$$

$$\tilde{\boldsymbol{x}}_\mu = \boldsymbol{x}_\mu + (\zeta + \xi)_\mu \boldsymbol{x}_3\,. \tag{4.61}$$

Applying the dual basis elements of $T\tilde{\mathcal{M}}$ and the covector of the normal $\tilde{\boldsymbol{n}}$ to the basis vectors of the substrate coordinate system (4.6) gives

$$\mathrm{d}x^i\,\varepsilon\tilde{\boldsymbol{n}} = \delta^i_3 + \mathcal{O}(\varepsilon^2)\,, \tag{4.62a}$$

$$\mathrm{d}x^j\,\tilde{\boldsymbol{x}}_\mu = \delta^j_\mu + (\zeta + \xi)_\mu \delta^j_3\,. \tag{4.62b}$$

These factors can now be used to express the shear stress tangent to the water-air interface in substrate coordinates. Plugging equation (4.62) into (4.59) gives:

$$\begin{aligned}\tilde{\tau}_{ij}\,\mathrm{d}x^i\,\tilde{\boldsymbol{x}}_\mu\,\mathrm{d}x^j\,\varepsilon\tilde{\boldsymbol{n}} &= \tau_{ij}\delta^i_3\left(\delta^j_\mu + (\zeta+\xi)_\mu\delta^j_3\right) + \mathcal{O}(\varepsilon^2) = \\ &= \tau_{3\mu} + (\zeta+\xi)_\mu \tau_{33} + \mathcal{O}(\varepsilon^2)\,.\end{aligned} \tag{4.63}$$

Therefore, the only relevant components of the deviatoric stress tensor are

$$\frac{1}{\mu}\tau_{33} = 2\nabla_3 u_3 = 2\partial_3 u_3 = 2\varepsilon^2\partial_3 u^3 = \mathcal{O}(\varepsilon^2)\,, \tag{4.64}$$

and

$$\begin{aligned}\frac{1}{\mu}\tau_{\alpha 3} &= \nabla_3 u_\alpha + \nabla_\alpha u_3 = \partial_3 u_\alpha + \partial_\alpha u_3 - 2u_i\Gamma^i_{\alpha 3} = \\ &= \partial_3 g_{\alpha i} u^i + \partial_\alpha g_{3i} u^i - 2u_\beta \Gamma^\beta_{\alpha 3} = \partial_3 g_{\alpha\beta} u^\beta + 2u_\beta \varepsilon \underline{b}^\beta_\alpha + \mathcal{O}(\varepsilon^2) = \\ &= \partial_3\left(\underline{a}_{\alpha\beta} - 2\varepsilon\eta \underline{b}_{\alpha\beta} u^\beta\right) + 2u^\beta\varepsilon\underline{b}_{\alpha\beta} + \mathcal{O}(\varepsilon^2) = g_{\alpha\beta}\partial_3 u^\beta + \mathcal{O}(\varepsilon^2)\,.\end{aligned} \tag{4.65}$$

Plugging expressions (4.64) and (4.65) into equation (4.63) we obtain

$$\tilde{\tau}_{ij}\,\mathrm{d}x^i\,\tilde{\boldsymbol{x}}_\mu\,\mathrm{d}x^j\,\varepsilon\tilde{\boldsymbol{n}} = g_{\mu\nu}\partial_3 u^\nu + \mathcal{O}(\varepsilon^2)\,. \tag{4.66}$$

Finally, using expression (4.66) on both sides of equation (4.57) gives a simplified form of the continuity of surface stress condition which is given by

$$\partial_3 u^{\mu} = g^{\mu\nu}\tau_{\mathrm{a}\nu 3} + \mathcal{O}(\varepsilon^2)\,. \tag{4.67}$$

Perpendicular momentum equation

The surface tension of the free surface exerts a pressure into the thin film which is governed by the Young-Laplace equation (Frankel, 2011)

$$\Delta p = -2\sigma\tilde{H}\,, \tag{4.68}$$

where σ is the surface tension and $\tilde{H}$ the mean curvature at the free surface. The mean curvature is defined as the trace of the second fundamental form $\tilde{b}$. Taking the trace of equation (4.25) gives

$$\tilde{H} = \underline{b}_{\alpha}^{\alpha} + \varepsilon(\zeta+\xi)\underline{b}_{\alpha}^{\beta}\underline{b}_{\beta}^{\alpha} + \varepsilon\underline{\nabla}_{\alpha}\underline{a}^{\alpha\beta}(\zeta+\xi)_{\beta} + \mathcal{O}(\varepsilon^2)\,. \tag{4.69}$$

This result is one of the significant differences of this derivation compared to a thin film on a flat surface. The first two terms take into account the curvature of the substrate. Therefore, it is possible that the film evolution is driven by surface tension even though the film height is constant. A result like this is not possible with the flat substrate equations.

Finally, we arrive at the normal stress boundary condition at the free surface:

$$\tilde{p} = p_{\mathrm{a}} - 2\sigma\tilde{H}\,. \tag{4.70}$$

Continuity equation

Mass is conserved across fluid interfaces. Considering two fluids A and B separated by an interface I the continuity of mass constraint becomes

$$\rho_A\langle \boldsymbol{n}_{\mathrm{I}}|\boldsymbol{v}_A - \boldsymbol{v}_{\mathrm{I}}\rangle = \rho_B\langle \boldsymbol{n}_{\mathrm{I}}|\boldsymbol{v}_B - \boldsymbol{v}_{\mathrm{I}}\rangle\,, \tag{4.71}$$

where $\boldsymbol{n}_{\mathrm{I}}$ is the normal of the interface, $\boldsymbol{v}_{\mathrm{I}}$ the velocity of the interface, ρ the density and $\boldsymbol{v}$ the material velocity. This boundary condition is applied at both the ice-water and the water-air boundaries. The ice-water interface velocity is $\partial_t\bar{\boldsymbol{x}}$ which simplifies to

$$\partial_t\bar{\boldsymbol{x}} = \varepsilon\,\underline{\boldsymbol{n}}\,\partial_t\zeta\,. \tag{4.72}$$

Due to the no-slip condition given in equation (4.56), the tangential components of the water velocity vanish and the continuity of mass equation becomes

$$\bar{u}^3 = \left(1 - \frac{\rho_\mathrm{i}}{\rho}\right)\partial_t \zeta + \mathcal{O}(\varepsilon^2)\,. \tag{4.73}$$

At the free surface $\tilde{\mathscr{M}}$, the continuity of mass condition is given by

$$\alpha_\mathrm{d}\rho_\mathrm{d}\langle \tilde{\boldsymbol{n}} | \boldsymbol{v}_\mathrm{a}\rangle - \varepsilon\langle \tilde{\boldsymbol{n}} | \underline{\boldsymbol{n}}\,\partial_t(\zeta + \xi)\rangle = \rho\langle \tilde{\boldsymbol{n}} | \boldsymbol{u} - \varepsilon\,\underline{\boldsymbol{n}}\,\partial_t(\zeta + \xi)\rangle\,, \tag{4.74}$$

where $\alpha_\mathrm{d}\rho_\mathrm{d}$ is the liquid water content in the air and $\boldsymbol{v}_\mathrm{a}$ is the velocity of the water droplets in the air phase. Rearranged to solve for $\tilde{u}^3$ the equation reads.

$$\tilde{u}^3 = \left(1 - \alpha_\mathrm{d}\frac{\rho_\mathrm{d}}{\rho}\right)\partial_t(\zeta + \xi) + \tilde{u}^\alpha(\zeta + \xi)_\alpha + \alpha_\mathrm{d}\frac{\rho_\mathrm{d}}{\rho\varepsilon}\langle \tilde{\boldsymbol{n}} | \boldsymbol{v}_\mathrm{a}\rangle + \mathcal{O}(\varepsilon^2)\,. \tag{4.75}$$

Plugging the boundary conditions (4.73) and (4.75) into the continuity of mass equation (4.53)

$$\begin{aligned} &\left(1 - \alpha_\mathrm{d}\frac{\rho_\mathrm{d}}{\rho}\right)\partial_t\xi + (1 + \varepsilon\underline{H}(\zeta + \xi))\underline{\nabla}_\alpha Q^\alpha = \\ &\qquad = \left[(1 + \varepsilon\underline{H}\xi)\left(1 - \frac{\rho_\mathrm{i}}{\rho}\right) - \left(1 - \alpha_\mathrm{d}\frac{\rho_\mathrm{d}}{\rho}\right)\right]\partial_t\zeta - \alpha_\mathrm{d}\frac{\rho_\mathrm{d}}{\rho\varepsilon}\langle \tilde{\boldsymbol{n}} | \boldsymbol{v}_\mathrm{a}\rangle + \mathcal{O}(\varepsilon^2)\,. \end{aligned} \tag{4.76}$$

This is the final governing equation for the water film which is used for the remainder of this chapter. Finally, we need to find expressions for the fluxes Q^α, which is discussed in the next section.

4.2.5 Integration of the governing equations

We can integrate the momentum equations analytically thereby reducing the governing set to one equation. Under the thin film assumption, the solution is well approximated by a linear expansion in ε:

$$u^\mu = u^\mu_{(0)} + \varepsilon\, u^\mu_{(1)} + \mathcal{O}(\varepsilon^2)\,, \tag{4.77a}$$

$$p = p_{(0)} + \varepsilon\, p_{(1)} + \mathcal{O}(\varepsilon^2)\,. \tag{4.77b}$$

We can plug these expansions into the governing equations (4.38) and (4.45) and apply the boundary conditions (4.56), (4.67) and (4.70). Collecting terms of varying order in ε and listing them individually simplifies the derivation.

Terms of order ε^0

Firstly, let us consider terms of constant order in ε. The differential equations are given by:

$$\partial_3^2 u^\mu_{(0)} = \underline{a}^{\mu\nu}\partial_\nu p_{(0)}\,, \tag{4.78a}$$

$$\partial_3 p_{(0)} = 0\,, \tag{4.78b}$$

$$\tag{4.78c}$$

subject to the following boundary conditions:

$$\tilde{p}_{(0)} = p_\mathrm{a} - \sigma \underline{H}\,, \tag{4.79a}$$

$$\partial_3 \tilde{u}^\mu_{(0)} = g^{\mu\nu}\tau_{\mathrm{a}\mu 3}\,, \tag{4.79b}$$

$$\bar{u}^\mu_{(0)} = 0\,. \tag{4.79c}$$

Note that equations (4.79b) and (4.79c) imply a shear stress singularity as $\xi \to 0$. This is a possible scenario in icing applications and needs to be addressed, e.g. in cold conditions when rime ice is building up. Diez et al. (2001) have found that the introduction of a precursor film gives good numerical results and is based on experimental evidence (Hansen and Toong, 1971; Ludviksson and Lightfoot, 1968). We also implement the precursor framework to avoid the shear stress singularity.

Under the precursor assumption $\xi > 0$, we can integrate the governing equations. The constant order solution is given by:

$$u^\mu_{(0)} = g^{\mu\nu}\tau_{\mathrm{a}\nu 3}(\eta - \zeta) - \underline{a}^{\mu\nu}(\partial_\nu p_{(0)})\left[(\zeta + \xi)(\eta - \zeta) - \frac{\eta^2 - \zeta^2}{2}\right], \tag{4.80a}$$

$$p_{(0)} = p_\mathrm{a} - \sigma \underline{H}\,. \tag{4.80b}$$

Terms of order ε^1

The linear order equations are given by

$$\begin{aligned} \partial_3^2 u^\mu_{(1)} &= \underline{a}^{\mu\nu}\partial_\nu p_{(1)} + 2\eta \underline{b}^{\mu\nu}\partial_\nu p_{(0)} + 2\underline{b}^\mu_\nu \partial_3 u^\nu_{(0)} + \underline{b}^\nu_\nu \partial_3 u^\mu_{(0)}\,, \\ \partial_3 p_{(1)} &= 0\,, \end{aligned} \tag{4.81}$$

subject to the boundary conditions:

$$\begin{aligned} \tilde{p}_{(1)} &= -\sigma\left[(\zeta+\xi)\underline{b}_{\alpha}^{\beta}\underline{b}_{\beta}^{\alpha} + \underline{\nabla}_{\alpha}\underline{a}^{\alpha\beta}(\zeta+\xi)_{\beta}\right], \\ \partial_3 \tilde{u}^{\mu}_{(1)} &= 0, \\ \bar{u}^{\mu}_{(1)} &= 0. \end{aligned} \tag{4.82}$$

Integrating the equations gives

$$\begin{aligned} u^{\mu}_{(1)} = {} & \underline{a}^{\mu\nu}\partial_{\nu}p_{(1)}\frac{\eta-\zeta}{2}(\zeta-\eta+2\xi)+ \\ & +\underline{b}^{\mu\nu}\partial_{\nu}p_{(0)}\frac{\eta-\zeta}{3}\left(2\zeta^2-\zeta\eta-\eta^2+6\zeta\xi+3\xi^2\right)+ \\ & +\underline{b}^{\mu}_{\nu}\frac{\zeta-\eta}{3}\left[\left(3\xi(\zeta-\eta)+(\zeta-\eta)^2+3\xi^2\right)\underline{a}^{\nu\lambda}\partial_{\lambda}p_{(0)}-3\tau_0^{\nu}(\zeta-\eta+2\xi)\right]+ \\ & +\underline{H}\frac{\zeta-\eta}{6}\left[\left(3\xi(\zeta-\eta)+(\zeta-\eta)^2+3\xi^2\right)\underline{a}^{\mu\nu}\partial_{\nu}p_{(0)}-3\tau_0^{\mu}(\zeta-\eta+2\xi)\right]+ \\ & +{\tau_{\mathrm{a}(1)}}^{\mu}(\eta-\zeta), \\ p_{(1)} = {} & -\sigma\left[(\zeta+\xi)\underline{b}_{\alpha}^{\beta}\underline{b}_{\beta}^{\alpha}+\underline{\nabla}_{\alpha}\underline{a}^{\alpha\beta}(\zeta+\xi)_{\beta}\right], \end{aligned} \tag{4.83}$$

Mass fluxes

Using the approximations from the previous section, we can rewrite the mass fluxes giving

$$\begin{aligned} Q^{\mu} = {} & \int\limits_{\zeta}^{\zeta+\xi}(1-\varepsilon\eta\underline{H})u^{\mu}\,\mathrm{d}\eta = \int\limits_{\zeta}^{\zeta+\xi}(1-\varepsilon\eta\underline{H})u^{\mu}_{(0)}+\varepsilon u^{\mu}_{(1)}\,\mathrm{d}\eta+\mathcal{O}(\varepsilon^2)= \\ = {} & \frac{\xi^2}{2}\left(\tau^{\mu}_{(0)}+\epsilon\tau^{\mu}_{(1)}\right)-\frac{\xi^3}{3}\underline{a}^{\mu\nu}\left(\partial_{\nu}p_{(0)}+\epsilon\partial_{\nu}p_{(1)}\right)+ \\ & +\varepsilon\left[\frac{1}{3}\underline{H}\xi^3(\zeta+\xi)\partial_{\nu}p_{(0)}\underline{a}^{\mu\nu}-\frac{1}{6}\xi^3(4\zeta+\xi)\partial_{\nu}p_{(0)}\underline{b}^{\nu\mu}-\right. \\ & \left.-\frac{1}{6}\underline{H}\xi^2(3\zeta+4\xi)\tau^{\mu}_{(0)}-\frac{2}{3}\xi^3\tau^{\nu}_{(0)}\underline{b}^{\mu}_{\nu}\right]+\mathcal{O}(\varepsilon^2). \end{aligned} \tag{4.84}$$

Equation (4.76) and (4.84) combine to give a fourth order non-linear PDE which governs the water flow. Three aspects differentiate this model from others published in the literature. Firstly, no assumption is made about the parameterisation of the substrate. Secondly, $\mathcal{O}(\varepsilon)$ terms are fully included and, lastly, the equations allow the existence of another layer which is defined by ζ such as an ice layer.

Our system reduces naturally to the Myers et al. (2002a) model by assuming $\underline{b}$ to be diagonal and truncating $\mathcal{O}(\varepsilon)$ terms. Moreover, we can recover the governing equations of Thiffeault and Kamhawi (2006) by setting $\zeta = 0$ and $\tau = 0$.

4.2.6 Summary of the physical processes in the water film

Before we turn to the numerical solution of the governing equations, we briefly summarise and give some physical intuition for the previous derivation.

One of the foundational assumptions was that the film remains thin. In other words, we neglect second and higher orders of ε i.e. the ratio of the film height over the film extent. Moreover, we assumed that inertial forces are negligible or that $\mathrm{Re}\,\varepsilon^2$ remains small. These assumptions are common in the ice accretion literature (Myers et al., 2002a; Bourgault et al., 2000a).

The boundary conditions between the water and the ice, and the water and surrounding air drive the dynamics of the film. The motion of the ice-water interface is assumed to be known. In section 4.7, we will derive a governing differential equation for the interface dynamics based on the Stefan approach.

We impose a continuity of stress condition onto the water-air interface. This introduces three driving forces: surface tension, air pressure gradients and air shear stress. The air shear stress is the main driving factor when the film is very thin as its contribution scales with the square of the film height whereas all other forces scale with the cube (see equation (4.84)). The surface tension and air pressure gradient forces arise from to the continuity of normal stress. The forces due to surface tension are proportional to the mean curvature of the water-air interface. Contrary to flows on a flat plate where the curvature is approximated by the second derivative, it is important to also take into account the curvature of the underlying substrate. The combined mean curvature is given in equation (4.69).

These assumptions and boundary conditions make it is possible to integrate the expanded Navier-Stokes equations over the film height to give a significantly simplified governing equation for the dynamic of the water film.

4.3 Numerical methods for the water film

The PDE for glaze ice, discussed in the previous section, exhibits features such as non-linearities and high order derivatives which pose challenges to numerical solvers.

Each term contributes to the governing equations in a different way. We decompose the flux into two parts: an explicit Q_{exp} and implicit part Q_{imp}. The explicit part contains all terms with no derivative of ξ or ζ and the implicit flux is made up of the remainder. Consequently, the explicit and implicit portions of the fluxes are given by

$$\begin{aligned} Q^{\mu}_{\text{exp}} &= \frac{\xi^2}{2}\left(\tau^{\mu}_{(0)} + \epsilon\tau^{\mu}_{(1)}\right) + \varepsilon\left[-\frac{1}{6}\underline{H}\xi^2(3\zeta+4\xi)\tau^{\mu}_{(0)} - \frac{2}{3}\xi^3\tau^{\nu}_{(0)}\underline{b}^{\mu}_{\nu}\right] + \mathcal{O}(\varepsilon^2)\,, \\ Q^{\mu}_{\text{imp}} &= -\frac{\xi^3}{3}\underline{a}^{\mu\nu}\partial_{\nu}p_{(0)} + \varepsilon\left[\frac{1}{3}\underline{H}\xi^3(\zeta+\xi)\partial_{\nu}p_{(0)}\underline{a}^{\mu\nu} - \frac{1}{6}\xi^3(4\zeta+\xi)\partial_{\nu}p_{(0)}\underline{b}^{\nu\mu}\right] + \mathcal{O}(\varepsilon^2)\,. \end{aligned} \tag{4.85}$$

The terms of the flux containing τ model the shear stress. The quadratic dependency on the state variable ξ resembles the flux of the inviscid Bateman-Burgers equation and is capable of introducing discontinuities into the solution. Terms containing p arise from the surface tension forces and have derivates in them. These expressions add significant stiffness to the problem and require implicit solvers. We use a splitting methodology to employ the most suitable solver for the individual fluxes:

$$\text{Implicit portion:}\quad \left.\begin{aligned} &\partial_t\xi + \nabla\cdot Q_{\text{imp}} = 0 \\ &\xi_0 = \xi^n \end{aligned}\right\} \rightsquigarrow \xi^{n+\frac{1}{3}}\,, \tag{4.86a}$$

$$\text{Explicit portion:}\quad \left.\begin{aligned} &\partial_t\xi + \nabla\cdot Q_{\text{exp}} = 0 \\ &\xi_0 = \xi^{n+\frac{1}{3}} \end{aligned}\right\} \rightsquigarrow \xi^{n+\frac{2}{3}}\,, \tag{4.86b}$$

$$\text{Source portion:}\quad \left.\begin{aligned} &\frac{\mathrm{d}}{\mathrm{d}t}\xi = S \\ &\xi_0 = \xi^{n+\frac{2}{\xi}3} \end{aligned}\right\} \rightsquigarrow \xi^{n+1}\,. \tag{4.86c}$$

4.3.1 Explicit portion

The explicit portion is solved using a high-resolution method. Contrary to air and droplet flow, the Riemann problem for the explicit portion of the flux is not solved efficiently. Therefore, we fall back to centred methods. In this work, we use the Slope Limited Centred flux method(SLIC) as presented in Toro (2009) with a superbee-type slope limiter. The superbee-type slope limiter favours a higher order of reconstruction which gives higher accuracy at the cost potentially spurious oscillation. We have not found any significant oscillations which stem from the flux method and therefore employ the higher accuracy superbee limiter. This part of the splitting step tends to dominate the time step restriction. But we have not found the explicit nature of this scheme to be restrictive to computational performance for icing applications.

4.3.2 Implicit portion

The implicit portion contains derivatives up to fourth order and non-linearities making this a challenge to solve numerically. Myers et al. (2002b) published results solving this system explicitly. However, they found that the time step restriction imposed by the high derivatives is too severe and concluded that an implicit methodology is better-suited (Myers et al., 2002a). Due to the non-linear terms, the discretisation cannot be reduced to a system of linear equations. Myers et al. (2002a) circumvent this restriction by only treating the linear terms implicitly and approximate the non-linear quantities at $t + \Delta t$ by their value at t. We follow their strategy and employ an implicit methodology. However, we also discretise non-linear terms implicitly.

For the time discretisation, a Crank Nicolson scheme is used, which reads

$$\frac{\xi^{n+1} - \xi^{n}}{\Delta t} + \frac{1}{2}\left(\nabla \cdot Q_{\text{imp}}\Big|^{n} + \nabla \cdot Q_{\text{imp}}\Big|^{n+1} \right) = 0\,. \tag{4.87}$$

The spatial discretisation of the fourth order derivative requires a comparatively large 5-point stencil in 1D. The computer algebra system *SymPy* developed by Meurer et al. (2017) is used to aid the error prone implementations of high order finite difference approximations. The software can automatically convert symbolic expressions containing partial derivatives into finite difference representations. This method of lines approach requires finding the root of equation (4.87) for every grid cell where the spatial differences depend on the neighbouring cells. The *Trust-Region Method for Non-linear Equations* is one of the most widely used and practical root finding methods (Nocedal and Wright, 1999, p. 299). An approximate root is found using the *Dogleg* method (Nocedal and Wright, 1999, p. 300). Subsequently, the solution is checked against the actual problem and the trust region is adjusted based on the quality of the approximation. This process is done iteratively until the root is found. The method is based on the Newton-Raphson method and requires the Jacobian of the system. Due to the fourth derivative, the spatial discretisation requires a relatively wide stencil making the derivation of the Jacobian cumbersome and error-prone. *SymPy* is used again to compute the Jacobian automatically.

We accept an approximation if the absolute residual (left hand side of equation (4.87)) is less than 10^{-20} or the relative residual less than 100ε where ε is machine precision. We have found that the root finder converges within a few iterations. Given a time step from the explicit solver, an acceptable approximation to the root is typically found in less than 10 iterations.

4.4 Validation tests for the water film

This section presents various tests to assess the correct implementation of the numerical solvers which were introduced in section 4.3. Myers et al. (2002b) devised validation cases relevant to aircraft ice accretion. We start by studying the water flow only. The setup is illustrated in figure 4.3. The first test assesses the capability of resolving capillary ridges under shear stress and the second introduces gravity as a competing driving force.

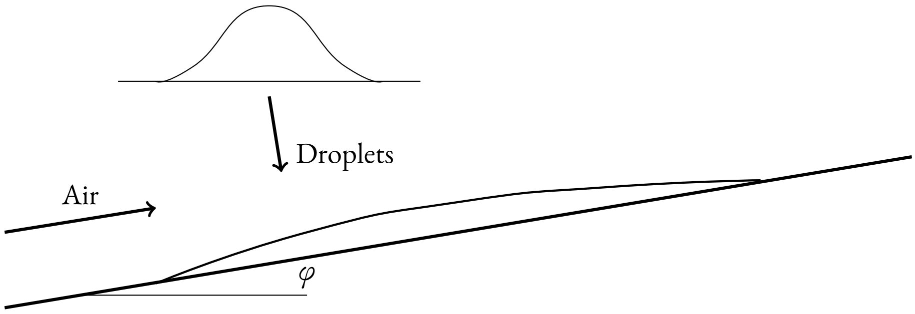

Figure 4.3: Illustration of the setup of the flat plate validation case. The incoming droplet distribution is bell shaped. Air flow parallel to the flat exerts a shear stress onto the water film. The plate is inclined by an angle φ and gravity acts downwards.

Variable	Symbol	Value	
Surface tension of water-air interface	σ	0.727	Pa
Density of water	ρ_w	1000	$\mathrm{kg\,m^{-3}}$
Density of ice	ρ_i	898	$\mathrm{kg\,m^{-3}}$
Dynamic viscosity of water	μ_w	1	mPa s
Latent heat	L_f	334.4	$\mathrm{kJ\,kg^{-1}}$
Thermal conductivity of water	k_w	0.571	$\mathrm{W\,m^{-1}\,K^{-1}}$
Thermal conductivity of ice	k_i	2.18	$\mathrm{W\,m^{-1}\,K^{-1}}$
Specific heat capacity of water	c_w	4192	$\mathrm{J\,kg^{-1}\,K^{-1}}$
Magnitude of gravitational acceleration	$\|\|\boldsymbol{g}\|\|$	10	$\mathrm{m\,s^{-2}}$

Table 4.1: Physical constants used for the validation of the thin water film and ice solver.

The values of the physical parameters that were used in the simulation are tabulated in 4.1. In all of the test cases, the water droplet distribution on the surface follows a Gaussian profile centred around the origin given by

$$\rho_\mathrm{d}\langle v_\mathrm{d}|\underline{\boldsymbol{n}}\rangle = \beta_0 \exp(-\lambda x^2)\,, \tag{4.88}$$

where $\beta_0 = 5 \times 10^{-2}\,\mathrm{kg\,m^{-2}\,s^{-1}}$ and $\lambda = 460\,\mathrm{m^{-2}}$. A precursor film of height $5\,\mu\mathrm{m}$ is introduced to avoid a shear stress singularity at the beginning of the simulation.

Flat plate

The first test case simulates impinging droplets on a flat plate driven by free surface shear. A constant stress of $\tau = 0.5\,\mathrm{Pa}$ is introduced. Balancing the surface tension and shear stress forces, this type of flow typically features a capillary ridge (Kataoka and Troian, 1997). The equations are spatially discretised on a computational grid of 700 cells.

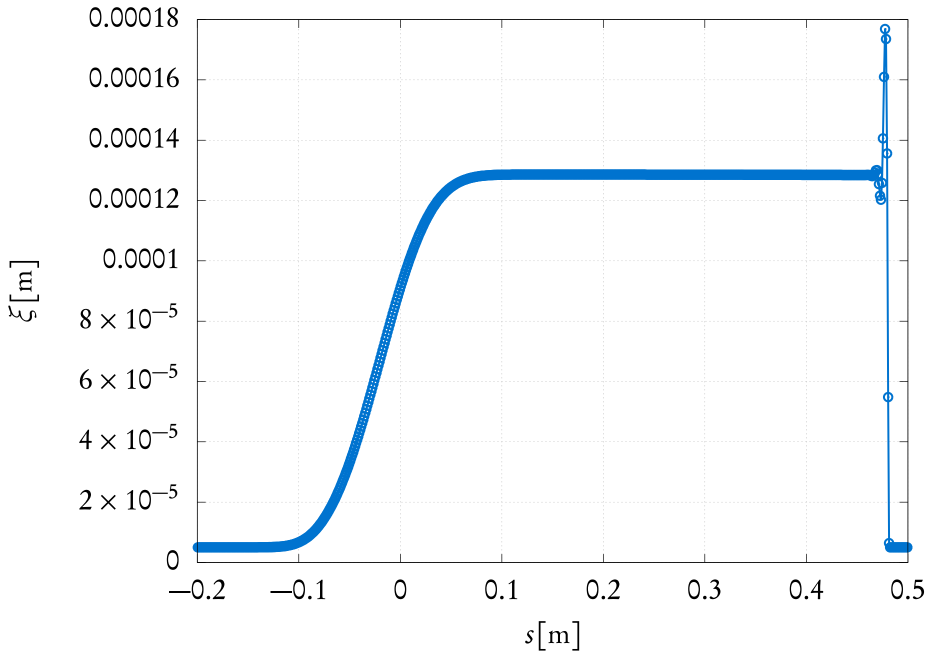

Figure 4.4: The water height is plotted over the spatial extent of the film for $T = 15\,\mathrm{s}$. After initial growth of the film a quasi-steady state is reached. The shear stress flux increases with ξ^2 balancing the incoming water droplets when the equilibrium height is reached. A capillary ridge is formed at the contact line as expected for this type of flow.

The results of this test are illustrated in figure 4.4. Initially, water accumulates on the surface and the film height increases producing a Gaussian profile. As ξ grows the shear stress flux increases as well pushing the film to the right. Eventually, the shear stress flux and the water droplets flux balance and an equilibrium height is attained. The shear stress flux is a Burger-like flux introducing a discontinuity at the contact line which is countered by the surface tension forces producing a capillary ridge. The bulk height, as well as the ridge height, agrees well with the validation results by Myers et al. (2002b).

Inclined flat plate

The second test case introduces gravity as a competing driving force to the shear stress. The derivation of the thin film model from section 4.2 did not include gravity terms since an expression for the gravity flux was already found by Thiffeault and Kamhawi (2006). The gravity flux is given by

$$Q_{\mathrm{g}}^{\mu} = \frac{\xi^3}{3}\left((1-\varepsilon \underline{H}\xi)g^{\mu} - \varepsilon \underline{b}_{\nu}^{\mu} g^{\nu}\xi + \varepsilon g_3 \underline{a}^{\mu\nu}\partial_{\nu}\xi\right), \tag{4.89}$$

where g is the gravity vector and not to be confused with the metric. The flat plate is inclined at an angle of 20°. The same grid spacing as in the previous test case is used giving a computational domain of 600 cells.

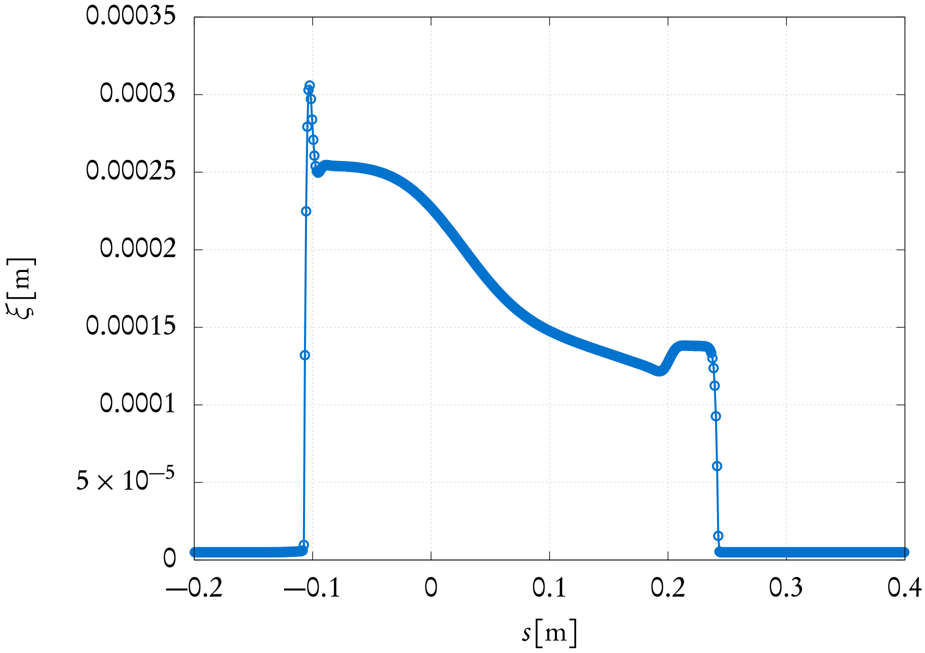

Figure 4.5: A thin water film driven by surface shear stress and gravity on an inclined flat plate. A flux of incoming water droplets initially increases the film height. The shear stress flux pushes the film along the positive coordinate direction as the flux grows with ξ^2. After the film grows even further the effects of gravity are visible which pulls the film into the opposite direction. Eventually, an equilibrium is reached resulting in a quasi-steady state.

Figure 4.5 presents the results of this test case. A quasi-steady state, similar to the previous simulation, is reached. This time the shear stress is pushing the film along the positive substrate direction and gravity is forcing in the opposite direction. Again, we observe good overall qualitative agreement with the results published by Myers et al. (2002a).

4.5 Importance of $\mathcal{O}(\varepsilon)$ terms

In this section, we study the importance of first-order terms of the thin film approximation. Myers et al. (2002a) neglected some of the linear terms and only retained ε-terms appearing in the free surface curvature expression. In section 4.2, we have generalised the thin film model of Myers et al. (2002a) to consistently include terms of order ε. We present a test case demonstrating the advantages of retaining linear terms in the thin film approximation.

Evans et al. (2004) studied the coating flow of a rotating cylinder. As part of their study, they presented results for a water drop forming on the underside of a static horizontal cylinder. The existence of an analytic expression for the water height makes this an ideal test case to demonstrate the contribution of first-order terms. We continue by introducing the case of a non-rotating cylinder as illustrated in figure 4.6.

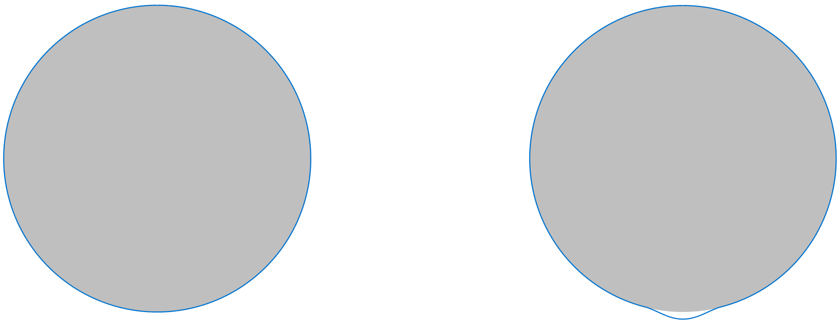

(a) $t = 0$

(b) $t \to \infty$

Figure 4.6: Illustration of a test case for assessing the importance of $\mathcal{O}(\varepsilon)$ terms. A cylinder is coated by a water film of uniform height. The cross section of the cylinder is illustrated by a grey circle and the free surface of the water film by a blue solid line. Initially, gravity forces pull down the water film forming a drop thereby increasing the curvature of the free surface. Eventually, the surface tension forces are balanced with gravity and an equilibrium is reached. An analytical expression for the maximum height of the equilibrium film can be derived as done by Evans et al. (2004).

In equilibrium, the water column is supported by the pressure arising from the surface tension at every point. Based on this observation, Evans et al. (2004) derived an ODE which describes the film surface. The problem is non-dimensionalised by a characteristic length l_c based on the capillary length which is defined by:

$$l_c = \sqrt{\frac{\sigma}{\rho_w g}} \,. \tag{4.90}$$

Given a cylinder of a radius $R = 10 l_c$ and an initial uniform water film height $h_0 = 0.002109R$, we expect for the maximum water film height $h_{max} = l_c/2$.

We set up a numerical experiment to compare the Myers model (see (4.2c)) and our set of equations given in (4.84). The computational domain consists of 400 cells along the cylinder surface as in Evans et al. (2004). Periodic boundary conditions are specified at the domain edges. The simulation is run to a dimensional time of $T = 2000\,\mathrm{s}$ and the physical parameters given in table 4.1 were used. Due to the long simulation time and small length scale the time step of the splitting strategy, as introduced in (4.86) and used in the rest of this work, severely limits the computational performance. Moreover, since the solution to this problem does not contain discontinuities a shock-capturing high-resolution method is not required. We, therefore, combine the explicit and implicit flux into a single expression and solve it implicitly for this test case. This allows us to advance the solution at much larger time steps, improving computational performance significantly.

The results are illustrated in figure 4.7. Our new model produces data in excellent agreement with the analytical results. On the other hand, the Myers model underpredicts the equilibrium surface curvature. This results in a maximum height lower than the analytical value. Since we do not track the contact line explicitly (Diez et al., 2001), we cannot directly compare the wetted surface areas. However, the area of noticeable film height is significantly larger in the Myers model than the analytical solution and our model. The runtime of both models is comparable. Based on these results, we conclude that our novel set of equations models a broader range of conditions while not noticeably increasing run time.

4.6 Flow on a two-dimensional plate

Finally, a two-dimensional showcase is presented. It is a two-dimensional extension of the first test case considered in section 4.4. Water impinges following a Gaussian profile. A constant free surface shear stress pushes the water downstream. Due to the unstable nature of this kind of flow the results are not expected to be the same as in the one-dimensional case. Global properties of these instabilities such as average finger width and velocity could also be used to validate the model and the numerical implementation. However, we have not performed such validation and it remains an

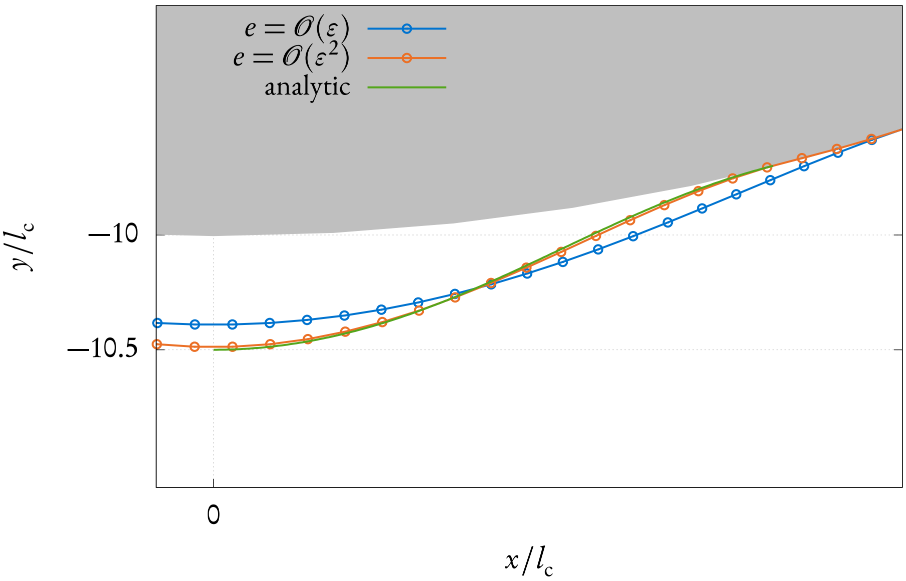

Figure 4.7: Results for the test case for assessing the importance of $\mathcal{O}(\varepsilon)$ terms. A close up of the underside of the cylinder is shown. The cylinder cross-section is the solid grey region. The free water surface for the Myers model which truncates $\mathcal{O}(\varepsilon)$ term is plotted in blue. The orange line represents the results obtained with our set of equations which truncates $\mathcal{O}(\varepsilon^2)$. The green line shows the analytic solution. The analytic maximum height is plotted as a dotted horizontal line.

item of future work. This experiment illustrates the advantages of a thin film approach that includes surface tension terms. The results are illustrated in figure 4.8. Phenomena such as finger formation can be captured which is not possible with SWIM.

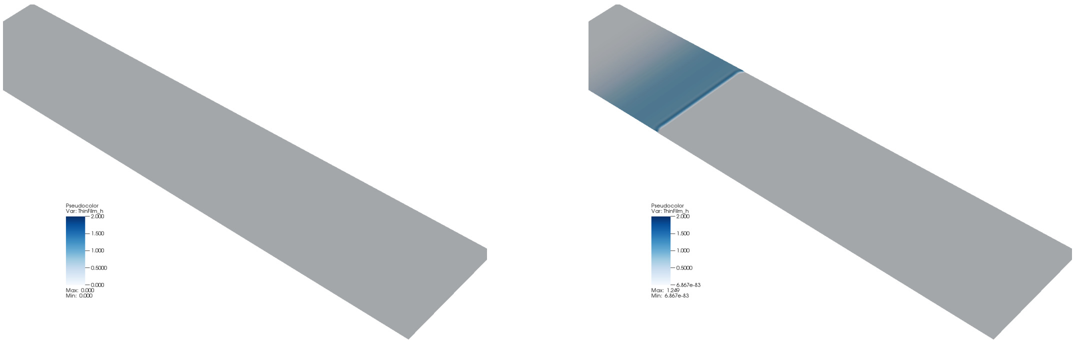

(a) $t = 0$ s (b) $t = 3$ s

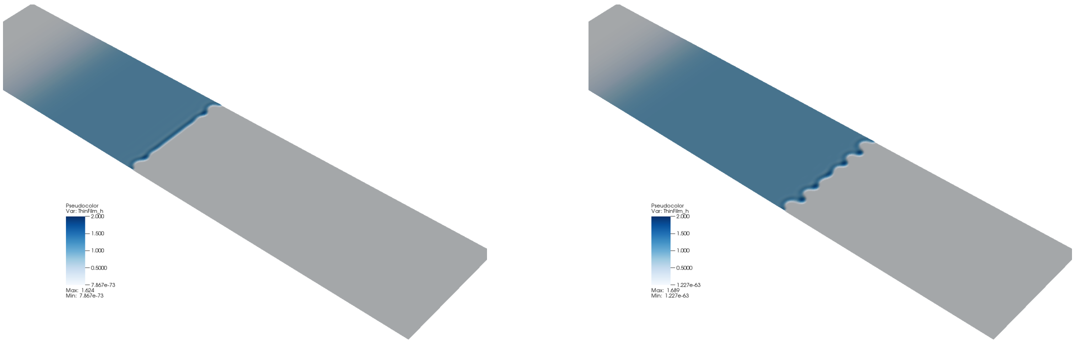

(c) $t = 6$ s (d) $t = 9$ s

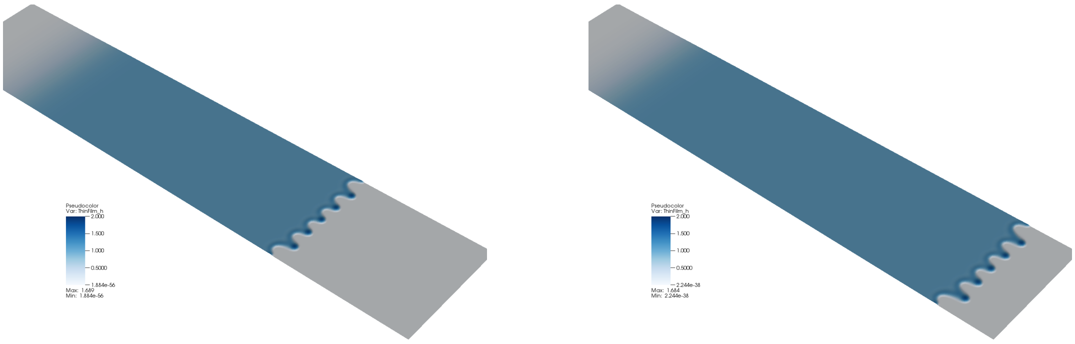

(e) $t = 12$ s (f) $t = 15$ s

Figure 4.8: Two-dimensional thin water film on a flat plate

4.7 Generalisation for independent droplet temperatures

Following the study of the water film, we turn to the discussion of the ice layer. A time evolution equation describing the ice growth can be formulated by considering conservation of energy across the ice-water interface, i.e. a Stefan condition. This approach has been widely used to describe the free surface of a phase transition (Leppäranta, 1993; Kim et al., 2006; Hu and Argyropoulos, 1996; Danilyuk, 1985) and was also applied to atmospheric ice accretion by Myers and Hammond (1999) and Myers et al. (2002a,b). A Stefan condition states that the energy which is required to move the interface (i.e. the latent heat) is supplied by heat fluxes from either phase of the interface. Application of the Stefan condition to the ice-water interface gives

$$\langle -\rho_\mathrm{i} H_\mathrm{i} \partial_t \bar{\boldsymbol{x}} - \rho_\mathrm{w} H_\mathrm{w} (\boldsymbol{v}_\mathrm{w} - \partial_t \bar{\boldsymbol{x}}) | \bar{\boldsymbol{n}} \rangle = \langle k_\mathrm{i} \nabla T_\mathrm{i} - k_\mathrm{w} \nabla T_\mathrm{w} | \bar{\boldsymbol{n}} \rangle \,, \tag{4.91}$$

where k is the thermal conductivity[2] and H enthalpy[3]. The Stefan condition establishes a relationship between the time evolution of the water-ice interface $\partial_t \bar{\boldsymbol{x}}$ and the temperatures in both phases T_i and T_w. This equation can be significantly simplified by applying the thin film assumption (i.e. $\varepsilon \ll 1$). Using conservation of mass across the interface (see equation (4.73)) and the definition of the interface normal $\bar{\boldsymbol{n}}$ the expression reads in substrate coordinate form

$$\varepsilon^2 \rho_\mathrm{i} (H_\mathrm{w} - H_\mathrm{i}) \partial_t \zeta = k_\mathrm{i} \partial_3 T_\mathrm{i} - k_\mathrm{w} \partial_3 T_\mathrm{w} - \varepsilon^2 \underline{a}^{\alpha\beta} \zeta_\beta (k_\mathrm{i} \partial_\beta T_\mathrm{i} - k_\mathrm{w} \partial_\beta T_\mathrm{w}) + \mathcal{O}(\varepsilon^3) \,. \tag{4.92}$$

We keep ε^2 terms if other non-geometrical scaling factors appear. Terms containing ε^2 and higher orders are only truncated if ε is the only scaling factor. We, therefore, retain the $\partial_t \zeta$ term and truncate the tangential derivate terms giving

$$\mathrm{St}\, \partial_t \zeta = \partial_3 T_\mathrm{i} - \frac{k_\mathrm{w}}{k_\mathrm{i}} \partial_3 T_\mathrm{w} + \mathcal{O}(\varepsilon^2) \,, \tag{4.93}$$

where we have introduced the Stefan number St which is defined by

$$\mathrm{St} = \varepsilon^2 \frac{\rho_\mathrm{i} (H_\mathrm{w} - H_\mathrm{i})}{k_\mathrm{i}} \,. \tag{4.94}$$

The heat fluxes on the right-hand side of equation (4.93) are determined by considering temperature diffusion. The Peclet number Pe is typically between 10^{-4} and 10^{-2} (Myers et al., 2002a) and is

---

[2] Note that the upright subscript $\cdot_\mathrm{i}$ denotes ice quantities whereas a slanted subscript $\cdot_i$ denotes a summation index

[3] The enthalpy is not to be confused with the mean curvature which is used earlier in this chapter

neglected. The thin film heat diffusion equation simplifies to

$$\partial_3^2 T_\mathrm{w} = \mathcal{O}(\varepsilon^2, \mathrm{Pe}) , \qquad \partial_3^2 T_\mathrm{i} = \mathcal{O}(\varepsilon^2, \mathrm{Pe}) , \tag{4.95}$$

subject to boundary conditions. The model for the temperature in the ice layer T_i is closed by Dirichlet boundary conditions on either side of the layer which are given by

$$\bar{T}_\mathrm{w} = \bar{T}_\mathrm{i} = T_\mathrm{f} , \qquad \underline{T}_\mathrm{i} = T_\mathrm{s} , \tag{4.96}$$

where T_f is the freezing Temperature assumed to be $273.15\,\mathrm{K}$, and T_s is the substrate temperature. The temperature in the water layer T_w requires an additional condition since the water temperature at the free surface $\tilde{T}_\mathrm{w}$ is unknown. The system can be closed by imposing a Neumann condition describing the heat exchange with the surroundings. The boundary condition is given by

$$\partial_3 \tilde{T}_\mathrm{w} = Q(\tilde{T}_\mathrm{w}) , \tag{4.97}$$

where Q is the heat flux at the free surface. So far, the derivation of the time evolution equation for the ice layer in this section has followed the work by Myers and Hammond (1999). In order to integrate the extra information about the droplet temperatures from chapter 2 an extension of the Myers system is required.

4.7.1 Heat exchange at the free surface

The second boundary condition accounts for the heat exchange Q with the surroundings. Numerous heat exchange mechanisms have been suggested in literature (Verdin, 2007). Icing packages have included differing subsets. A typical choice is to include kinetic energy of the droplets, droplet cooling, convective heat exchange, aerodynamic heating and evaporation (Poots, 1996) giving

$$Q = Q_\mathrm{k} - Q_\mathrm{d} - Q_\mathrm{c} + Q_\mathrm{a} - Q_\mathrm{e} , \tag{4.98}$$

where the individual terms on the right-hand side are defined as follows:

Kinetic energy: The amount of energy released as the droplets impinge. The expression reads

$$Q_\mathrm{k} = \rho_\mathrm{d} \langle \boldsymbol{v}_\mathrm{d} | \tilde{\boldsymbol{n}} \rangle \frac{||\boldsymbol{v}_\mathrm{d}||^2}{2} . \tag{4.99}$$

Droplet cooling: The energy required to heat the supercooled droplets to film temperature is given by

$$Q_\mathrm{d} = \rho_\mathrm{d} c_\mathrm{w} \langle \boldsymbol{v}_\mathrm{d} | \tilde{\boldsymbol{n}} \rangle (\tilde{T}_\mathrm{w} - T_\mathrm{d})\,. \tag{4.100}$$

Convective heat exchange: The energy transferred by convection to the surrounding air flow reads

$$Q_\mathrm{c} = h_\mathrm{c} (\tilde{T}_\mathrm{w} - T_\mathrm{a})\,. \tag{4.101}$$

Aerodynamic heating: The heat created by skin friction is given by

$$Q_\mathrm{a} = \frac{r h_\mathrm{c} \|\boldsymbol{v}_\mathrm{a}\|^2}{2 c_\mathrm{pa}}\,, \tag{4.102}$$

where r denotes the local recovery factor as given by Myers and Hammond (1999).

Evaporation: Heat loss due to evaporation is given by

$$Q_\mathrm{e} = \chi_\mathrm{e} (e(T) - e(T_\mathrm{a}))\,, \tag{4.103}$$

where e is the saturation vapour pressure and χ is the evaporation coefficient. Empirical data is available for the temperature dependency of the saturation water pressure (Smi, 1918). A commonly used approximation in atmospheric icing applications (Myers and Hammond, 1999; Poots and Skelton, 1992) empirically fits a sixth order polynomial (Lowe, 1976). The linear approximation is sufficient for a small temperature range. The vapour pressure is given by

$$e(T) = e_{(0)} + e_{(1)} (T - T_0) + \mathcal{O}(\tilde{T}_\mathrm{w} - T_0)^2\,. \tag{4.104}$$

The heat exchange term can be written as a constant factor and a temperature difference in accordance with the other terms. The final expression is given by

$$Q_\mathrm{e} = \chi_\mathrm{e} e_{(1)} (T - T_\mathrm{a}) + \mathcal{O}(T - T_0)^2\,, \tag{4.105}$$

where $e_{(1)}$ is the derivative of e evaluated at a, for icing purposes, appropriate temperature T_0.

Consequently, the Neumann boundary condition can be written as

$$\partial_3 \tilde{T}_\mathrm{w} = -a_{(0)} + a_{(1)} (\tilde{T}_\mathrm{w} - T_\mathrm{a}) + a_{(2)} (\tilde{T}_\mathrm{w} - T_\mathrm{d})\,, \tag{4.106}$$

where

$$\begin{aligned} a_{(0)} &= \frac{r h_{\mathrm{c}} \|v_{\mathrm{a}}\|^2}{2 c_{\mathrm{pa}} k_{\mathrm{w}}} + \rho_{\mathrm{d}} \langle v_{\mathrm{d}} | \tilde{n} \rangle \frac{\|v_{\mathrm{d}}\|^2}{2 k_{\mathrm{w}}} \,, \\ a_{(1)} &= \frac{h_{\mathrm{c}} + \chi_{\mathrm{e}} e_{(1)}}{k_{\mathrm{w}}} \,, \\ a_{(2)} &= \rho_{\mathrm{d}} \langle v_{\mathrm{d}} | \tilde{n} \rangle \frac{c_{\mathrm{w}}}{k_{\mathrm{w}}} \,. \end{aligned} \tag{4.107}$$

Integrating equation (4.95) with boundary conditions (4.96) and (4.106) gives

$$T_{\mathrm{w}} = T_{\mathrm{f}} + \frac{a_{(0)} - a_{(1)}(T_{\mathrm{f}} - T_{\mathrm{a}}) - a_{(2)}(T_{\mathrm{f}} - T_{\mathrm{d}})}{1 + (a_{(1)} + a_{(2)})\xi} (\eta - \zeta) \,. \tag{4.108}$$

The solution to the differential equation for the temperature in the ice layer is simpler since two Dirichlet boundary conditions are imposed. The solution is given by:

$$T_{\mathrm{i}} = T_{\mathrm{s}} + \frac{\eta}{\zeta}(T_{\mathrm{f}} - T_{\mathrm{s}}) \,. \tag{4.109}$$

For the special case of $T_{\mathrm{d}} = T_{\infty}$ we recover the solution by Myers et al. (2002b).

Free boundary problem

The Stefan problem (4.93) describes the motion of the ice-water interface. Plugging in the expressions for ice temperature (4.109) and water temperature (4.108), we obtain a differential equation for the ice height ζ given by

$$\frac{\partial \zeta}{\partial t} = \frac{a_{(3)}}{\zeta} - \frac{a_{(4)}}{1 + (a_{(1)} + a_{(2)})\xi} \,, \tag{4.110}$$

where we have introduced new substitutions to aid conciseness:

$$\begin{aligned} a_{(3)} &= \frac{k_{\mathrm{i}}(T_{\mathrm{f}} - T_{\mathrm{s}})}{\rho_{\mathrm{i}} L} \,, \\ a_{(4)} &= \frac{k_{\mathrm{w}} \left(a_{(0)} - a_{(1)}(T_{\mathrm{f}} - T_{\mathrm{a}}) - a_{(2)}(T_{\mathrm{f}} - T_{\mathrm{d}}) \right)}{\rho_{\mathrm{i}} L} \,. \end{aligned} \tag{4.111}$$

The symbol L denotes the latent heat which is defined by $L = H_{\mathrm{w}} - H_{\mathrm{i}}$. This result is a generalisation of the approach initially presented by Myers and Hammond (1999) since it also includes the droplet temperatures.

4.7.2 Numerical methods for the ice layer

The ice layer is governed by a simple ODE and is integrated with a 4^{th} order Runge Kutta scheme. However, special care needs to be taken at the transition between rime and glaze ice.

Rime-glaze ice transition

The update (4.86c) of the splitting routine (4.86) includes the ice and water layer growth due to incoming droplets and the exchange between the phases. So far, we have not discussed the situation where the substrate temperature T_s is very low or the heat flux onto the surface is too small to heat the supercooled droplets above the freezing temperature T_f. In this case, no water film is present and the rime ice equations are used. Instead of determining at what point the transition between rime and glaze icing occurs Myers et al. (2002a) make use of the presence of the precursor film. The precursor film is introduced to avoid the shear stress singularity if $\xi = 0$. A small film height ξ_p (typically on the order of $1\,\mu\text{m}$) is introduced everywhere in the domain.

If the solution to equations (4.86c) and (4.110) yields $\xi < \xi_\text{p}$ then mass is transferred to the ice phase. In this case, the state is reset and the rime ice update, given by

$$\partial_t \zeta = -\frac{\rho_\text{w}}{\rho_\text{i}} v_\text{d} \cdot \boldsymbol{n} \,, \tag{4.112}$$

is used. The update is linear and therefore solved exactly with a simple Euler forward method.

At the transition between rime to glaze ice, this approach violates conservation of mass. We apply the water flux to the ice phase in rime regions if the neighbouring cell is a glaze ice cell.

4.7.3 Summary of the physical processes in the ice layer

In section 4.2, we derived the governing partial differential equation for the water film assuming that the motion of the ice-water interface is known. In this section, we have derived a time-evolution equation for the ice layer height (see equation (4.112)).

It is based on the Stefan free boundary problem and requires the knowledge of the heat fluxes on both sides of the interface. The energy balance typically consists of kinetic energy, cooling of the droplets, convective heat exchange, aerodynamic heating and evaporation. Moreover, heat advection is neglected in the derivation which is reasonable given a typical Peclet number Pe of less than 10^{-2}.

4.8 Icing of a flat plate

We present a validation test for the full ice accretion model including the phase transition to an ice layer. The setup of the problem is similar to the once considered in section 4.4. A Gaussian water droplet distribution (4.88) impinges on an inclined flat plate. In this test case, the substrate is at a temperature of $T_\mathrm{s} = 272\,\mathrm{K}$ which causes the water to freeze. The free stream air and droplet flow are in equilibrium and no heat exchange between the phases is assumed. The free stream temperature is set to $T_\mathrm{a} = T_\mathrm{d} = 270.5\,\mathrm{K}$. The remaining physical constants are tabulated in 4.1. The flat plate is discretised on a mesh of 700 cells.

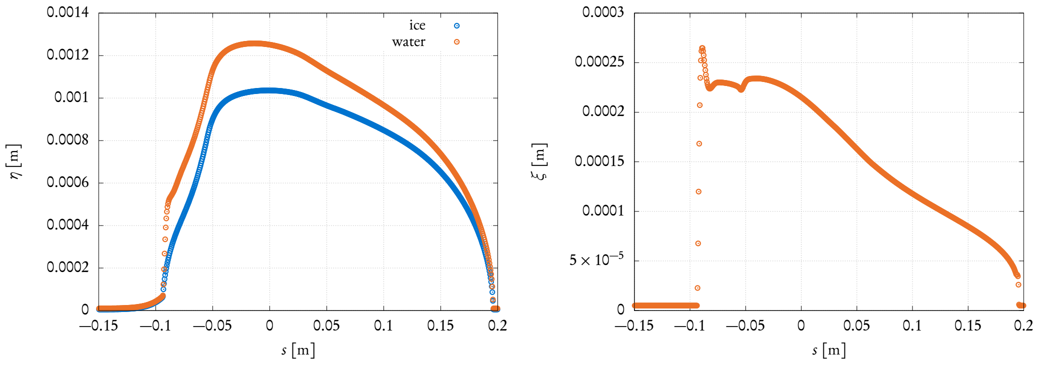

(a) Water and ice height

(b) Water height

Figure 4.9: Ice and water film on an inclined flat plate after 60 s. The different shape of the capillary ridge, compared with previous results, is due to the underlying ice layer which alters the curvature of the film.

The numerical solution is illustrated in figure 4.9 after an ice accretion time of 60 s. Due to the thin ice layer and subzero substrate temperature the water droplets impinge and freeze immediately. As the accretion grows, the ice acts as an insulator and the surface temperature reaches 273.15 K where liquid water appears. Similarly to the test cases from the water film section, gravity and shear stress forces dominate the water dynamics. Except for regions of steep gradients where surface tension forces cause a capillary ridge. The surface tension forces are proportional to the curvature of the free surface. Since the water film exists on top of the ice layer, the curvature of the ice contributes to the surface tension forces at the free surface. This manifests in a double capillary ridge and could not be captured with a model that assumes surface curvature to be negligible. Overall, we observe an excellent qualitative agreement with the results published by Myers et al. (2002b).

Finally, we study the effects of independent droplet temperatures on the ice shape. To this end, we use a high droplet temperature increase of 4 K over the free stream temperature, i.e. $\Delta T = T_\mathrm{d} - T_\mathrm{a} = 4\,\mathrm{K}$. In an ice accretion situation, this increase is due to the heat exchange with the air flow as the air temperature rises near stagnation points (see chapter 2). Otherwise, the setup is identical to the previous test case.

The results are presented in figure 4.10. The illustration compares the ice shape for $\Delta T = 0\,\mathrm{K}$ and $\Delta T = 4\,\mathrm{K}$. We observe a larger area of ice growth when the droplet temperature is increased. This is due to higher internal energy of the warmer droplets which causes a water film to appear earlier. The flux of the water layer grows with the film height. Therefore, the preferred state corresponds to minimal water height.

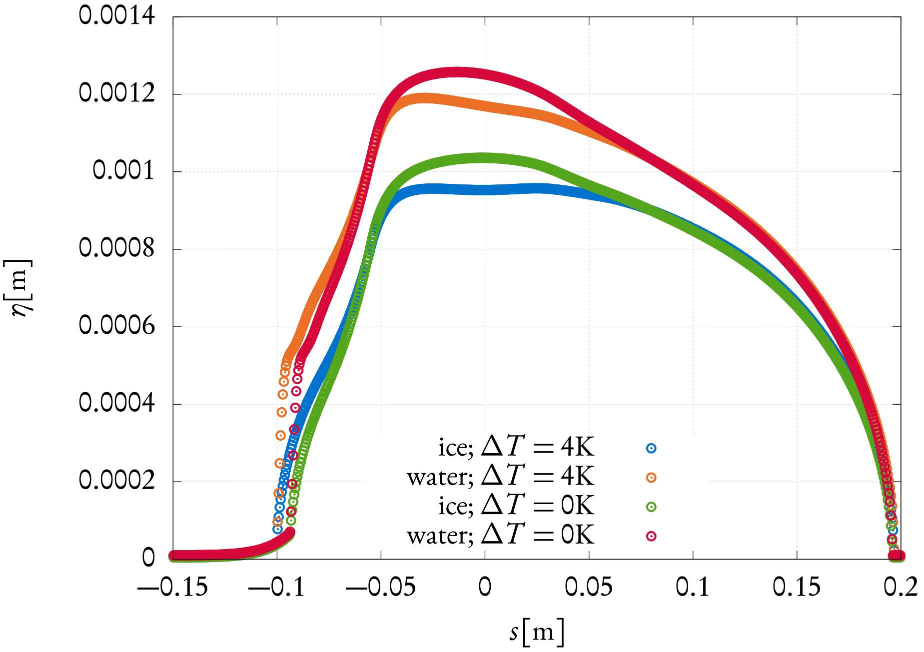

Figure 4.10: Ice and water film on an inclined flat plate after 60 s for different droplet temperatures. The higher droplet temperature has an effect on the resulting ice shape. The area of the ice growth is larger since water appears earlier due to added energy by the heat capacity of the droplets.

4.9 Conclusions

Following a literature review, we have concluded that a lubrication theory based methodology fits best with our framework while promising accurate results, albeit, the model might fail for thicker films. Systems that model the whole spectrum constitute an interesting direction for future research but are deemed not mature enough to be used in a full ice accretion simulation at this point.

We extended the lubrication theory approach to a more general class of surfaces and also improved the order of the series approximation. The new model was validated against existing numerical results where available. The effects of the improvements were demonstrated by comparing our novel model and systems from the literature with analytical results. We observe excellent agreement between our model and the exact solution.

Subsequently, the phase transition calculation was extended to account for independent droplet temperatures. A showcase study using a typical droplet temperature deviation of 4 K produced a significantly different ice shape.

Chapter 5

The full in-flight ice accretion simulation with a continuously deforming interface

In the final chapter, we present results for the full in-flight ice accretion software. Following the introduction of the modules for the air and droplet flow in chapter 2, boundary layer model in chapter 3, and the thin film dynamics in chapter 4, we combine them to give a novel methodology to study atmospheric ice accretion on aircraft.

5.1 Introduction

We begin the chapter by validating our code using a static rigid body interface against results from literature. In this case, the air and droplet flow is only computed once and the solution is assumed to remain valid throughout the ice accretion process. Many different simulation suites have been developed over the last decades and in the year 2000, the research branch of the National Atlantic Treaty Organization (NATO) the Research Technology Organization (RTO) sponsored an international task group to determine the state of the art of numerical ice accretion prediction. They published a series of test cases (Kind, 2001) which we use as benchmarks to assess the numerical performance of our methodology.

Section 5.2 presents results for two of the most difficult test cases and we find good agreement between our prediction and literature. Most ice accretion software takes into account the effect of the growing ice layer on the air flow by updating the shape of the rigid body. This is a computationally expensive operation for boundary following approaches and, hence, only done infrequently. Our Cartesian mesh based methodology is able to produce a mesh much faster making it possible to continuously update the rigid body as it evolves. The implementation of this approach is described in section 5.3. Having validated the moving boundary approach in section 5.3.4, we present results of a showcase study of a NACA 0012 aerofoil in section 5.4. Comparisons are drawn with static methods and we find that changes in the curvature of the interface have a significant effect on the air temperature and, consequently, on the ice shape.

5.2 RTO/NATO validation test cases for static meshes

A significant number of leading companies, research institutions and national agencies in aeronautics and astronautics such as NASA, Boeing, Airbus, Fokker and British Aerospace participated in the RTO workshop. Robustness and accuracy were identified to be the main subjects of assessment. 18 core (C1 - C18) and 13 optional (O1 - O13) test cases were defined. Participants could submit results for each test case, however, the experimental data was only published afterwards. The test cases were mainly glaze ice or mix-icing types which are the most difficult ones to predict. Kind (2001) published a final report where the submissions were assessed using the following grades given in order of performance

1. Poor/Unsafe,
2. Poor/Safe,
3. Poor,
4. Fair/Safe,
5. Fair/Good,
6. Fair,
7. Good/Fair and
8. Good.

Kind (2001) also noted that the consistency of ice shapes from experimental results needs to be investigated. Nevertheless, the results from this workshop constitute ideal validation data for a novel full ice accretion simulation.

We compare our findings against the submissions from established packages such as results from Gent et al. (2000) using TRAJICE2, Wright (2000) using LEWICE2.0, Paraschivoiu et al.

(2000) using CANICE and Simon (2000) using the ONERA software. Unfortunately, not every participant has submitted results for every test case. Furthermore, a significant number of test cases concern phenomena which are beyond the scope of our models such as SLD icing and ice accretion of helicopter rotor blades.

We selected the difficult cases C4 where all software ranked *poor*, and O5 where all except one achieved *poor* agreement.

5.2.1 Core data case 4

The core test case 4 (C4) is a flow over a NACA 0012 aerofoil with a chord length of $0.45\,\mathrm{m}$. A free stream pressure of $99.6\,\mathrm{kPa}$, a free stream temperature of $270.2\,\mathrm{K}$ and a free stream velocity of $77.2\,\mathrm{m\,s^{-1}}$ was specified. A water droplet phase with a liquid water content of $0.44\,\mathrm{g\,kg^{-1}}$ was introduced. The droplets were modelled using a Langmuir D distribution with a median volumetric diameter of $18\,\mathrm{\mu m}$. The extent of the ice and water layers are recorded after $T = 300\,\mathrm{s}$. The AMR method was setup to give approximately 500 cells along the chord. The ice accretion is illustrated in figure 5.1. Our results are compared to data from experiments, TRAJICE2 and ONERA. CANICE submitted also resulted but they are almost identical to the ONERA software and therefore omitted in the plot.

In summary, none of the simulations can predict the experimental ice shape accurately. Although the ice extent is well captured by Gent (2000), the stagnation point thickness and the overall ice mass are significantly underpredicted. The numerical experiments by Simon (2000) overestimate the water runback notably. The stagnation point ice thickness is underpredicted as well as the ice mass. Our results perform similarly to existing icing codes. The stagnation point thickness is slightly more accurate but the overall shape and ice mass still show significant deviation from experiments. The general trend of overestimating runback points to an issue with the representation of the driving forces in the thin film. In particular, a more accurate modelling of the boundary layer transition could improve results. It is also worth reemphasizing that our ice growth model is based on the assumption of thin accretions. The thickness ratio ε of the ice shape in figure 5.1 is 0.058 and is on the large end for the thin film assumption. Aspect ratios of the order 10^{-3} are exceeded after accretion times of $60\,\mathrm{s}$. They remain of the order 10^{-2} for accretion times on the order of minutes. This also highlights the advantage of a truncation order of $\mathcal{O}(\varepsilon^2)$ as we proposed in the previous chapter. Truncation orders of $\mathcal{O}(\varepsilon)$, as it was done previously, may introduce significant approximation errors for long accretion times.

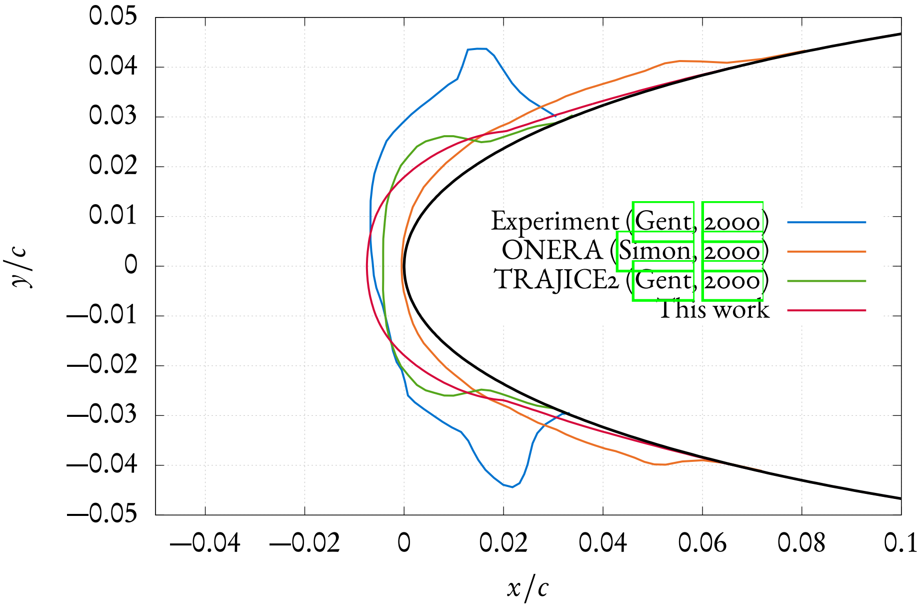

Figure 5.1: Comparison of numerical predictions and experimental results for the ice accretion for the NATO C4 test. The leading edge of a NACA 0012 is plotted in solid black. The experimentally obtained ice shape is shown in blue. Results from ONERA and TRAJICE2 are compared to our data. Paraschivoiu et al. (2000) using CANICE also submitted results for this test case but they are very similar to the predictions from ONERA.

5.2.2 Optional data case 5

The second validation study is the O5 case from the RTO workshop. A flow over a small cylinder with a diameter of 6.4 cm was considered. Similar flow conditions to the previous test are used. A free stream pressure of 99.6 kPa, a free stream temperature of 270.2 K, a free stream velocity of 77.2 $\mathrm{m\,s^{-1}}$ and a liquid water content of 0.44 $\mathrm{g\,kg^{-1}}$ was specified. The droplet diameters follow the one parameter Langmuir D distribution with a median of 18 μm.

Similarly to the previous case, this test is considered to be difficult to predict accurately. In the final report by Kind (2001), only TRAJICE2 achieved a *fair* rating the remaining submissions were graded *poor* or worse. The results are presented in figure 5.2. The predictions by ONERA show significant overprediction of water runback and underprediction of the stagnation point ice thickness. The submissions by TRAJICE2 perform better. The stagnation point thickness is only slightly smaller than experimental data and the ice extent, as well as the total mass, is underestimated.

Our results show a significantly improved stagnation point thickness and also the total ice mass and the ice extent a better captured. Given the passing grade of *fair* for the results by Gent (2000) we consider our prediction to be at least as good.

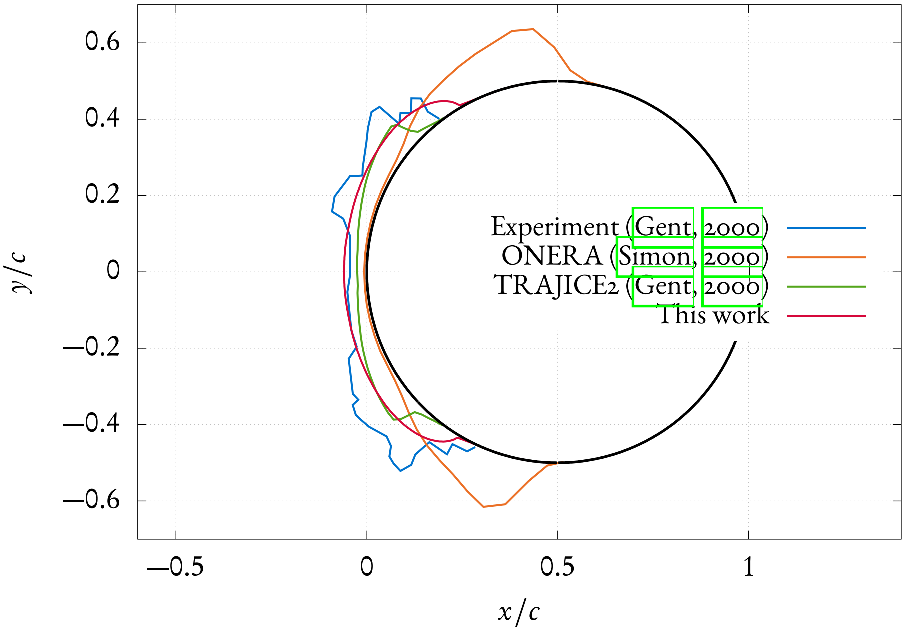

Figure 5.2: Comparison of numerical predictions and experimental results for the ice accretion for the NATO O5 test. The leading edge of a cylinder is plotted in solid black. The experimentally obtained ice shape is shown in blue. Results from ONERA and TRAJICE2 are compared to our data.

5.3 Extension for continuously deforming bodies

So far, we have only presented results for static meshes. The air and droplet solution was computed once and assumed to be valid throughout the ice accretion process. This is, in general, an injudicious assumption since the growing ice can have significant effects on the air flow.

Almost all of the icing software has the ability to incorporate the changing geometry into the process. The most popular approach is to let the user specify a remeshing time step. This approach is used by TRAJICE2, CANICE and LEWICE2.0 (Kind, 2001). Typically, approximately 10 remeshing steps are performed.

Mingione and Brandi (1998) developed a less user dependent approach based on physical quantities for the MULTIICE software. The methodology is essentially a predictor-corrector approach.

Dima and Brandi (2000) presented the results using the predictor-corrector multi-stepping at the RTO workshop. The predictor-corrector approach was later also implemented for ICECREMO by Verdin (2007) in his PhD thesis. Verdin et al. (2009) and Verdin and Charpin (2013) published comprehensive validation results. After every remesh operation, the air and droplet solver is run to steady state. Verdin (2007) concludes that this is a prohibitively expensive procedure for frequent remeshing.

Leese (2010) proposed a methodology based on a continuously deforming mesh. The implementation is based on the overlapping grid library Overture developed by Henshaw (2002). Leese (2010) was able to compute a continuously evolving ice accretion, albeit, only for a cylinder or simple rime ice conditions. More challenging test cases such as glaze ice on an aerofoil, e.g. the RTO test case C4, cause a distorted boundary following mesh which resulted in robustness issues.

This work is based on a Cartesian cut-cell approach which is able to compute the flow around complex geometries. It is therefore ideally suited to cope with the challenging geometries arising from ice growth.

5.3.1 Boundary treatment for deforming bodies

This section introduces the approach of extending the LPFS method presented in section 2.3.3 to a moving boundary. Bennett et al. (2018) extended the KBN cut-cell method to moving rigid bodies. Their approach extends a general split flux stabilisation cut-cell methodology to rigid bodies and is therefore also applicable to the LPFS method. Bennett et al. (2018) validated their approach for an oscillating NACA 0012 aerofoil against experimental results which is a relevant test case for our application.

The moving boundary methodology requires two input parameters. Firstly, the signed distance field at the current time step and, secondly, the velocity of the interface. The signed distance field is computed using the Characteristic Scan Conversion (CSC) algorithm by Roosing et al. (2018) for the polygonised geometry. The CSC algorithm is explained in more detail in appendix A. The polygon approximating the iced substrate is defined to be the union of the substrate polygon and the sequence of vertices which define the free surface. The substrate polygon is defined in section A.1.1.

The signed distance field at the next time step is approximated by advecting the 0-level set using the current interface velocity which is given by $\partial_t \tilde{x}$.

5.3.2 Summary of modules and algorithms of the full continuous ice accretion software

A high-level overview of the software employed during this project is illustrated in figures 5.3 and 5.4.

The initial setup which comprises the computing of the interfaces and applying of the initial conditions is done in parallel. A load balancer redistributes patches across all processors to optimise parallel performance. An explicit time marching method is used for the air and droplet flow which is conditionally stable. Therefore, a stable global time step has to be found which depends on the cell size and the wave speeds. The stable global time step is found by reducing the local time step over all the data patches of the whole domain. If finer AMR levels exist, the update routine is repeated for all finer levels. After all levels have been advanced to the same time, the surface data around the icing body is extracted as described in section 3.1.

From the extracted surface data, the remaining boundary layer quantities are computed using the boundary layer model which is then fed to the ice accretion solver. We have decided not to parallelise the ice and water computation. The main computational cost of the water dynamics computation arises from finding the root of equation (4.87) which requires solving a sparse linear system for every iteration. We have attempted to parallelise the routines using GPGPUs and cuSPARSE. However, memory transfer was a significant bottleneck. We have not found any speed up of the cuSPARSE implementation over the highly optimised serial libraries that exist to solve sparse linear system. It is therefore doubtful whether a naïve parallelisation would improve performance and developing a highly optimised implementation is beyond the scope of this work.

Following the update of the ice and water dynamics, the new layer heights need to be communicated to the other processes. The ice surface is represented by a sequence of vertices which is broadcast to all processors. Each processor updates the signed distance field on its local patches. Based on the modified interface, the load balancer decides whether redistribution of the workload is necessary and a new iteration starts.

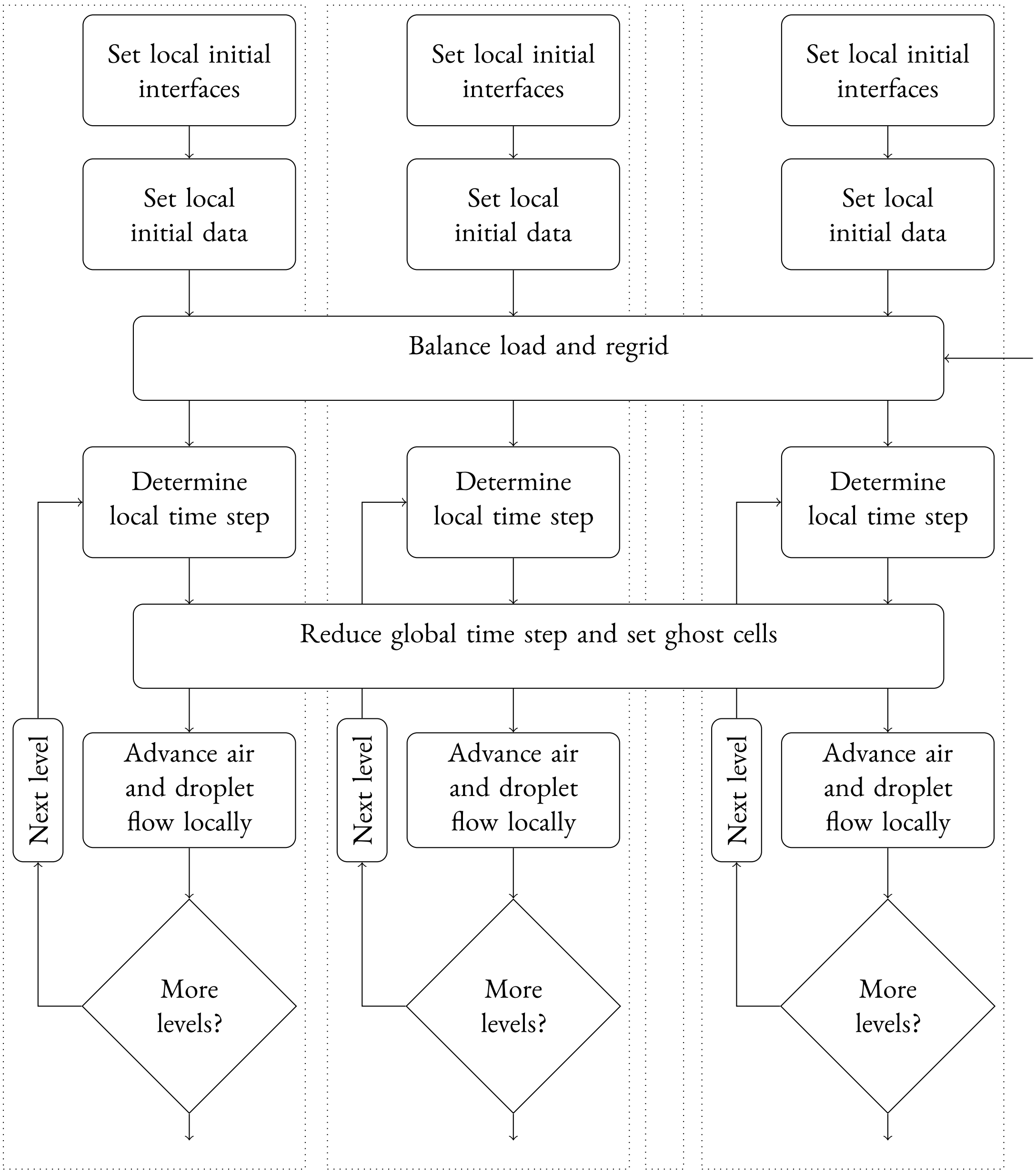

Figure 5.3: Flowchart of the full simulation with a continuously deforming interface. The air and droplet flow solver setup and update are depicted. The MPI communication is illustrated. Regions with a dotted border indicate independent processors. Blocks spanning all processors indicate communication.

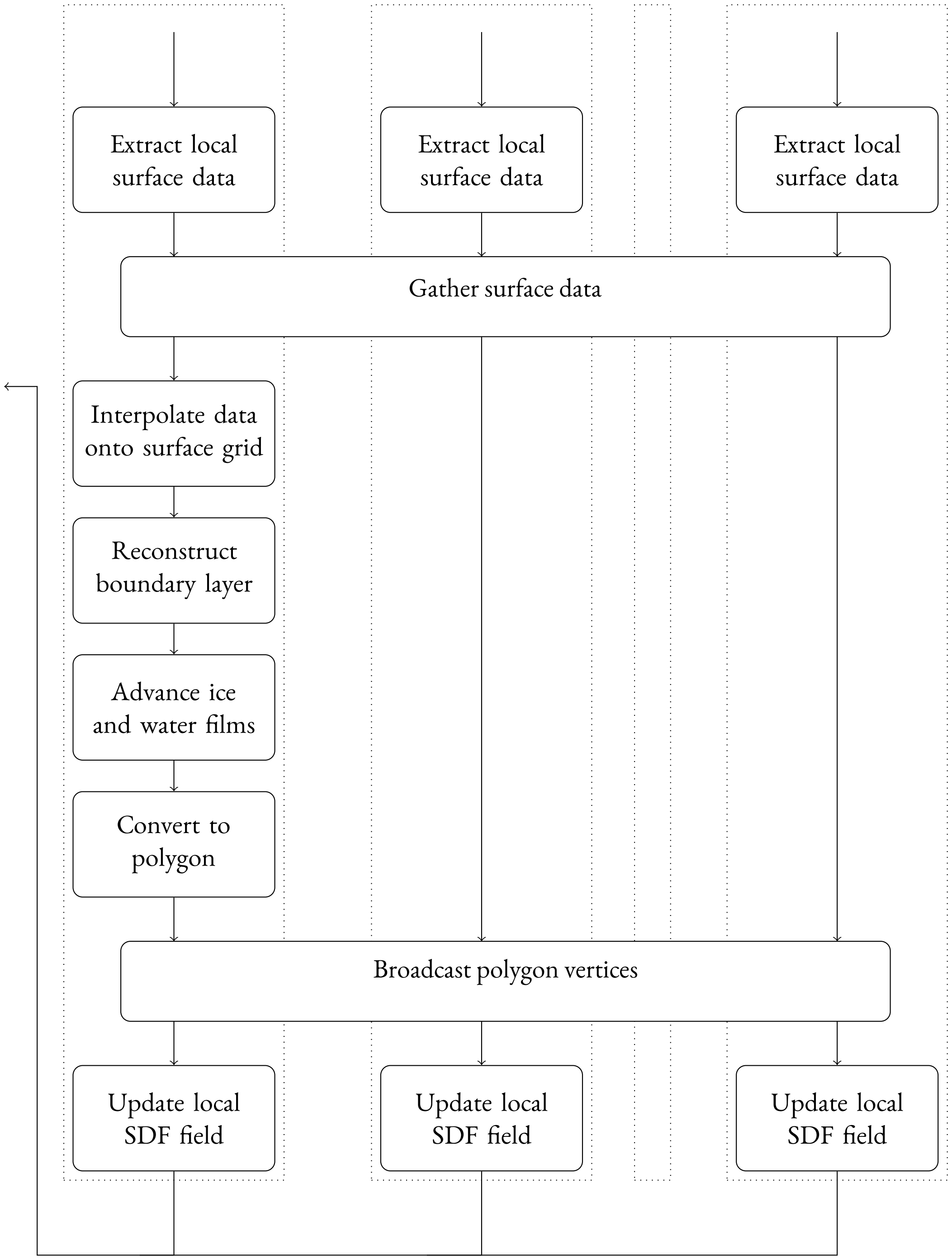

Figure 5.4: (Contd.) Flowchart of the full simulation with a continuously deforming interface. The surface data extraction, boundary layer computation and the update of the ice and water layers are illustrated.

5.3.3 Optimisations

The interpolation routines in the AMR algorithm by Bell et al. (1994) require a consistent signed distance field on all levels. Otherwise, it is possible that a fine patch of only solid cells exists above coarse fluid cells and the projection step fails. Due to this, we chose to update the geometry when the time on all levels align. This, on the other hand, allows for a significant optimisation in the context of small geometry deformation as it is typical for ice accretion simulation. If the system is near equilibrium, e.g. steady state, and the geometry deformation is small, then it is likely that the equilibrium is reached within a few time steps. On finer levels, a number of time steps are required to advance the solution to the same time as the coarsest level. Since we only update the geometry every coarsest time step, there are no effects perturbing the system form the equilibrium. Therefore, as soon as we detect a steady state on a level we can exclude its patches from the list of patches that need to be updated until the next remeshing takes place.

This process is illustrated in figure 5.5. A small perturbation in the geometry causes a new steady state to be reached after approximately a quarter of the time step on level 0 and we can deactivate the update computation until the next remeshing.

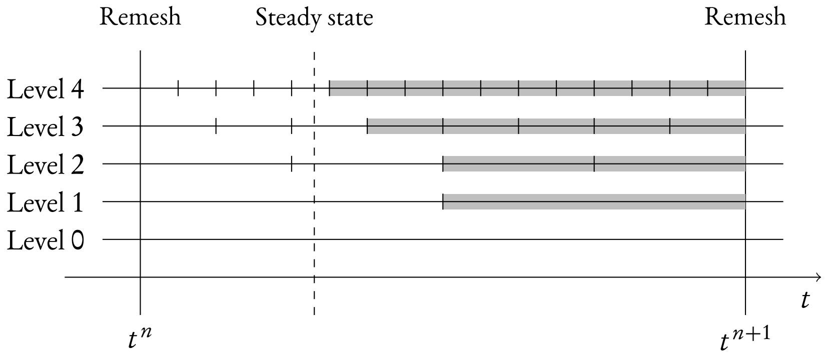

Figure 5.5: Illustration of potential optimisation exploiting the temporal structure of the AMR setup. If a steady state is detected on a level (dashed line) the update can be suspended (greyed area) until the next remeshing step since no other perturbing factors force the system out of equilibrium.

5.3.4 Validation of the implementation of the geometry update

This section validates the implementation of the representation of the moving boundary. Similarly to the test case from section 3.5, which validates that the implementation of the quantities transfer from the air and droplet module to the thin film solver, we need to confirm that the growing ice layer correctly alters the geometry.

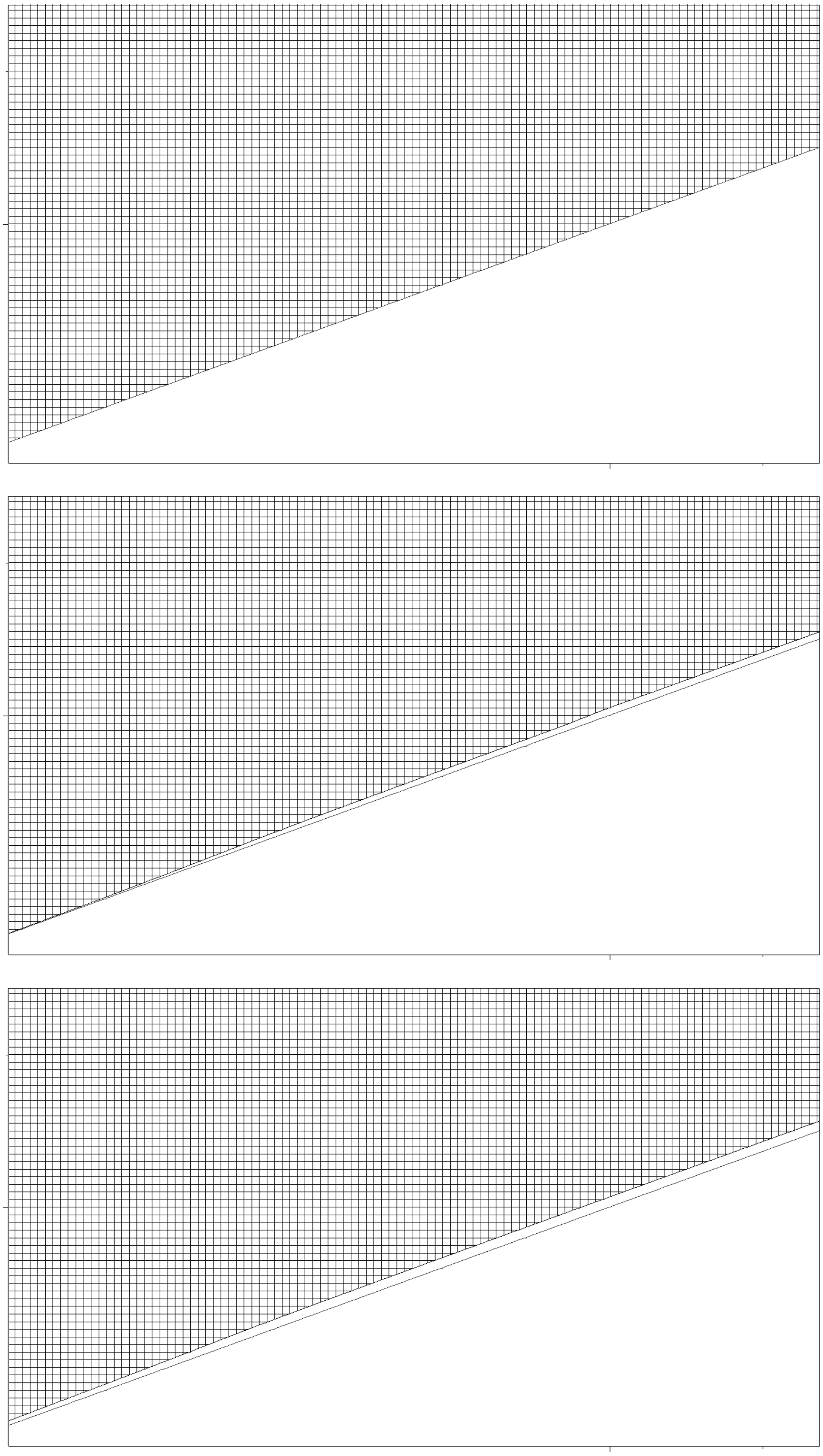

Figure 5.6: Illustration of moving film boundary of the icing of a flat inclined plate. The first subfigure shows the initial data, the second the mesh after 30 s and the third and final mesh at 60 s. The transitions of cut-cell states can be seen. Previously regular cell become cut-cells and cut-cells turn into fully covered cells.

To this end, we compare the positions of the cut-cell interface centroids with the ice and water layer heights from the substrate dynamics solver. We use a simple test case of icing of an inclined flat plate. The experimental set up is identical to the test case from section 4.8. The cut-cell mesh evolution is illustrated in figure 5.6. The first subfigure shows the initial condition and the second subfigure the mesh after the ice grew for 30 s. The framework deals robustly with the covering of small cut-cells and creating of new mixed cells from previously regular cells.

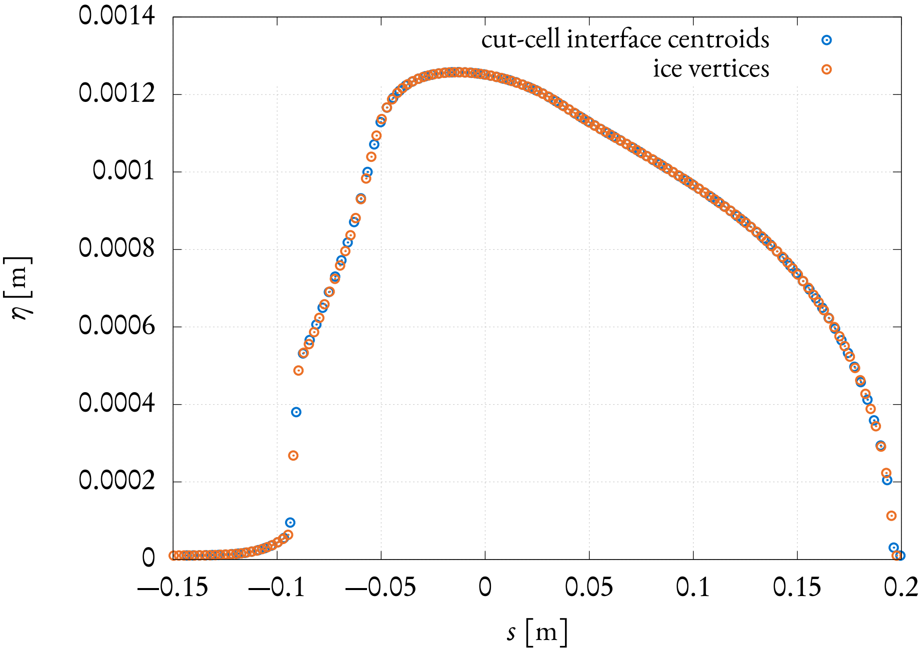

Figure 5.7: Validation results for the interface update of the icing of a flat inclined plate. The ice layer is shown after an accretion time of 60 s. The data from the ice and water film solver is represented by orange points. The cut-cell interface centroids are plotted as blue points. The cut-cell data is rotated such that the substrate aligns with the x-axis.

Figure 5.7 compares the interface centroids of the cut-cells with the layer height data from the thin film solver. The interface centroids are rotated about the origin by −20° such that their y-component represents the film height. Excellent agreement validates the polygonisation approach of coupling the growing ice layer with the cut-cell methodology.

5.4 Showcase: NACA 0012

Finally, we present a showcase of the glaze ice accretion on a continuously deforming NACA 0012 aerofoil. To the best of our knowledge, this is the first such simulation in literature.

The setup is similar to the O9 test case from the RTO workshop but an increased free stream temperature is specified to exhibit stronger glaze ice effects. An aerofoil of chord length $0.533\,\mathrm{m}$ and an angle of attack of $4°$ is introduced into a free stream flow of $103\,\mathrm{m\,s^{-1}}$, a free stream pressure of $99.6\,\mathrm{kPa}$ and a free stream temperature of $270\,\mathrm{K}$. The results are illustrated in figures 5.8 and 5.11. The simulation was run on four Intel Xeon Skylake 6142 CPUs with 16 cores each and took approximately ten days of wall-clock time to reach a simulated time of $150\,\mathrm{s}$.

Figure 5.8 compares the ice accretion on the aerofoil for the simulation with a continuously moving boundary and a static approach. Additionally, we mark the location of the stagnation point by the tip of an arrow in figure 5.8.

Initially, the two methodologies produce the same results, however, after approximately $60\,\mathrm{s}$ we see a slightly thinner accretion in the dynamic boundary case. This is due to the altering collection efficiency. Figure 5.10 illustrates the droplet trajectories at different times. Since the aerofoil is at an angle of incidence, the vertically growing ice shields the upper surface of the aerofoil from impinging water droplets. This can be seen when comparing the droplet trajectories between the dynamic and static case. The distance between impinging streamlines is directly proportional to the collection efficiency (see equation (1.2)). The blue streamlines in figure 5.10, which represent the dynamic results, are spread farther apart compared with the red streamlines obtained from the static simulation.

The difference in the two methodologies is also exhibited by considering the position of the stagnation point. In a static simulation, the stagnation point remains stationary, whereas it moves further forward towards the leading edge as the ice accretes if the interface is tracked dynamically. Eventually, it settles at the indentation below the leading edge.

The effects of a different process appear after approximately $90\,\mathrm{s}$. We believe that the appearing horn shape at the leading edge and the upper apex of the ice layer is due to the temperature field of the air flow. Air temperature contours are illustrated in figure 5.11. We notice that the, in the beginning convexly shaped, ice layer becomes flatter in the vicinity of the stagnation point. This can be observed in subfigure 5.11d and later. The flatter geometry around the stagnation point causes a larger convex curvature of the interface in its surrounding which a dynamically remeshing simulation feeds back to the air flow update. The high curvature produces a stronger expansion of the air and therefore lower temperature which causes more water to freeze adjacent to the stagnation point. The additional ice creates a protrusion at the leading edge of the aerofoil. Moreover, after $90\,\mathrm{s}$ the previously flat interface around the stagnation point turns concave. This creates a larger region of decelerated flow and higher temperature which reduces ice build-up.

A similar process can be observed at the upper apex of the ice layer and the aerofoil. The high concave curvature at the apex causes a compression which increases the air temperature. This effect starts to appear after 90 s, is slightly more pronounced after 120 s and is clearly visible at 150 s. The high-temperature region forms a barrier for the ice layer to grow further downstream. At the same time, it creates a steeper angle between the ice layer and the aerofoil which increases the curvature of the interface. Due to analogue reasons to the one described in the previous paragraph, the flow expands at this point of high convex curvature and causes ice to accrete forming another protrusion.

At this point the physical accuracy of the integral boundary layer model is debatable. The model was derived under the assumption that surface curvature is negligible which breaks down for complex interfaces like the final one presented. A desirable direction for future research is to investigate the performances of boundary layer models in the context of the ice accretion process. Nevertheless, this showcase demonstrates the increased modelling capability of the methodology by continuously evolving the accretion layer.

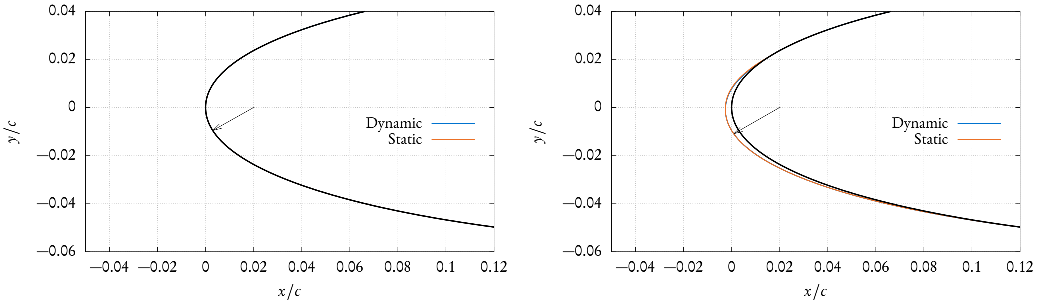

(a) $t = 0$ s

(b) $t = 30$ s

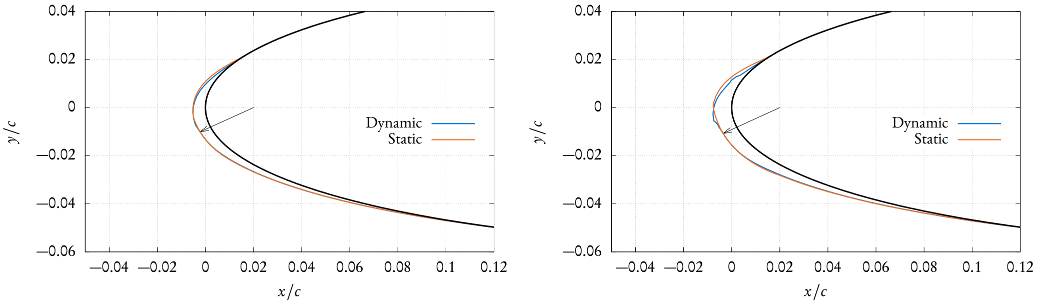

(c) $t = 60$ s

(d) $t = 90$ s

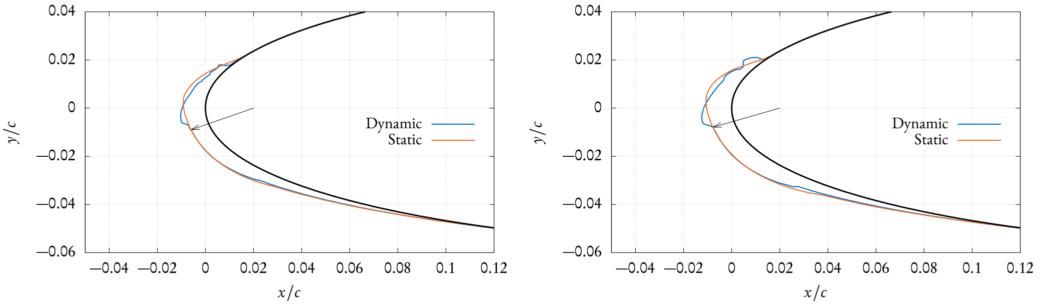

(e) $t = 120$ s

(f) $t = 150$ s

Figure 5.8: Comparison of static interface and continuously updating interface methodologies. The clean aerofoil is illustrated as a solid black curve. The ice accretion interface obtained with the static interface assumption is plotted in orange. The interface obtained using a continuous feedback of the ice shape is illustrated in blue. The moving stagnation point in the dynamic case is indicated by the arrow.

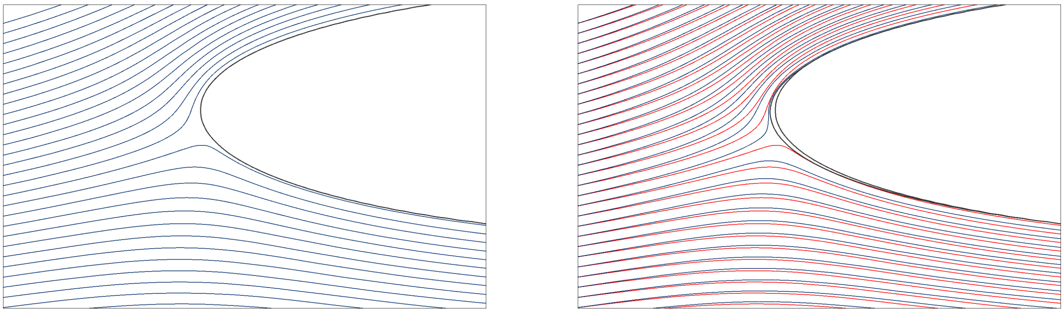

(a) $t = 0\,\mathrm{s}$ (b) $t = 30\,\mathrm{s}$

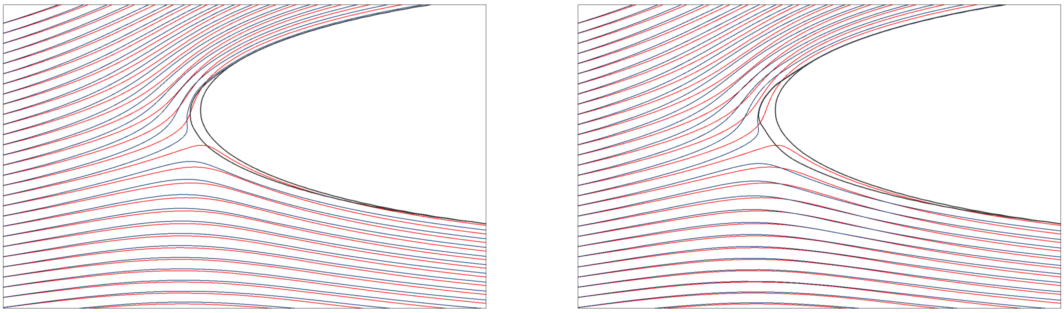

(c) $t = 60\,\mathrm{s}$ (d) $t = 90\,\mathrm{s}$

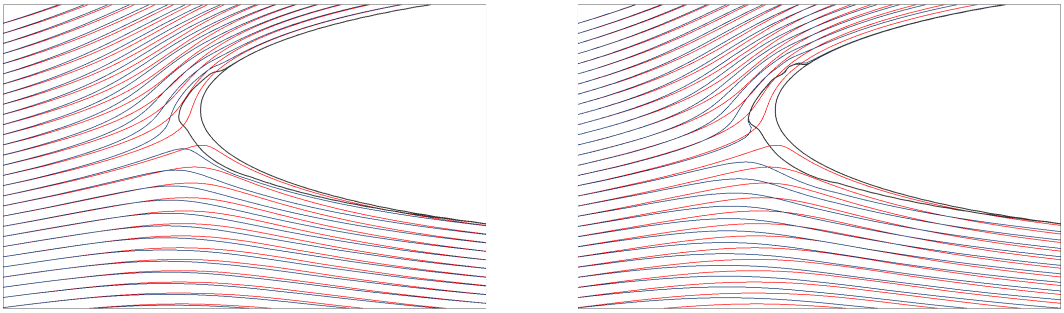

(e) $t = 120\,\mathrm{s}$ (f) $t = 150\,\mathrm{s}$

Figure 5.9: Air streamlines for the ice accretion of a NACA 0012 aerofoil. The blue streamlines represent the velocity field if the interface evolves dynamically. The red streamlines correspond to the static case.

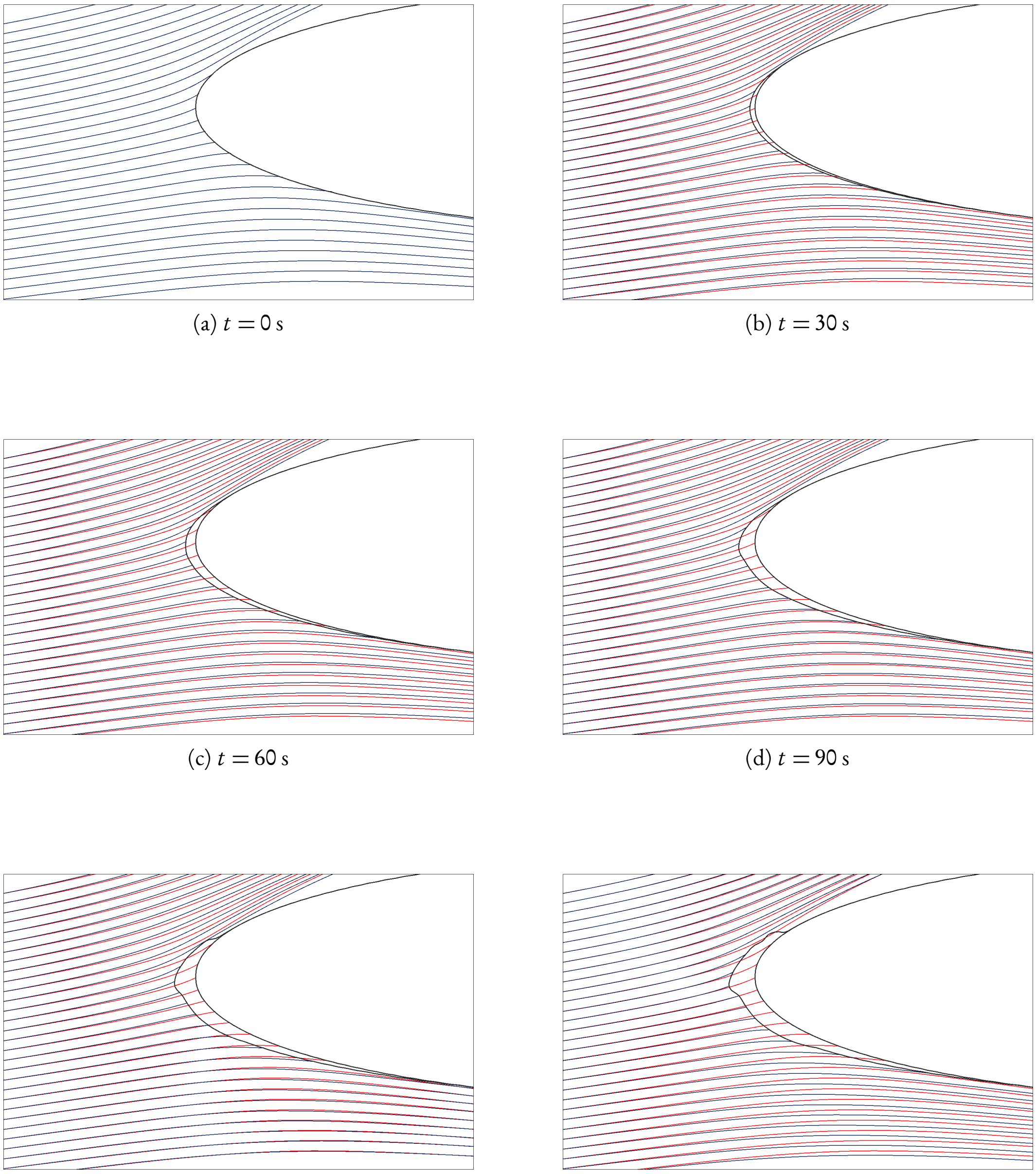

(a) $t = 0\,\mathrm{s}$

(b) $t = 30\,\mathrm{s}$

(c) $t = 60\,\mathrm{s}$

(d) $t = 90\,\mathrm{s}$

(e) $t = 120\,\mathrm{s}$

(f) $t = 150\,\mathrm{s}$

Figure 5.10: Droplet streamlines for the ice accretion of a NACA 0012 aerofoil. The blue streamlines represent the velocity field if the interface evolves dynamically. The red streamlines correspond to the static case.

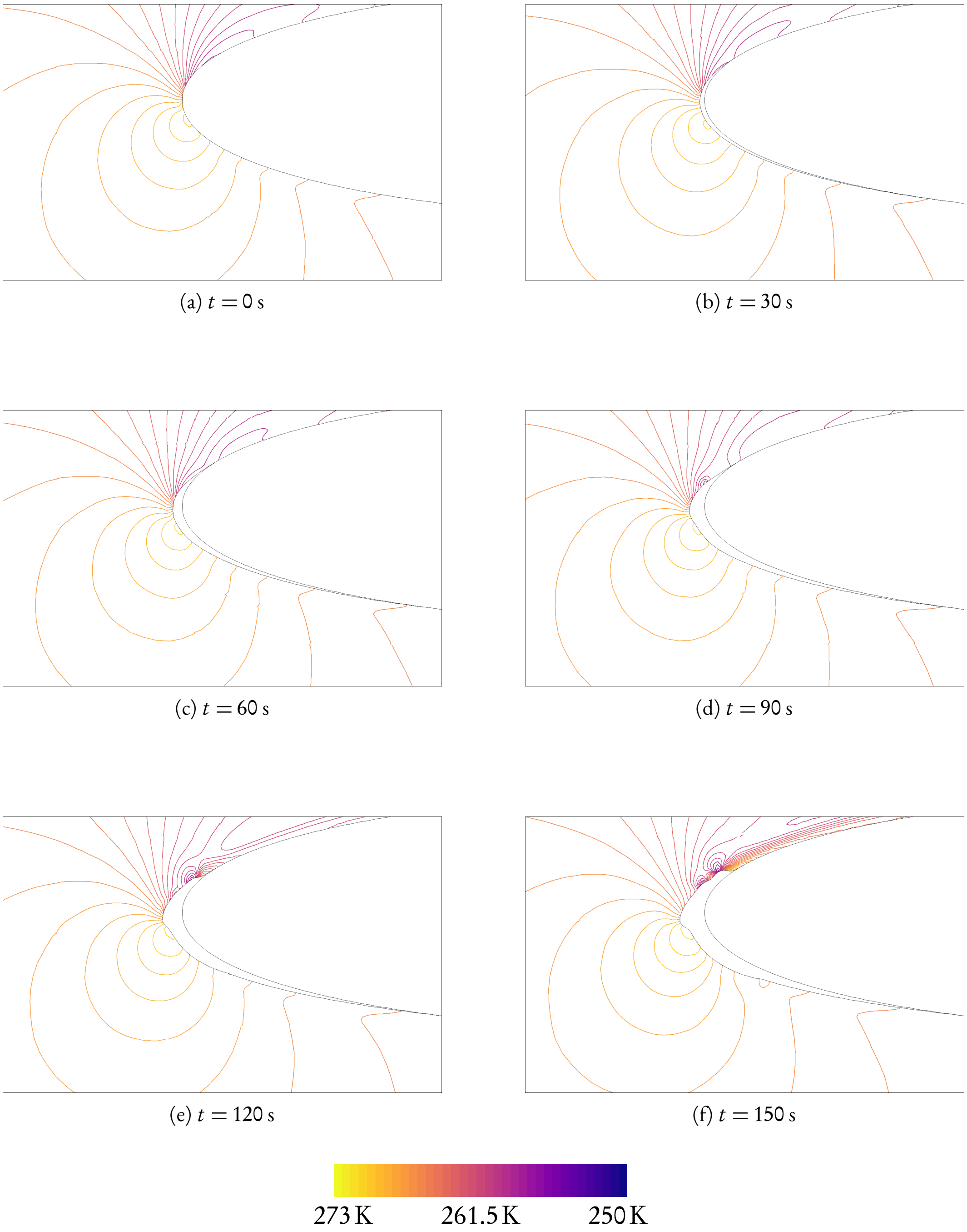

(a) $t = 0$ s

(b) $t = 30$ s

(c) $t = 60$ s

(d) $t = 90$ s

(e) $t = 120$ s

(f) $t = 150$ s

Figure 5.11: Contours of air temperature for the ice accretion of a NACA 0012 aerofoil.

5.5 Conclusions

In this chapter, we have presented the full ice accretion simulation using the Cartesian cut-cell methodology for the air and droplet flow and the extended thin film model. We validated our static approach against results from literature for the NATO test cases. We found that even for a static interface our predictions are comparable to the best performing multi-step approaches from literature.

Subsequently, we have introduced an implementation which dynamically incorporates the evolving ice layer. The novel methodology was showcased by studying the accretion of ice on a NACA 0012 aerofoil. We found that small changes in the interface curvature have a significant effect on the temperature field of the air flow which is pivotal for the ice layer dynamics. However, the simplistic integral boundary layer model is not adequate to study more general cases and improvement is left for future work. Moreover, the dynamic ice interface still represents a significant computational bottleneck. Even though the cut-cell methodology makes it possible to study accretion times on the order of minutes, a simulation of 150 s accretion time takes on the order of ten days to compute. This makes a comprehensive validation study using the NATO test cases which require an accretion time of ten minutes prohibitively expensive within the scope of this work. Nevertheless, we have demonstrated that the continuously moving boundary approach adds significant physical accuracy and we recommend for next generation ice accretion software to include this effect.

Chapter 6

Conclusions

6.1 Summary

In this thesis, we have developed a novel ice accretion simulation methodology. The framework is based on a Cartesian cut-cell mesh and we have suggested various modelling improvements to the governing equations. All of the improvements are validated or demonstrated using test cases relevant for atmospheric ice accretion on aircraft.

Modelling of droplet flow

In chapter 2, we have presented a novel model to study the water droplet flow around icing geometries. Our droplet model is augmented by an energy conservation equation and a heat exchange term. This allows the recovery of droplet temperatures as they interact with the air flow. We have demonstrated that this effect yields droplet temperature differences of up to 2 K which can be significant in the context of ice accretion.

Moreover, we have discussed the need for a non-negativity preservation property of the numerical method. The employed cut-cell method violates the requirement but using the collection efficiency boundary condition we proposed a conditional stabilisation that recovers non-negativity preservation.

We have validated the approach by computing collection efficiencies around two-dimensional aerodynamic bodies and presented a final showcase of air and droplet flow around a complex three-dimensional automotive body.

Generalisation of thin film flow on arbitrary parameterised surfaces

Subsequently, we have described a comprehensive derivation of the lubrication limit of the Navier-Stokes equation on a smoothly parameterised surface. To the best of our knowledge, the resulting model is the most general for this type of flow in literature. It has no requirements on the parameterisation except sufficient smoothness and the truncation order is higher than comparable models from literature. We demonstrated the benefits of the higher truncation order and presented results for a one-dimensional thin film flow on a two-dimensional cylinder. Our results agree significantly better with the analytical solution than commonly used approaches. Lastly, we extended the free surface boundary condition to incorporate the droplet temperatures and validated the implementation by studying the freezing of a thin film on a flat plate in one spatial dimension.

Continuously deforming ice accretion simulation

Finally, we have combined the previously presented modules to give a full in-flight ice accretion simulation. We validated our methodology against results from literature for the NATO icing workshop test cases. We found that even for a static interface our results agree well with results from multi-step methodologies.

Subsequently, we presented a novel approach to describe a continuously moving ice interface utilising the fast mesh generation capability of the Cartesian cut-cell method. We illustrated the advantages of such a methodology by studying the ice accretion on a NACA 0012 aerofoil. We have found that the interface curvature has a significant effect on the air flow. An increase in the curvature causes pronounced compression or expansion of the air phase which in turn creates regions of high temperature. These regions have a pivotal effect on the extent of the ice layer and form protrusion. This kind of analysis has previously not been possible with multi-step methods or static interface methods.

6.2 Further Work

Finally, we present directions for future research we believe could improve the ice accretion prediction capability of CFD methods.

Boundary layer model and roughness model: The convective heat transfer coefficient has a leading effect on the freezing process. Further investigation is necessary to establish the accuracy of the integral boundary layer model. In particular, the surface roughness and regions of high interface curvature could create a turbulent transition.

Inertial effects in the thin film model: Research by Rothmayer and Tsao (2000) has shown that the lubrication theory approach to modelling the water film breaks down for thicker films when air pressure gradients drive the water layer. In such a case inertia terms within the film become important. A comprehensive thin film model for fast flows based on centre manifold theory was developed by Roy et al. (2002). Centre manifold theory acts as an ideal framework to generalise the lubrication approximation model to faster flows.

Lateral discretisation of ice temperature field: The governing equations for the water and ice film assume that heat conduction mainly occurs in the substrate normal direction. For large accretion, further investigation is necessary to confirm this hypothesis. Alternatively, the temperature field in the ice should be computed without a thin layer assumption.

SLDs: We have neglected super large droplets since they exhibit new dynamics such as break-up and merging. There are empirical approaches to take these effects into account which would make a straightforward generalisation possible. Nevertheless, more theoretical approaches would be desirable.

Three-dimensional flow: Most of the modules we presented are validated or generalise straightforwardly to three-dimensional flow. Only the boundary layer model requires more work in order to study more than two dimensions. Some effects such as viscous finger formation of the water film are only possible in three space dimensions and an extension would therefore immediately allow the study of more physical effects.

Appendix A

Representation of icing geometries

In this appendix, we describe how icing bodies are represented in the numerical simulation. The geometry is an essential part of two stages of the simulation process. Firstly, it determines the air and water droplet flow. The geometry is incorporated into the flow simulation through the cut-cell methodology. This approach requires knowledge of various geometrical properties of the intersection of the Cartesian grid cells with the geometry such as volume fractions and face fractions of the cut-cells, and interface normals. Secondly, the governing system of the water film flow and ice growth depends on the tangential and normal vectors of the surface. Furthermore, the boundary conditions at the free surface depend on the curvature of the geometry. Given the multitude of dependencies, a unifying approach to representing the geometry is desirable.

One of these approaches, and the one mainly employed in this work, is to describe the geometry as a parametric surface. Let U be the parameter space then the surface of the geometry is the image of a parametrisation $\underline{\boldsymbol{x}} : U \rightarrow \mathbb{R}^D$. Given a parameterisation tangent and normal vectors, curvatures, etc. are readily computed. However, the analytical expression can be rather convoluted, hence, we use SymPy, a computer algebra Python library, to generate the relevant derivates and produce C-code. The approach of defining the geometry via a parametrisation also ties in well with the computation of the cut-cell geometry parameters.

A.1 Extraction of cut-cell parameters

All relevant cut-cell parameters such as fluid volume fraction α, face fractions β and interface normals $\boldsymbol{n}$ can be obtained from a vertex centred signed distance field assuming a flat interface in every cell. Under this assumption, the cut-cell parameters are readily found. The set of explicit formulas is summarised by Gokhale et al. (2018).

A.1.1 Signed distance function

The efficient implementation of a signed distance function is a less straightforward problem. The signed distance function ϕ of a geometry Ω is defined by

$$\phi(\boldsymbol{x}) = o \inf_{\hat{\boldsymbol{x}} \in \partial\Omega} d(\boldsymbol{x}, \hat{\boldsymbol{x}}) \,, \qquad o = \begin{cases} 1 & \text{if } \boldsymbol{x} \in \Omega \\ -1 & \text{otherwise} \end{cases} \,. \tag{A.1}$$

The value of the signed distance function is required for every cell vertex in the computational mesh. In general, this means that a minimisation problem has to be solved for every cell making this a computationally expensive part of the simulation. For static boundaries, this might be acceptable but for a moving surface, a more efficient approach is required. Since the step of extracting cut-cell parameters from the signed distance function assumes a piecewise flat interface, we extend this assumption and replace the geometry Ω with a polyhedron approximating the surface $\partial\Omega$.

Efficient algorithms exist to populate the signed distance function of a piecewise flat geometry such as polyhedra on a rectangular mesh. We briefly summarise the used algorithm in section A.1.2. Given a parametric surface, a polyhedra approximation is easily computed by sampling the surface in regular intervals. The interval size should be based on the computational cell size and the speed of the parametrisation. We usually require the characteristic physical length of an interval $\Delta\sigma$ to be less than half of the characteristic size of a computational cell. The arc length $\Delta\sigma$ can then be translated into a coordinate interval Δs using the relation

$$\mathrm{d}\sigma^2 = \underline{a}_{\mu\nu} \, \mathrm{d}s^\mu \, \mathrm{d}s^\nu \,, \tag{A.2}$$

where $\underline{a}$ is the first fundamental form of the surface.

A.1.2 The Characteristic Scan Conversion (CSC) algorithm

A widely used method was developed by Mauch (2001, 2003) and subsequently optimised for the use on GPGPUs by Roosing et al. (2018). This algorithm is linear in both the number of grid points and the number of geometry nodes and the algorithm works as follows:

In the beginning, all cells are updated to the largest representable floating point value. The algorithm walks along nodes and flat elements of the tessellated geometry. If a flat part is encountered, the surface is extruded along the normal direction. The shortest distance of all cells within the volume to the geometry is along the normal of the surface and, therefore, easily computed. We update all cells within the extruded volume if the magnitude of the new value is smaller than the magnitude of the current one. We define a similar volume for nodes by considering the pyramid which is constructed by taking the apex to be the node and the sides to be along the neighbouring normals. Again, the shortest distance to the geometry for all cells within this volume is directly to the apex. We update all cells in a similar fashion to the straight part. This method partitions the whole domain and, therefore, assigns every cell a signed distance.

A.2 Example: NACA 0012

The NACA four-digit aerofoil series is a popular validation case for CFD studies. The original definition of the aerofoil shape by Jacobs et al. (1933) is given as an explicit function for the upper and lower half of the geometry. Every digit encodes a parameter which relates to the shape of the aerofoil. The first two digit represent the camber of the geometry. Profiles which start with 00 have no camber and are symmetric. Especially the NACA 0012 aerofoil is a popular object of studies and is widely found in experimental setups. It is also featured in a number of core test cases from the NATO/RTO icing workshop as given in Kind (2001) which makes the NACA 0012 an important validation geometry for this work. The original definition of the NACA polynomial by Jacobs et al. (1933) as an explicit function which causes numerical problems when computing the normal of the geometry since the derivative diverges. Therefore, we use a Bezier representation given by

$$\underline{x}(s) = \sum_{k=0}^{8} \boldsymbol{P}_k \, b_{k,8}(s) \,, \tag{A.3}$$

where $b_{k,8}$ denote the Bernstein basis polynomials of degree 8 and $\boldsymbol{P}_k$ the control points. The control points for a NACA 0012 aerofoil of chord length 1 were determined by Boehm (1987) and are given by

$$\begin{aligned}
\boldsymbol{P}_0 &= \begin{pmatrix} 0.0 \\ 0.0 \end{pmatrix}, & \boldsymbol{P}_1 &= \begin{pmatrix} 0.0 \\ 0.0222672 \end{pmatrix}, & \boldsymbol{P}_2 &= \begin{pmatrix} 0.035 \\ 0.0418356 \end{pmatrix}, \\
\boldsymbol{P}_3 &= \begin{pmatrix} 0.10714 \\ 0.0587028 \end{pmatrix}, & \boldsymbol{P}_4 &= \begin{pmatrix} 0.21429 \\ 0.0698568 \end{pmatrix}, & \boldsymbol{P}_5 &= \begin{pmatrix} 0.35714 \\ 0.0668688 \end{pmatrix}, \\
\boldsymbol{P}_6 &= \begin{pmatrix} 0.53571 \\ 0.0539148 \end{pmatrix}, & \boldsymbol{P}_7 &= \begin{pmatrix} 0.75 \\ 0.0363372 \end{pmatrix}, & \boldsymbol{P}_8 &= \begin{pmatrix} 1. \\ 0.00126 \end{pmatrix}.
\end{aligned} \tag{A.4}$$

Therefore, the parameter space $U = [-1, 1]$ and the image of $\underline{\boldsymbol{x}}(U)$ is the surface of the geometry. The polygon vertices are given by the sequence $\underline{\boldsymbol{x}}(s_i)$ where $s_i := s_0 + i\Delta s$ with $s_0 := \inf U$, $s_i \in U$ and $\Delta s \leq \Delta x \sqrt{\underline{a}}/2$, where Δx is the smallest grid spacing.

Bibliography

Smithsonian Meteorological Tables, 1918.

V. Abdollahi, W. G. Habashi, and M. Fossati. Hybrid Quasi Molecular-Continuum Modeling of Supercooled Large Droplet Dynamics for In-flight Icing Conditions. In *54th AIAA Aerospace Sciences Meeting*, number January, pages 1–11, Reston, Virginia, jan 2016. American Institute of Aeronautics and Astronautics. ISBN 978-1-62410-393-3. doi: 10.2514/6.2016-0061.

R. Abgrall. On Essentially Non-oscillatory Schemes on Unstructured Meshes: Analysis and Implementation. *Journal of Computational Physics*, 114(1):45–58, sep 1994. ISSN 00219991. doi: 10.1006/jcph.1994.1148.

M. J. Aftosmis, M. J. Berger, and G. Adomavicius. A parallel multi-level method for adaptively refined cartesian grids with embedded boundaries. *38th Aerospace Sciences Meeting and Exhibit*, (January), 2000.

K. M. Al-Khalil, C. Horvath, D. R. Miller, and W. B. Wright. AIAA 97-0051 Validation of Thermal Ice Protection Computer Codes : Part 3- The Validation of ANTICE 35 th Aerospace Sciences Meeting & Exhibit. In *35th Aerospace Sciences Meeting & Exhibit*, Reno, Nevada, 1997.

J. L. Amick. Comparison of the Experimental Pressure Distribution on an NACA 0012 Profile at high Speeds with that calculated by the relaxation method. Technical report, National Advisory Comittee for Aeronautics, Langley, 1950.

J. D. Anderson. *Fundamentals of Aerodynamics*. Anderson series. McGraw-Hill Education, 5th edition, 2011. ISBN 9780073398105.

C. Bartels, J. Cliquet, and C. Bautista. Improvement of Ice Accretion Prediction Capability of the ONERA 2D Icing Code. 2015. doi: 10.4271/2015-01-2103.

P. T. Barton, B. Obadia, and D. Drikakis. A conservative level-set based method for compressible solid/fluid problems on fixed grids. *Journal of Computational Physics*, 230(21):7867–7890, sep 2011. ISSN 00219991. doi: 10.1016/j.jcp.2011.07.008.

Batchelor G. K. *An Introduction to Fluid Dynamics*. Cambridge University Press, 2000.

J. T. Batina. Unsteady Euler airfoil solutions using unstructured dynamic meshes. *AIAA Journal*, 28(8):1381–1388, aug 1990. ISSN 0001-1452. doi: 10.2514/3.25229.

BEA. Final Report on the accident on 1st June 2009 to the Airbus A330-203 registered F-GZCP operated by Air France AF 447 Rio de Janeiro - Paris. Technical report, 2012.

H. Beaugendre, F. Morency, and W. G. Habashi. FENSAP-ICE's Three-Dimensional In-Flight Ice Accretion Module: ICE3D. *Journal of Aircraft*, 40(2), 2003.

J. Bell, M. J. Berger, J. Saltzman, and M. Welcome. Three-Dimensional Adaptive Mesh Refinement for Hyperbolic Conservation Laws. *SIAM Journal on Scientific Computing*, 15(1):127–138, jan 1994. ISSN 1064-8275. doi: 10.1137/0915008.

W. P. Bennett, N. Nikiforakis, and R. Klein. A moving boundary flux stabilization method for Cartesian cut-cell grids using directional operator splitting. *Journal of Computational Physics*, 368:333–358, 2018. ISSN 10902716. doi: 10.1016/j.jcp.2018.04.048.

M. J. Berger and M. J. Aftosmis. Progress Towards a Cartesian Cut-Cell Method for Viscous Compressible Flow. In *50th AIAA Aerospace Sciences Meeting including the New Horizons Forum and Aerospace Exposition*, Reston, Virigina, jan 2012. American Institute of Aeronautics and Astronautics. ISBN 978-1-60086-936-5. doi: 10.2514/6.2012-1301.

M. J. Berger and P. Colella. Local adaptive mesh refinement for shock hydrodynamics. *Journal of Computational Physics*, 82(1):64–84, may 1989. ISSN 00219991. doi: 10.1016/0021-9991(89)90035-1.

G. Blanchard, N. Bempedelis, C. Bayeux, E. Radenac, and P. Villedieu. 3D ice accretion modeling using an integral boundary layer method. In *7th European Conference for Aeronautics and Aerospace Sciences*, volume M, page 31055, 2017. doi: 10.13009/EUCASS2017-400.

W. Boehm. Bézier presentation of airfoils. *Computer Aided Geometric Design*, 4(1-2):17–22, jul 1987. ISSN 01678396. doi: 10.1016/0167-8396(87)90021-5.

F. Bouchut. On zero pressure gas dynamics. In *Advances in Kinetic Theory and Computing: Selected Papers*, pages 171–189. World Scientific, 1994. ISBN 9789810216719.

Y. Bourgault, H. Beaugendre, and W. G. Habashi. Development of a Shallow-Water Icing Model in FENSAP-ICE. *Journal of Aircraft*, 37(4):640–646, 2000a. ISSN 0021-8669. doi: 10.2514/2.2646.

Y. Bourgault, Z. Boutanios, and W. G. Habashi. Three-Dimensional Eulerian Approach to Droplet Impingement Simulation Using FENSAP-ICE, Part 1: Model, Algorithm, and Validation. *Journal of Aircraft*, 37(1):95–103, 2000b. doi: 10.2514/2.2566.

Y. Cao and J. Huang. New Method for Direct Numerical Simulation of Three-Dimensional Ice Accretion. *Journal of Aircraft*, 52(2):1–10, 2014. ISSN 0021-8669. doi: 10.2514/1.C032824.

Y. Cao, Z. Wu, Y. Su, and Z. Xu. Aircraft flight characteristics in icing conditions. *Progress in Aerospace Sciences*, 74:62–80, 2015. ISSN 03760421. doi: 10.1016/j.paerosci.2014.12.001.

F. Capizzano and E. Iuliano. A Eulerian Method for Water Droplet Impingement by Means of an Immersed Boundary Technique. *Journal of Fluids Engineering*, 136(4):040906, feb 2014. ISSN 0098-2202. doi: 10.1115/1.4025867.

T. Chilton and A. Colburn. Mass Transfer (Absorption) Coefficients Prediction from Data on Heat Transfer and Fluid Friction. *Industrial & Engineering Chemistry*, 26(11):1183–1187, 1934. ISSN 0019-7866. doi: 10.1021/ie50299a012.

S. G. Cober, G. a. Isaac, and J. W. Strapp. Characterizations of Aircraft Icing Environments that Include Supercooled Large Drops, 2001. ISSN 0894-8763.

P. Colella, D. T. Graves, B. J. Keen, and D. Modiano. A Cartesian grid embedded boundary method for hyperbolic conservation laws. *Journal of Computational Physics*, 211(1):347–366, jan 2006. ISSN 00219991. doi: 10.1016/j.jcp.2005.05.026.

R. A. da Silveira and C. Maliska. Numerical Simulation of Ice Accretion on the Leading Edge of Aerodynamic Profiles. In *Proceedings of the 2nd International Conference on Computational Heat and Mass Transfer*, pages 0–7, Rio de Janeiro, 2001.

R. A. da Silveira, C. R. Maliska, D. A. Estivan, and R. Mendes. Evaluation of Collection Efficiency Methods for Icing Analysis. In *Proceedings of COBEM 2003*, Sao Paulo, 2003.

I. I. Danilyuk. On the Stefan problem. *Russian Mathematical Surveys*, 40(5):157–223, oct 1985. ISSN 0036-0279. doi: 10.1070/RM1985v040n05ABEH003684.

J. A. Diez, L. Kondic, and A. Bertozzi. Global models for moving contact lines. *Physical Review E - Statistical, Nonlinear, and Soft Matter Physics*, 63(1 II):1–13, 2001. ISSN 15393755. doi: 10.1103/PhysRevE.63.011208.

C. Dima and V. Brandi. Prediction of Ice Accretion on Airfoils using CIRA Multi-Ice code. Technical report, CIRA, Centro itialiano Ricerche Aerospaziali, Capua, Italy, 2000.

B. Einfeldt, C. Munz, P. Roe, and B. Sjögreen. On Godunov-type methods near low densities. *Journal of Computational Physics*, 92(2):273–295, feb 1991. ISSN 00219991. doi: 10.1016/0021-9991(91)90211-3.

P. L. Evans, L. W. Schwartz, and R. V. Roy. Steady and unsteady solutions for coating flow on a rotating horizontal cylinder: Two-dimensional theoretical and numerical modeling. *Physics of Fluids*, 16(8):2742–2756, 2004. ISSN 10706631. doi: 10.1063/1.1758943.

G. Fortin, J.-L. Laforte, and A. Ilinca. Heat and mass transfer during ice accretion on aircraft wings with an improved roughness model. *International Journal of Thermal Sciences*, 45(6):595–606, jun 2006. ISSN 12900729. doi: 10.1016/j.ijthermalsci.2005.07.006.

T. Frankel. *The Geometry of Physics*. Cambridge University Press, Cambridge, 2011. doi: 10.1017/CBO9781139061377.

R. W. Gent. TRAJICE2 Code Results. In *NATO/RTO Workshop on Ice Accretion Simulation Evaluation Test*, Capua, Italy, 2000.

R. W. Gent, N. P. Dart, and J. T. Cansdale. Aircraft icing. *Philosophical Transactions of the Royal Society A: Mathematical, Physical and Engineering Sciences*, 358(1776):2873–2911, 2000. ISSN 1364-503X. doi: 10.1098/rsta.2000.0689.

N. Gokhale, N. Nikiforakis, and R. Klein. A dimensionally split Cartesian cut cell method for hyperbolic conservation laws. *Journal of Computational Physics*, 364:186–208, 2018. ISSN 00219991. doi: 10.1016/j.jcp.2018.03.005.

R. J. Hansen and T. Y. Toong. Interface behavior as one fluid completely displaces another from a small-diameter tube. *Journal of Colloid And Interface Science*, 36(3):410–413, 1971. ISSN 00219797. doi: 10.1016/0021-9797(71)90014-2.

D. Hartmann, M. Meinke, and W. Schröder. An adaptive multilevel multigrid formulation for Cartesian hierarchical grid methods. *Computers & Fluids*, 37(9):1103–1125, oct 2008. ISSN 00457930. doi: 10.1016/j.compfluid.2007.06.007.

W. Henshaw. Overture: An Object-Oriented Framework for Overlapping Grid Applications. In *32nd AIAA Fluid Dynamics Conference and Exhibit*, Reston, Virigina, jun 2002. American Institute of Aeronautics and Astronautics. ISBN 978-1-62410-113-7. doi: 10.2514/6.2002-3189.

H. Hu and S. A. Argyropoulos. Mathematical modelling of solidification and melting: a review. *Modelling and Simulation in Materials Science and Engineering*, 4(4):371–396, jul 1996. ISSN 0965-0393. doi: 10.1088/0965-0393/4/4/004.

E. N. Jacobs, K. E. Ward, and R. M. Pinkerton. The Characteristics of 78 Related Airfoil Sections from Tests in the Variable-Density Wind Tunnel. Technical report, National Adivsory Committee For Aeronautics, 1933.

A. Jameson, W. Schmidt, and E. Turkel. Numerical Solution of the Euler Equations by Finite Volume Methods Using Runge-Kutta Time-Stepping Schemes. In *14th Fluid and Plasma Dynamics Conference*, volume M, pages 1–19, Palo Alto, CA, jun 1981. American Institute of Aeronautics and Astronautics. doi: 10.2514/6.1981-1259.

S. Jung and R. Myong. A second-order positivity-preserving finite volume upwind scheme for air-mixed droplet flow in atmospheric icing. *Computers & Fluids*, 86:459–469, nov 2013. ISSN 00457930. doi: 10.1016/j.compfluid.2013.08.001.

D. E. Kataoka and S. M. Troian. A theoretical study of instabilities at the advancing front of thermally driven coating films. *Journal of Colloid and Interface Science*, 192(2):350–362, 1997. ISSN 00219797. doi: 10.1006/jcis.1997.5018.

W. M. Kays and M. E. Crawford. *Convective Heat and Mass Transfer*. 1980. ISBN 9788578110796. doi: 10.1017/CBO9781107415324.004.

M. F. Kerho and M. B. Bragg. Airfoil boundary-layer development and transition with large leading-edge roughness. *AIAA Journal*, 35(1):75–84, 1997. ISSN 0001-1452. doi: 10.2514/3.13466.

J. Kim, P. G. Dennis, L. Sankar, and R. E. Kreeger. Ice Accretion Modeling Using an Eulerian Approach for Droplet Impingement. In *51st AIAA Aerospace Sciences Meeting including the New Horizons Forum and Aerospace Exposition*, Reston, Virigina, jan 2013. American Institute of Aeronautics and Astronautics. ISBN 978-1-62410-181-6. doi: 10.2514/6.2013-246.

T. Kim, D. Adalsteinsson, and M. C. Lin. Modeling ice dynamics as a thin-film stefan problem. In *EG CA - EuroGraphics Symposium on Computer Animation*, pages 167–177, 2006. ISBN 3-905673-34-7.

R. J. Kind. Ice Accretion Simulation Evaluation Test. Technical Report November, Reseach and Technology Organisation, NATO, 2001.

R. Klein, K. R. Bates, and N. Nikiforakis. Well-balanced compressible cut-cell simulation of atmospheric flow. *Philosophical transactions. Series A, Mathematical, physical, and engineering sciences*, 367(1907):4559–75, nov 2009. ISSN 1364-503X. doi: 10.1098/rsta.2009.0174.

J. G. Knudsen and D. L. V. Katz. *Fluid dynamics and heat transfer*. McGraw-Hill series in chemical engineering. McGraw-Hill, 1958.

I. Langmuir and C. G. Suits. *The Collected Works of Irving Langmuir: Atmospheric Phenomena*. Pergamon Press, 1961.

G. Leese. *On the Accretion of Ice on Aircraft*. PhD thesis, University of Cambridge, 2010.

M. Leppäranta. A review of analytical models of sea-ice growth. *Atmosphere-Ocean*, 31(1):123–138, mar 1993. ISSN 0705-5900. doi: 10.1080/07055900.1993.9649465.

R. J. LeVeque. *Finite volume methods for hyperbolic problems*. Cambridge University Press, 2002. ISBN 0521009243.

R. J. LeVeque. The dynamics of pressureless dust clouds and delta waves. *Journal of Hyperbolic Differential Equations*, 01(02):315–327, jun 2004. ISSN 0219-8916. doi: 10.1142/S0219891604000135.

H. Li, F. Chen, and H. Hu. Simultaneous measurements of droplet size, flying velocity and transient temperature of in-flight droplets by using a molecular tagging technique. *Experiments in Fluids*, 56(10):1–14, 2015. ISSN 07234864. doi: 10.1007/s00348-015-2063-y.

P. R. Lowe. An approximating polynomal for the computation of saturation vapor pressure. *Journal of Applied Meteorology*, 16(1):100–103, 1976.

V. Ludviksson and E. N. Lightfoot. Deformation of advancing menisci. *AIChE Journal*, 14(4): 674–677, jul 1968. ISSN 0001-1541. doi: 10.1002/aic.690140433.

F. T. Lynch and A. Khodadoust. Effects of ice accretions on aircraft aerodynamics. *Progress in Aerospace Sciences*, 37(8):669–767, nov 2001. ISSN 03760421. doi: 10.1016/S0376-0421(01)00018-5.

B. J. Mason. *The Physics of Clouds*. Clarendon Press, Oxford, UK, second edi edition, 1971.

S. Mauch. A Fast Algorithm for Computing the Closest Point and Distance Transform. Technical Report 077, Caltech, 2001.

S. Mauch. *Efficient Algorithms for Solving Static Hamilton-Jacobi Equations*. PhD thesis, California Institute of Technology, 2003.

B. P. Messinger. Equilibrium Temperature of an Unheated Icing Surface as a Function of Air Speed, jan 1953.

A. Meurer, C. P. Smith, M. Paprocki, O. Čertík, S. B. Kirpichev, M. Rocklin, A. Kumar, S. Ivanov, J. K. Moore, S. Singh, T. Rathnayake, S. Vig, B. E. Granger, R. P. Muller, F. Bonazzi, H. Gupta, S. Vats, F. Johansson, F. Pedregosa, M. J. Curry, A. R. Terrel, Š. Roučka, A. Saboo, I. Fernando, S. Kulal, R. Cimrman, and A. Scopatz. SymPy: symbolic computing in Python. *PeerJ Computer Science*, 3:e103, jan 2017. ISSN 2376-5992. doi: 10.7717/peerj-cs.103.

G. Mingione and V. Brandi. Ice Accretion Prediction on Multielement Airfoils. *Journal of Aircraft*, 35(2):240–246, mar 1998. ISSN 0021-8669. doi: 10.2514/2.2290.

H. Miura and I. I. Glass. Supersonic Expansion of a Dusty Gas Around a Sharp Corner. *Proceedings of the Royal Society A: Mathematical, Physical and Engineering Sciences*, 415(1848): 91–105, jan 1988. ISSN 1364-5021. doi: 10.1098/rspa.1988.0004.

M. R. Moore, M. S. Mughal, and D. T. Papageorgiou. Ice formation within a thin film flowing over a flat plate. *Journal of Fluid Mechanics*, 817:455–489, 2017. ISSN 14697645. doi: 10.1017/jfm.2017.100.

F. Morency, F. Tezok, and I. Paraschivoiu. Anti-Icing System Simulation Using CANICE. *Journal of Aircraft*, 36(6):999–1006, nov 1999. ISSN 0021-8669. doi: 10.2514/2.2541.

T. G. Myers and D. W. Hammond. Ice and water film growth from incoming supercooled droplets. *International Journal of Heat and Mass Transfer*, 42(12):2233–2242, jun 1999. ISSN 00179310. doi: 10.1016/S0017-9310(98)00237-3.

T. G. Myers, J. P. F. Charpin, and S. J. Chapman. The flow and solidification of a thin fluid film on an arbitrary three-dimensional surface. *Physics of Fluids*, 14(8):2788, 2002a. ISSN 10706631. doi: 10.1063/1.1488599.

T. G. Myers, J. P. F. Charpin, and C. P. Thompson. Slowly accreting ice due to supercooled water impacting on a cold surface. *Physics of Fluids*, 14(1):240, 2002b. ISSN 10706631. doi: 10.1063/1.1416186.

J. J. Nelson, A. Alving, and D. Joseph. Boudary layer flow of air over water on a flat plate. *Journal of Fluid Mechanics*, 284:159–169, 1995.

J. Nocedal and S. J. Wright. *Numerical Optimization*, volume 43. 1 edition, 1999. ISBN 0387987932. doi: 10.1002/lsm.21040.

NTSB (National Transportation Safety Board). In-Flight Icing Encounter and Loss of Control, Simmons Airlines, d.b.a. American Eagle Flight 4184, Avions de Transport Regional (ATR) Model 72-212, N401AM, Roselawn, Indiana, October 31, 1994. Technical report, Washington, D.C., 1994.

A. Oron and S. G. Bankoff. Long-scale evolution of thin liquid films, 1997. ISSN 0034-6861.

S. Özgen and M. CanIbek. Ice accretion simulation on multi-element airfoils using extended Messinger model. *Heat and Mass Transfer*, 45(3):305–322, 2009. ISSN 09477411. doi: 10.1007/s00231-008-0430-4.

J. Pan, W. Wang, Y. Wei, J. Chen, and L. Wang. A calculation model of critical liquid-carrying velocity of gas wells considering the influence of droplet shapes. *Natural Gas Industry B*, 5(4): 337–343, 2018. ISSN 23528559. doi: 10.1016/j.ngib.2018.01.007. URL `https://doi.org/10.1016/j.ngib.2018.01.007`.

I. Paraschivoiu and F. Saeed. Ice Accretion Simulation Code CANICE. In *International Aerospace Symposium, Carafoli 201*, 2001.

I. Paraschivoiu, F. Saeed, and S. Gouttebroze. CANICE - Capabilities and Current Status. In *NATO/RTO Workshop on Ice Accretion Simulation Evaluation Test*, Capua, Italy, 2000.

M. Pelanti and R. J. LeVeque. High-Resolution Finite Volume Methods for Dusty Gas Jets and Plumes. *SIAM Journal on Scientific Computing*, 28(4):1335–1360, jan 2006. ISSN 1064-8275. doi: 10.1137/050635018.

K. Peng and W. Xinxin. Super-cooled Large Droplets consideration in the droplet impingement simulation for aircraft icing. *Procedia Engineering*, 17:151–159, jan 2011. ISSN 18777058. doi: 10.1016/j.proeng.2011.10.018.

B. Perthame and C.-w. Shu. On positivity preserving finite volume schemes for Euler equations. *Numerische Mathematik*, 73(1):119–130, mar 1996. ISSN 0029-599X. doi: 10.1007/s002110050187.

G. Poots. *Ice and Snow Accretion on Structures*. Research Studies Press Ltd, 1996. ISBN 0863801897.

G. Poots and P. Skelton. Rime- and glaze-ice accretion due to freezing rain falling vertically on a horizontal thermally insulated overhead line conductor, 1992. ISSN 0142727X.

M. Potapczuk, K. M. Al-Khalil, and M. Velazquez. Ice Accretion and Performance Degradation Calculations with LEWICE-NS. In *31st Aerospace Sciences Meeting*, 1993.

M. G. Potapczuk. *Navier-Stokes analysis of airfoils with leading edge ice accretions*. PhD thesis, University of Akron, 1989.

E. Radenac, A. Kontogiannis, C. Bayeux, and P. Villedieu. An extended rough-wall model for an integral boundary layer model intended for ice accretion calculations. In *2018 Atmospheric and Space Environments Conference*, pages 1–23, 2018. ISBN 978-1-62410-558-6. doi: 10.2514/6.2018-2858.

J. A. Rees. *A Short Course in Cloud Physics*, volume 27. aug 1976. doi: 10.1088/0031-9112/27/8/028.

A. J. Roberts. *Model emergent dynamics in complex systems*. SIAM, 2015. ISBN 9781611973556.

A. J. Roberts and Z. Li. An accurate and comprehensive model of thin fluid flows with inertia on curved substrates. *Journal of Fluid Mechanics*, 553:33, apr 2006. ISSN 0022-1120. doi: 10.1017/S0022112006008640.

A. Roosing, O. Strickson, and N. Nikiforakis. Fast Distance Fields for Fluid Dynamics Mesh Generation on Graphics Hardware. *Manuscript submitted for publication*, 2018.

A. Rothmayer and J. Tsao. Water film runback on an airfoil surface. *38th Aerospace Sciences Meeting and Exhibit*, (c), 2000. doi: 10.2514/6.2000-237.

A. P. Rothmayer, B. D. Matheis, and S. N. Timoshin. Thin liquid films flowing over external aerodynamic surfaces. *Journal of Engineering Mathematics*, 42(3-4):341–357, 2002. ISSN 00220833. doi: 10.1023/A:1016152918706.

R. V. Roy, A. J. Roberts, and M. E. Simpson. A lubrication model of coating flows over a curved substrate in space. *Journal of Fluid Mechanics*, 454:235–261, 2002. ISSN 0022-1120. doi: 10.1017/S0022112001007133.

G. A. Ruff and B. M. Berkowitz. Users Manual for the NASA Ice Accretion Prediction Code (LEWICE). Technical report, Lewis Research Center, NASA, Brook Park, Ohio, 1990.

F. Saeed, S. Gouttebroze, and I. Paraschivoiu. Modified CANICE for improved prediction of airfoil ice accretion. In *8th Aerodynamic Symposium*, 2001.

T. Saito. Numerical Analysis of Dusty-Gas Flows. *Journal of Computational Physics*, 176(1):129–144, feb 2002. ISSN 00219991. doi: 10.1006/jcph.2001.6971.

L. W. Schwartz. Viscous flows down an inclined plane: Instability and finger formation. *Phys. Fluids A*, 1(May 2015):443–445, 1989. ISSN 08998213. doi: 10.1063/1.857466.

H. Shan, L. Jiang, and C. Liu. Direct numerical simulation of flow separation around a naca 0012 airfoil. *Computers & fluids*, 34(9):1096–1114, 2005.

W. Sheng and T. Zhang. *The Riemann Problem for the Transportation Equations in Gas Dynamics*. Number no. 654 in American Mathematical Society: Memoirs of the American Mathematical Society. American Mathematical Society, 1999. ISBN 9780821863770.

J. Shin, B. Berkowitz, H. Chen, and T. Cebeci. Prediction of ice shapes and their effect on airfoil performance. In *29th Aerospace Sciences Meeting*, volume 31, pages 263–270, Reston, Virigina, jan 1991. American Institute of Aeronautics and Astronautics. doi: 10.2514/6.1991-264.

F. J. Simon. Summary of CASA Predictions. In *NATO/RTO Workshop on Ice Accretion Simulation Evaluation Test*, Capua, Italy, 2000.

M. Sivapuratharasu, S. Hibberd, M. Hubbard, and H. Power. Inertial effects on thin-film wave structures with imposed surface shear on an inclined plane. *Physica D: Nonlinear Phenomena*, 325:86–97, jun 2016. ISSN 01672789. doi: 10.1016/j.physd.2016.03.008.

D. Spalding and W. Pun. A review of methods for predicting heat-transfer coefficients for laminar uniform-property boundary layer flows. *International Journal of Heat and Mass Transfer*, 5(3-4): 239–249, mar 1962. ISSN 00179310. doi: 10.1016/0017-9310(62)90014-5.

G. Strang. On the Construction and Comparison of Difference Schemes. *SIAM Journal on Numerical Analysis*, 5(3):506–517, sep 1968. ISSN 0036-1429. doi: 10.1137/0705041.

Technical University Munich. DrivAer, 2018. URL `http://linkinghub.elsevier.com/retrieve/pii/S0021999112005839`.

J.-L. Thiffeault and K. Kamhawi. Transport in Thin Gravity-driven Flow over a Curved Substrate. *pre-print*, 2006.

E. F. Toro. *Riemann solvers and numerical methods for fluid dynamics - A Practical Introduction*. Springer, 3rd edition, 2009. ISBN 9783540252023. doi: 10.1007/b7976.

P. Verdin. *An Automatic Multi-Stepping Approach for Aircraft Ice Prediction*. PhD thesis, Cranfield University, 2007.

P. Verdin, J. P. F. Charpin, and C. P. Thompson. Multistep Results in ICECREMO2. *Journal of Aircraft*, 46(5):1607–1613, sep 2009. ISSN 0021-8669. doi: 10.2514/1.41451.

P. G. Verdin and J. P. F. Charpin. Multi-Stepping Ice Prediction on Cylinders and Other Relevant Geometries. Technical Report 3, 2013.

H. K. Versteeg and W. Malalasekera. *An introduction to computational fludi dynamics: the finite volume method*. Pearson, second edi edition, 2007.

A. E. von Doenhoff and E. A. Horton. A low-speed experimental investigation of the effect of a sandpaper type of roughness on boundary-layer transition. Technical report, National Advisory Committee for Aeronautics. Langley Aeronautical Lab., 1958.

W. H. Wentz and H. C. Seetharam. Development of a Fowler flap system for a high-performance general aviation airfoil. Technical report, Wichita State University, 1974.

F. M. White and I. Corfield. *Viscous fluid flow*. 2006.

J. Williams, S. Hibberd, H. Power, and D. S. Riley. On the effects of mass and momentum transfer from droplets impacting on steady two-dimensional rimming flow in a horizontal cylinder. *Physics of Fluids*, 24(5), 2012. ISSN 10706631. doi: 10.1063/1.4718653.

W. Wright. User Manual for the Improved NASA Lewis Ice Accretion Code LEWICE 1.6. Technical report, Lewis Research Center, Ohio, 1995.

W. Wright. LEWICE 2.0 Results and Analysis. In *NATO/RTO Workshop on Ice Accretion Simulation Evaluation Test*, pages 1–25, Capua, Italy, 2000.

W. Wright. User's Manual for LEWICE Version 3.2. Technical Report November, QSS Group, Inc, Cleveland, Ohio, 2008.

W. Wright and M. Potapczuk. Semi-Empirical Modelling of SLD Physics. In *42nd AIAA Aerospace Sciences Meeting and Exhibit*, number April, Reston, Virigina, jan 2004. American Institute of Aeronautics and Astronautics. ISBN 978-1-62410-078-9. doi: 10.2514/6.2004-412.

W. B. Wright and A. Rutkowski. Validation Results for LEWICE 2.0. Technical Report January, 1999.

W. B. Wright, R. W. Gent, and D. Guffond. DRA / NASA / ONERA Collaboration on Icing Research. Technical report, 1997.

L. Wutschitz. On a Cartesian cut-cell approach to dusty gas flows and its application to the accretion of ice on aircraft. Master's thesis, University of Cambridge, 2014.

L. Wutschitz and N. Nikiforakis. A Cartesian Cut-Cell Approach for Modelling Air and Water Droplet Flow. In *54th AIAA Aerospace Sciences Meeting*, pages 1–12, San Diego, California, jan 2016. American Institute of Aeronautics and Astronautics. ISBN 978-1-62410-393-3. doi: 10.2514/6.2016-0600.